AN ABSTRACT OF THE DESERTATION OF

Edward A. Le for the degree of Doctor of Philosophy in Wood Science and Materials Science presented on May 14, 2010.
Title: Numerical Modeling and Experiments on Wood-Strand Composites.

Abstract approved:

_____ _____

John A. Nairn William H. Warnes

In wood-based composites, the glue-line (interface) between wood-strands affects the stress transfer from one member to the next. The glue-line properties determine the rate of load transfer between phases and these properties depend on wood species, surface preparation, glue properties, glue penetration into wood cells, and moisture content of the wood. As a result, the strength and stiffness of the composites are significantly affected by the amount, distribution, and properties of the resin.

In the first part of this research, the glue-line stiffness between wood strands was determined by experiments. The interfacial properties were calculated from experimental data on double lap shear (DLS) specimens. The results showed that in both normal and densified wood strands, resin coverage has a positive effect on the interfacial stiffness, and consequently on stiffness properties of wood-based composites. As adhesive coverage increased from discrete droplets (1% coverage) to a continuous bondline (100% or fully glued) the stiffness of the interface increased significantly and could even become stiffer than the wood itself.

In the second part of this research, once the mechanical properties of individual strands and interfacial properties were determined by experiment, they were used as

input to a numerical model for the mechanical properties of oriented strand board (OSB) panels. Modeling the compression of wood-strands and wood-based composites was done using a numerical method called the material point method (MPM). MPM was used to model wood-strand composite mechanical properties as a function of compaction (densification), compaction rate, strand geometry (strand length and strand size), strand undulations, strand properties, and adhesive properties. In addition, density profiles of the panels as a function of selected variables were studied. The various simulations were for either conventional OSB panels or for OSB panels with densified strands in the surface layers.

To demonstrate the importance of glue-line properties and undulating strands, a simple homogenized rule of mixtures (HROM) was developed for OSB and oriented strand lumber (OSL) structures. The results of MPM were compared to the HROM model. The results show that typical glue properties have a significant effect on mechanical properties of OSB. The role of the interface is a consequence of strand undulation in typical OSB structures and the length of the strands. Interfacial properties are most important for composites with short strands or for composites with imperfect alignment such as OSB with undulating or misaligned strands.

Numerical Modeling and Experiments on Wood-Strand Composites

by
Edward A. Le

A THESIS

submitted to

Oregon State University

in partial fulfillment of
the requirements for the
degree of

Doctor of Philosophy

Presented May 14, 2010
Commencement June 2010

Doctor of Philosophy dissertation of Edward A. Le presented on May 14, 2010.

APPROVED:

_____

Co-Major Professor, representing Wood Science

_____

Head of the Department of Wood Science and Engineering

_____

Co-Major Professor, representing Materials Science

_____

Director of the Materials Science Program

_____

Dean of the Graduate School

I understand that my dissertation will become part of the permanent collection of Oregon State University libraries. My signature below authorizes release of my dissertation to any reader upon request.

_____

Edward A. Le, Author

ACKNOWLEDGEMENTS

I would like to humbly acknowledge the love and support that I have received from a number of wonderful people; without them, I could not have completed this dissertation. It is with great pleasure; I would like to take this opportunity to express my sincere appreciation to all those who have helped me throughout this process.

First and foremost, I owe my deepest gratitude to Professor John A. Nairn who, not only served as my advisor but also encouraged and challenged me throughout my academic program. He taught me about composites models and was constantly developing MPM code to fit into this research. He always kept his office door opened for discussion. I am grateful to have Dr. Nairn as my advisor and for the valuable opportunity he has given me to complete this research at Oregon State University. Hopefully we will be able to continue our collaboration in the future.

Second, I would like to thank Professor Fred Kamke for his kindness, experimental input, and valuable discussion of OSB processing, as well as serving on my PhD committee. I also thank Professor Bill Warnes for his kindness and guidance when I first arrived at OSU and for serving on my PhD committee. I would like to thank Professor David Cann, Professor Joe Zaworski, Professor Prasad Tadepalli for their support and serving on my PhD committee.

I would also like to express my gratitude to Professor Greg Smith (UBC) for the help in preparing the glue bonds with variable coverage, Dr. Andreja Kutnar for assisted me scanning the density of the OSB specimens, Vardan Rathi for suppling the VTC strands and information about hybrid poplar, Dr. Peter Kitin for SEM help, Dr. John Simonsen for valuable conversations on cellulose nanocrystals and allowing me to borrow his books and Dr. Liping Xue for discussions on MPM and Fortran code.

I am indebted to many people at OSU, my colleagues for their help and companionship during my stay at OSU, Mr. Milo Clauson for experimental input and assistance on mechanical testing, Terralyn Vandetta for maintaining the Linux cluster

and answering my questions on utilizing computation resources, the OSU Writing Center staff for spending many hours editing my papers, the Wood Science & Engineering and the Materials Science department faculty and staff for their help to get things running smoothly and for making my study at OSU so pleasurable.

I would like to take this opportunity to thank my former professor and colleagues such as Dr. Charles H. Henager and Dr. Howard Heinisch at Pacific Northwest National Lab whose guidance enabled me to gain a great deal of knowledge while I was at PNNL, Professor Thomas Stoebe at the University of Washington, who constantly encouraged and convinced me continuing with my education and attending graduate school. His knowledge and enthusiasm supported me to apply for graduate school during my senior year. Without his encouragement, I would not be where I am today.

I would like to thank the National Research Initiative of the USDA Cooperative State Research, Education and Extension Service for providing the funding for this research: Grant # 2006-35504-17444.

I wish to thank my family, especially my parents, Hong V. Le and Sang T. Bui for the love and unconditional support to pursue my interests. They worked so hard to raise me and my siblings during and after the Viet-Nam war. I sincerely acknowledge my mother for her hard work, including the sacrifices for us while my dad was in the communist education camp for many years. I would like to thank my dad, who spent many years in the terrible camp, for his services during the war, and for enduring the many tragedies that he went through. I would like to thank my grandmother for the inspiration, my aunt, Dao Bui for her endless encouragement, my uncle, Professor Den Truong at North Carolina State University for his support and constant guidance, my brothers and sister, Hoai Le, Thuy-Huong Le, Ho-Hoai Le, Joshua Le, and Max Le for their continuous support and always putting up with me even when I was unreasonable. Last, but not least, I am tremendously grateful to my parents in-law,

Cong & Ngoc Nguyen for their understanding and assistance for my family while I was away from home.

To my wife, Kayly M. Nguyen, I thank you for your relentless love, unconditional support, encouragement, and taking care of our beautiful daughter so I could contribute most of my time to this research. This work could not have been done without your support. I thank you for always believing in me and enabling me to be who I am and where I am today.

Finally, I want to close with a quote by Richard David Bach, a writer who puts learning into perspective and inspires me:

"Learning is finding out what you already know, Doing is demonstrating that you know it, Teaching is reminding others that they know it as well as you do. We are all learners, doers, and teachers."

TABLE OF CONTENTS

Page

TABLE OF CONTENTS (Continued)

Page

TABLE OF CONTENTS (Continued)

Page

TABLE OF CONTENTS (Continued)

Page

TABLE OF CONTENTS (Continued)

Page

TABLE OF CONTENTS (Continued)

Page

LIST OF FIGURES

LIST OF FIGURES (Continued)

Figure Page

LIST OF FIGURES (Continued)

Figure Page

LIST OF FIGURES (Continued)

Figure Page

LIST OF FIGURES (Continued)

LIST OF TABLES

Table Page

This work is a dedication to my beautiful daughter (Katelynh Hoang-Khuyen Le).

Vita

Edward A. Le (FKA Huy-Hoai T. Le) was born and raised in Lam Dong, Viet Nam. He left Viet Nam and came to the U.S.A. as an immigrant (refugee) at the age of eighteen. He first enrolled at the University of Washington in 1996. He received his Bachelor of Science in Chemistry and Bachelor of Science in Metallurgical Engineering from the University of Washington in March 2001. He then obtained a Master of Science degree in Materials Science and Engineering at the University of Washington in December 2002 focusing on deposition of nano-materials and solidification and crystal growth. In summer 2002 and summer 2004, he worked for the Pacific Northwest National Lab focusing on the effect of swelling of SiC/SiC composite as a function of carbon interphase and interaction of Helium atoms with edge dislocations in Alpha-Fe. During his undergraduate and graduate study, he worked at the Fred Hutchinson Cancer Research Center and had the opportunity to work closely with biological science and antibiotics for cancer drugs. Because of his interest in biological science, materials science, and the inspiration of his grandmother, who passed away due to cancer, he wanted to know how they may be useful for cancer treatment and decided to go to medical school. He attended at St. Mathew Medical School in 2006 but was struggled with financial assistant for tuition. He decided to go back to graduate school to obtain the Ph.D. in materials science, to what he is best suited and can support himself financially. He enrolled at the Oregon State University in April 2007 with the dual program in Materials Science and Wood Science. He completed his Ph.D. in Materials Science and Ph.D. in Wood Science in June 2010. He specializes in the area of wood-strand based composites and natural fiber polymer matrix composites with an emphasis on analytical, numerical modeling and solid mechanics to improve the mechanical performance of the final composites.

CHAPTER 1 - INTRODUCTION, OBJECTIVE AND BACKGOUND

1.1. Introduction and Motivation

Wood composites can be classified into I) wood-based panels and engineered lumber, and II) advanced hybrid composites such as wood-plastic composites (WPC) and inorganic bonded composites. Wood-based panels and engineered lumber are composed of wood strands and veneers such as in plywood, oriented strand broad (OSB), oriented strand lumber (OSL), laminate strand lumber (LSL) and laminated veneer lumber (LVL). Since wood-strand composites are cheap, have high stiffness and can be tailored to various applications, they dominate the market for structural applications. In order to meet high demand, maintain mechanical strength and stiffness, and maintain low cost, the manufacturer needs to look at many aspects such as material cost, logging, processing and factors that contribute toward the mechanical properties. One way to increase stiffness of a panel is to increase resin usage, but this will increase the cost. Being able to minimize the material cost by optimizing resin consumption while maintaining mechanical performance is very important in the manufacturing of wood-strand and wood-based composites.

Mechanical properties of most composites such as carbon fiber/polymer or glass fiber/polymer composites and wood based composites depend on the quality of the interfaces between phases. Specifically, the stiffness of most manmade composites and wood-based composites depend on the quality of the glue lines that hold phases together. The glue-line properties of wood composites depend on wood species, surface preparation, glue penetration into wood cells, and moisture content of the wood. Resin type, content, distribution, and curing are generally the main factors that are affected bonding properties (Lehmann 1970, Hill and Wilson 1978, Youngquist et al 1987, Kamke et al 1996).

In composites, strength and stiffness are affected by the joints between wood pieces and these are mainly controlled by the interface region. Two roles for an interface are to hold two composite elements together and to transfer stress from one element to the other. While the main mechanical property of holding two composite elements together is strength, transfer of stress from element to element is controlled by stiffness.

Most work on wood composite glue lines focuses on strength (when the adhesive fails). There is much less work on the role of stiffness and stress transfer in wood composites properties. Stiffness is often the property with more practical relevance when designing with wood composites and therefore it needs more study. A good interface will rapidly transfer stress between elements and therefore result in superior stiffness in the composites.

Several methods of experimentation are used for researching interfacial properties of composites. The fragmentation test (Nairn and Kim 2005 and references there in), the microbond test (Fraser 1983, Bascom 1991, Dibenedetto 1991), the pull-out test (Verpoest 1990, Feillard 1994, Detassis 1996), and the microindentation test (Robinson 1987, Melanitis 1993) have been used for interfacial analysis of fibrous composites. These methods work well with synthetic fiber polymer composites but not with wood-strand composites. These types of test typically load an adhesive bond line to failure and record the load at the time of failure. Thus, these tests mostly measure for strength and do not measure stiffness. There is no attention to what happens before failure; which is controlled more by interfacial stiffness. Similarly, adhesive bonds tests for wood joints use double lap shear (DLS) method for testing shear strength. ASTM D 3528 is one standard test for strength properties of and it uses a DLS adhesive joint. This is a common test in wood composites where the specimens are loaded in tension to failure and measured for shear strength. In order to measure the interfacial stiffness property between strands in wood-strand composites, a new experimental method is needed.

Furthermore, once interfacial properties are measured with a new experimental method, the next question is: how does it affect the mechanical properties of wood composites? As recently reported, the resin coverage has a positive effect on interfacial stiffness and consequently on stiffness properties of wood-base composites (Nairn and Le 2009). In manufacturing OSB, the strands are mixed with resin in the blender, as a result, the amount of resin coverage on strand surfaces vary from strand to strand. Therefore, experiments that vary the amount and control of the glue line in a systematic way would be instructive. Experiments to study the mechanical properties of wood-based composites in term of the interfacial properties of glue lines, amount of glue, different type of glue, input structures, and strand mechanical properties, however might not be feasible.

Therefore, this thesis uses material point method (MPM) with inputs from experiments to tackle this problem by computer simulation methods.

1.2. Wood-Strand Composites

1.2.1 Oriented Strand Board (OSB)

OSB is a structural panel that is composed of adhesives and wood strands and pressed under heat and pressure into a panel. OSB is composed of face (surface) and core layers. Strands from face and core layers are roughly perpendicular to each other. Because of its low cost, use of strands from small logs, and high strength and stiffness, OSB has developed into having a larger market share than plywood. OSB can be used for making I-joists, wall sheathing, subfloors, floor underlayment and many other products. Phenol formaldehyde (PF) resins are typically used in the face layers, while isocyanates are typically used in the core. Wax is used in the manufacture of OSB for enhancing its moisture resistance and the dimensional stability (Wood Handbook 2007). In the manufacturing of OSB, resin is sprayed onto the strands in a rotary drum blender with an atomizer. The resin droplet size, distribution and amount of coverage all contribute to the mechanical properties of OSB panels.

1.2.2 Oriented Strand Lumber (OSL)

Unlike OSB, OSL is composed of only one layer. The strands in OSL are longer and parallel to each other. Because of the longer strand lengths, OSL has higher stiffness and strength compared to OSB. OSL is usually made into a panel and then cut into smaller size. Furthermore because of having high grade, parallel strands, and high compaction, OSL can have better mechanical properties than virgin wood lumber.

1.3. Adhesive

There are two types of adhesives—thermoset and thermoplastic adhesives. Thermoset adhesives are crosslinked polymeric resins after they are cured with heat and/or heat and pressure. Thermoplastics are not crosslinked. The most common thermoset adhesives used in the manufacturing of wood composites are phenol

formaldehyde (PF), polymeric methylenediphenyl diisocynate (pMDI), urea formaldehyde (UF), and melamine urea formaldehyde (MUF). The most common thermoplastic resins used in the manufacturing of wood and wood-plastic wood composites are polyvinyl acetate (PVA), polyethylene, polypropylene and polyvinyl chloride (PVC). PVA is commonly used as an adhesive in the wood furniture industry.

The bond strength of wood composites depends on adhesive use, the wood surface, adhesive penetration into wood cells, moisture content and the anatomy of the wood. More adhesive moves into the wood cell when there is a more open structure (or less dense structure). Resin penetration into the wood cell may affect the strength and stiffness of the interface. Penetration is thought to be important but results with densified wood suggests it may have limited role on glue line properties (Nairn and Le 2009, Kutnar et al 2007). As adhesive penetrates into the wood cell it may reinforce the wood resulting in increased stiffness of the glue-line zone. A high performance joint may result where the strength of the joint exceeds the strength of the wood (Reve, Vick et al 1991). The increased stiffness may also increase the stress transfer between the wood elements. On the other hand, if too much resin penetrates into the wood cells, it may leave the bond line starved of resin, resulting in poor properties. Thus bond line performance will depend on amount of glue and how much penetrates wood cells versus the amount that remains at the bond line.

Choosing the right adhesive can reduce stress concentrations at the interface and result in increased performance of the overall composites. As shown by Gindl et al (2005), an adhesive that has a similar elastic behavior to wood will reduce stress concentration on the bondline. Furthermore, Saiki et al (1983) reported that the strength of the joints is highest when they are bonded with a closed direction of the grain (or bond between two wood members that have parallel grain to each other). This is valid for radial and tangential direction but not for longitudinal direction. The authors claimed that the reason for higher strength of closed grain adhesive bonding is that the adhesive cast in the tracheid lumen provides some anchoring (Saiki et al 1983).

1.3.1 *Phenol Formaldehyde (PF) Resin*

The most common adhesive for structural wood-based composites is phenol formaldehyde (PF) resin. PF resin is a thermosetting resin with a mixture of phenol and formaldehyde in the presence of either an acid or base catalyst (see Figure 1.1). They are waterborne and polar (Frihart 2005). Unlike PF resins for OSB, PF resins for plywood are commonly blended with extenders, fillers and caustic soda. These additives will increased the resin viscosity (Ebewele, River et al 1986). PF resins are subdivided into novalaks and resole. Novolaks have a formaldehyde/phenol ratio of less than 1 and are generally made with an acid catalyst, while resole resins have a formaldehyde/phenol ratio of higher than 1 and are made with a base catalyst (Koch 1987). In most wood bonding applications resole resins are used because they have good wetting properties and the cure is delayed until activated by the heat, which allows extra product assembly time. These resoles have a formaldehyde/phenol ratio of 1.0-3.0 and a pH value of 7-13. After the PF resin is applied to wood, the low molecular weight components of the PF resin causes the cell walls to swell (Frazier and Ni 1998). This penetration into the cell walls is possible because PF resins have hydrogen bonding functionalities. The swelling allows some molecules to penetrate into the cell walls, but due to the small quantities of resin, only the immediate vicinity of the cell wall swells and not the whole cell wall (Wilson, Gregory et al 1979; Frihart 2005). Resole resins plasticize the wood, but they make the bonded panel more hygroscopic and can create excessive swelling of composite panels (River, Vick et al 1991). Despite this effect, resoles are still the most common PF resins.

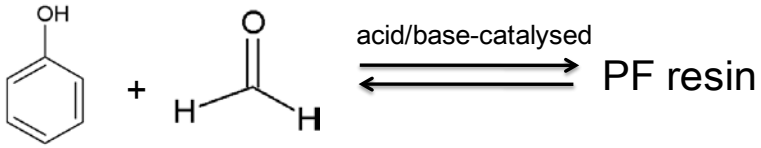

Figure 1.1. Schematic representation reaction of PF resin.

1.3.2 *Polyvinyl Acetate (PVA, Tite Bond Original)*

PVA is the most commonly used for wood furniture glue. As a wood glue, PVA is known as white glue or the yellow “carpenter’s glue”. PVA is produced from ethylene,

ethanoic acid and a mercury (I) salt. The degree of polymerization of polyvinyl acetate typically gives 100 to 5000 g/mole molecular weight (MW) (see Figure 1.2). The ester groups of the polyvinyl acetate are sensitive to alkali and will slowly convert PVA into polyvinyl alcohol and acetic acid. Under alkaline conditions, boron compounds, such as boric acid or borax causes the polymer to cross-link forming tackifying precipitates or slime. As an emulsion in water, PVA emulsions are good adhesives for porous materials, particulary for wood, paper, and cloth, and as a consolidant for porous building stone, in particular sandstone (Young et al 1999). PVA has poor gap-filling abilities, water resistance and heat resistance. To improve the water resistance, heat resistance and mechanical properties once cured, various crosslinkable monomers such as N-(hydroxymethyl)acrylamide can be added to modify PVA glues (Cho et al 1999, Lui et al 2005). Once the PVA glue is applied to wood, it sets quickly (typically within 15 min) at ambient temperature and the peak strength for the adhesive bonds is quickly achieved.

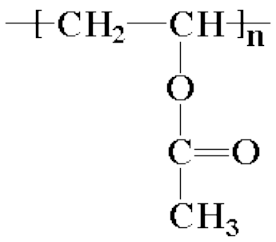

Figure 1.2. Chemical structure of PVA resin.

1.4 Flow Chart of Tasks in this Research

Figure 1.3 shows a flow chart of the tasks in this research. In the interfacial experiment tasks, a double lap shear (DLS) test was used to measure the compliance response of adhesives. Wood strands with straight grain were used to prepare the DLS specimens. Prior to gluing the strand with PF or PVA resin, the stiffness of each individual strand was measured. Different amounts of adhesive coverage were then applied to DLS specimens. Finally, the interfacial stiffness parameters were extracted by using a shear lag model to interpret the measured compliance results from the DLS tests.

In the modeling tasks, the interfacial stiffness parameters were input into a numerical model to study their effect on mechanical properties. The modeling of wood

strands composites (OSB) involved mat formation by compaction. The mat formation process was started with a random structure based on strand length, width, and gap between strands along with their standard deviations. The individual strand mechanical properties were also measured and input into the numerical model. The numerical method used in this study was the material point method (MPM). An elastic-plastic with hardening law model was used to incorporate the effect of yielding during compaction. MPM calculations for bending and tension were compared to a simple laminate plate theory. The sensitivity of results to various physical and geometric parameters was studied. The results for vertical density profile of composite panels from MPM were compared to the experimental data by an X-ray profilometer. Most results were 2D simulations but some 3D simulations were needed for density profile studies.

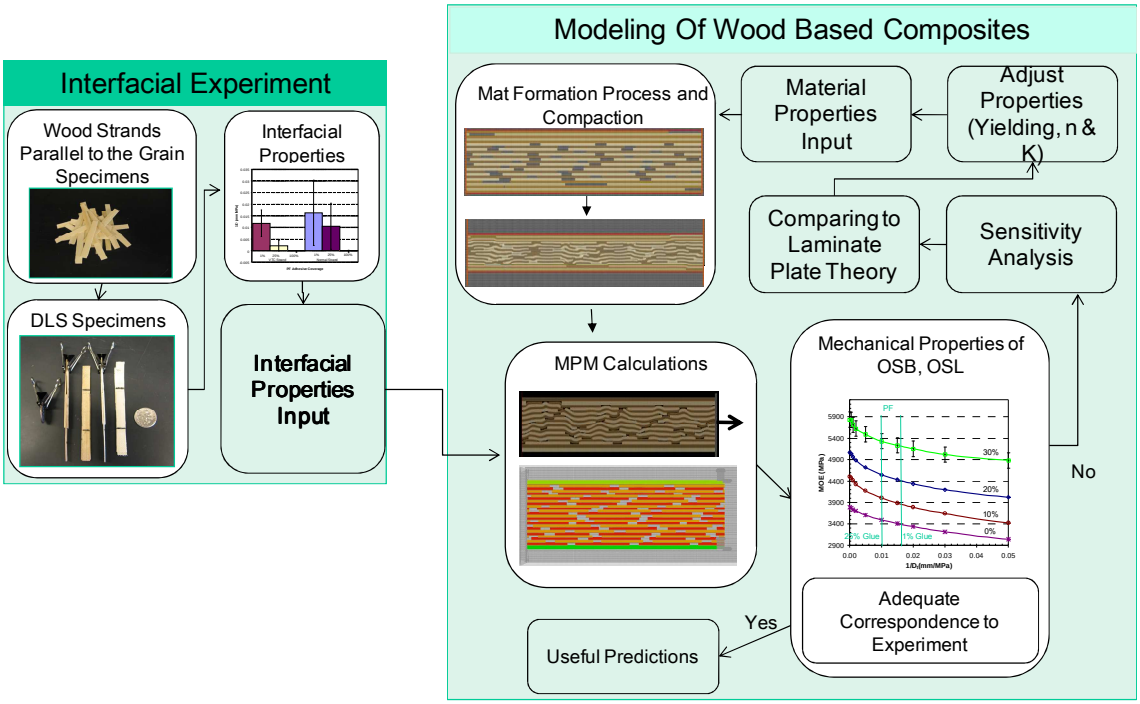

Figure 1.3. Flow chart of tasks in this research.

1.5 Technical Objectives of the Research

The overall goal of this research was to develop the Material Point Method (MPM) as a potential tool for numerical modeling of wood and wood-based composites that is capable for modeling many details of wood anatomy and wood-based composites

processing including mechanical properties, strand undulation, and glue-line stiffness effects. In order to achieve this goal the following specific objectives were pursued:

I. Determine the role of glue-lines for OSB in the panel mechanical properties
II. Evaluate the effect on mechanical properties of wood-based composites of using enhanced wood strands (such viscoelastic thermal compression [VTC] strands) in wood-based composites.

In order to complete these objectives, the following specific tasks were pursued:

1. Develop a new experimental technique to measure the interfacial stiffness properties for strand-to-strand bonds with varying amounts of adhesive coverage.
2. Construct a Material Point Method (MPM) model to study mechanical properties of OSB with bond-line interfaces.
3. Expand MPM to include elastic and plastic behavior with a work hardening law to simulate OSB compaction.
4. Study the effect of adhesive coverage on the mechanical stiffness of glued strands in wood-based composites (from discrete droplets to a continuous bondline).
5. Develop homogenized rule-of-mixtures model to help interpret OSB panel mechanical properties and MPM results.
6. Investigate the effect of interfacial properties of adhesives on mechanical behavior of OSB panels loaded in bending or in tension.
7. Study the density profile of OSB panels as a function of selected variables.

1.6 Rationale and Significance

Due to non-renewable and non-sustainable nature of synthetic composites such as carbon fiber and glass fiber composites, there is increasing demand for renewable composites panels for structured applications, such as engineered wood panels like OSB. Currently, wood resources in the United States are limited more and more to smaller diameter trees. The manufacturer that produces engineered OSB products can use small

log sizes (less than 20 year old trees). Furthermore, wood-strand composites such as OSB and oriented strand lumber (OSL) are able to enhance their properties by tailoring to specific applications (e.g., I-beam and Glulam for high load applications). With the advantages of engineering design of wood products, new wood composites can be established. Therefore, knowing the factors that control the mechanical properties of wood-strand composites is key for successful design of new products.

Specifically, this research can predict the mechanical properties of wood-strand composites in terms of its morphology and adhesive coverage (interfacial properties). This prediction has not been possible before. The experimental and modeling work in this research has opened a window of opportunity for engineering design of structural wood-based composites based on constituents properties of the raw materials.

1.7 Structure of the Dissertation

This dissertation is divided into seven chapters, including this introductory chapter. Each chapter discusses the results of individual tasks or part of the overall model from the tasks shown in Figure 1.3. Each chapter contains an abstract, introduction, background, material and methods, results, and conclusion section. Each chapter ends with a list of references.

The new experiments on strand-to-strand glue lines that extracted the interfacial properties from double lap shear (DLS) tests using a shear-lag model is addressed in chapter 2.

Chapter 3 discusses the development of the numerical model by the material point method (MPM), the development of a simple rule-of-mixtures analysis, and the results of numerical modeling of tensile modulus. The validation and sensitivity of MPM is compared to a rule of mixture. Chapter 4 discusses the results of mechanical properties of wood-strand composites in bending and their comparison to rule of mixtures and beam theory analysis. The effect of strand length over thickness (slenderness ratio or aspect ratio) and gaps between strands on mechanical properties is addressed in chapter 5. The vertical density profile formation during the pressing process is discussed in chapter 6. Parameters that affect the density profile were also addressed. Chapter 6 also presents 3D results on density profiles.

Finally, chapter 7 summarizes the entire research, discusses the conclusions from the numerical, analytical and experimental work, and considers future research needs.

References

Bascom, W. D., Yon, K. J., Jensen, R. M., and Cordner L. (1991) “The adhesion of Carbon Fibers to Thermoset and Thermoplastic Polymers,” *J. Adhesion* vol. 34, 79-98.

Cho, Y.-W., S.-S. Han, and S.-W. Ko. (1999) PVA-containing chito-oligosaccharide side chain. Polymer, 1999. 41(6): p. 2033-2039.

Detassis, M., Pegoretti, A., and Migliaresi, C. (1996) J. Materials Science 31:2385-2392.

Dibenedetto, A. T. (1991) *Composites Science & Technology* 42:103-123.

Feillard, P., Desermot, G., and Favre, J. P. (1994) *Composites Science & Technology* 50:265-279.

Ebewele, R. O., B. H. River and J. A. Koutsky (1986). Relationship between phenolic adhesive chemistry and adhesive joint performance: Effect of filler type on fracture energy. J Appl Polym Sci 31(7): 2275-2302.

Fraser, W. A., Ancker, F. H., DiBenedetto, A. T., and Elbirli, B. (1983) *Polymer Composites* 4:238-248.

Frihart, C. R. (2005) Wood adhesion and adhesives. Handbook of wood chemistry and wood composites. R. M. Rowell. Boca Raton, FL, CRC Press: 215-278.

Frazier, C. E. and J. Ni (1998) On the occurrence of network interpenetration in the wood-isocyanate adhesive interphase. Int J Adhes Adhes 18: 81-87.

Hill, M. D., and J. B. Wilson (1978) “Particleboard strength as affected by unequal resin distribution on different particle fractions. Forest Prod. J., 28(11):44–48.

Kamke, F.A., E. Kultikova, and C. A. Lenth (1996) “OSB properties as affected by resin distribution. Pages 147–154 in The Fourth International Panel and Engineered-Wood Technology Conference & Exposition, Atlanta, GA.

Koch, G.S. (1987) Adhesives for the composite wood panel, industryPark ridge N.J.: Noyes data Corp.

Kutnar A., Kamke F., Nairn J., and Sernek M. (2008) "Mode II Fracture Behavior of Bonded Viscoelastic Thermal Compressed Wood," Wood and Fiber, 40, 362-373.

Kutnar A., Kamke, F. A. and M. Sernek (2008) The mechanical properties of densitfied VTC wood relevant for structural composites. Hoz als Roh-Werkst, 66(6): 439-446.

Lehmann, W. F. (1970) “Resin efficiency in particleboard as influenced by density, atomization, and resin content.Forest Prod. J., 20(11):48–54.

Liu, Y.-m., C.-z. Zong, and Y. Xu (2005) “Manufacture of the self-crosslinking PVAc emulsion under room temperature.” Zhongguo Jiaonianji, 14(7): p. 9-11.

Melanitis, N., Galiotis, C., Tetlow, P. L., and Davies, C. K. L. (1993) J. Composites 24:459-466.

Nairn, J. and E. Le (2009) “Numerical Modeling and Experiments on the Role of Strand-to-Strand Interface Quality on the Properties of Oriented Strand Board”, Wood Adhesion Special Publications, 2009.

Nairn A. J. and Kim W. B. (2002) "Observations of Fiber Fracture and Interfacial Debonding Phenomena Using the Fragmentation Test in Single Fiber Composites," J. Comp. Mat., 36, 1825-1858.

Robinson, I. M., Zakikhani, M., Day, R. J., Young, R. J., and Galiotis, C. (1987) J. Materials Science Letters 6:1212-1214.

River, B., C. Vick and R. Gillespie (1991) Wood as an adherend-Treatise on adhesion and adhesives. New York, Marcel Dekker.

Furuno, T., H. Saiki, T. Guto and H. Harada (1983) Penetration of glue inoit the tracheid lumina of softwood and the morphology of fractures by tensile-shear testts. Mokuzai Gakkaishi 29(1): 43-53.

Gindl, W., A. Sretenovic, A. Vincenti and U. Mueller (2005). Direct measurement of strain distribution along a wood bond line. Part II: Effects of adhesive penetration on strain distribution. Holzforschung 59: 307-310.

Young, M.E., M. Murray and P. Cordiner. Stone consolidants and chemical treatments in Scotland. Robert Gordon University, Building Research Establishment and Historic Scotland. http://www2.rgu.ac.uk/schools/mcrg/miconsol.htm.1999. Retrieved 2009-07-30.

Young, Youngquit, G. V., J. A., G. C. Myers and L. L. Murmain L. L. (1987) Resin distribution in hardwood: evaluated by internal bond strength and fluorescence microscopy. Wood Fiber Sci., 19(2):215–224.

Verpoest, I., Desaeger, M., and Keunings, R. (1990) *Controlled Interphases in Composite Materials*, 653-666.

U.S. Department of Agriculture. 1987. Wood Handbook. Agriculture Handbook No. 72, Superintendent of Documents, Washington D.C. 466pp.

CHAPTER 2 – MEASURING THE EFFECT OF ADHESIVE COVERAGE ON THE MECHANICAL STIFFNESS OF GLUED STRANDS IN ORIENTED STRAND BOARD

Abstract

The glue line between wood strands in wood composites affects the stress transfer from one member to the next and consequently affects the strength and stiffness of the composite. The glue-line properties of wood composites determine the rate of load transfer between phases and these properties depend on wood species, surface preparation, glue properties, glue penetration into wood cells, and moisture content of the wood. The interfacial properties may change depending on whether resin droplets of glue spread to a continuous line or remain as discrete droplets and depend on the total amount of glue.

In this study, one interfacial property of glue lines between wood strands was determined by experiments and composite modeling. The interfacial property was obtained as a function of resin coverage. It was calculated from experimental data on double lap shear (DLS) specimens by using shear-lag analysis. The results showed that in both normal and densified wood strands, resin coverage has a positive effect on the interfacial stiffness, and consequently is expected to affect the stiffness properties of wood-based composites. As adhesive coverage increased from discrete droplets (1% coverage) to a continuous bondline (100% or fully glued) the stiffness of the interface increased and could become stiffer than the wood itself. This effect was likely due to the penetration of the resin into the wood cells resulting in an interfacial region stiffer than the wood. More work is needed to study how penetration of resin into wood cells affects the interfacial stiffness parameter.

2.1 Introduction

Stiffness and strength of wood composites such as oriented strand board (OSB), oriented strand lumber (OSL), plywood, laminated veneer lumber (LVL), glue-lam, fiber board, and particle board depend on the quality of the glue. The glue line properties of wood composites depend on wood species, surface preparation, glue properties, glue penetration into wood cells, and moisture content of the wood. In composites, strength

and stiffness is often influenced by the joint between wood pieces and these are mainly controlled by the glue and the interface region. When wood is joined together in a composite, there are five elements to the bond: adhesive film, intra-adhesive boundary layers, adhesive-adherend interface, adherend subsurface and adherend proper (Frihart 2005). The interface is the area between the intra-adhesive boundary and adherend subsurface.

The strength of the joint is determined by the strength of the weakest member. The stiffness of the joint is controls the rate of stress transfer between adherends. Most work on bonded wood is on interfacial strength. Here the goal is to measure and characterize stress transfer, which can be thought of as interfacial stiffness. Interfacial stiffness is often overlooked but it is a critical property that can affect mechanical properties in wood composites (Nairn 2005). A good interface will rapidly transfer stress between elements and therefore result in superior stiffness in the composites.

Gluing is one of the most important ways to connect wood strands in a wood composite. For example, in oriented strand board (OSB), the strands are bonded together by discrete droplets of resin. The droplet size and spacing are thought to be of importance. Even small flaws could reduce the strength substantially (Smith 2005); it may also reduce stiffness. Resin type, content, distribution, and curing are generally the main factors affecting the bonding properties (Lehmann 1970, Hill and Wilson 1978, Youngquist et al 1987, Kamke et al 1996). However, it has been demonstrated that resin spot thickness does not affect the bonding strength, suggesting that one could lessen resin usage by reducing spot thickness and increasing resin surface coverage area (He et al 2007). A uniform distribution of small resin spots produces the best properties for a given resin content. In practice, it is difficult to produce uniform resin distribution. As a result, increases in resin content may help but will increase cost. Therefore, understanding how resin contributes to the bonding in wood-based composites is an important task for minimizing the cost while optimizing the performance.

Approximately 50% of processed wood is glued (Marra 1992). Wood gluing is more complex than gluing of other materials because wood is anisotropic and inhomogeneous (Frihard 2005). Gluing of wood into composites enables the use of small diameter, low quality logs, by connecting their elements into new materials (such as

OSB, OSL, LVL or glulam beams). Gluing is accomplished by using adhesives to hold materials together (ASTM 1989). Adhesion is the state where two surfaces are held together by interfacial forces. These may be valence forces, mechanical interlocking or both. Good adhesives/gluing can effectively transfer and distribute stresses, thereby allowing phases to share load and produce a composite material (Wood HandBook 1999).

Several experimental methods have been used for researching interfacial properties in composites. The fragmentation test (Nairn and Kim 2005 and reference there in), the microbond test (Fraser 1983, Bascom 1991, Dibenedetto 1991), the pull-out test (Verpoest 1990, Feillard 1994, Detassis 1996), and the microindentation test (Robinson 1987, Melanitis 1993) have been used for interfacial analysis of fibrous composites. These methods work well with synthetic fiber polymer composites but do not work with wood-strand composites. Furthermore, these tests measure interfacial strength and do not measure stiffness. These tests typically load an adhesive bond line to failure and record the load at the time of failure. There is no attention to what happens prior to failure; which is controlled more by interfacial stiffness.

One standard adhesive bond test for wood joints uses double lap shear (DLS) specimens for testing shear strength (ASTM D 3528). This is a common test in wood composites where a DLS specimen is loaded in tension until failure. The peak load at failure is used to obtain shear strength for the adhesive bond. ASTM D 3528 determines the shear strengths of adhesives when tested in an essentially peel-free standard specimen that develops adhesive stress distribution representative of that developed in typical low-peel production-type structural joints. Besides the DLS test, a lap-shear test for adhesive bonds (ASTM D 3163), a lap shear for sandwich joints (ASTM D 3164), a lap-shear for sandwich joints in shear by tension load (ASTM D 3164M), and a single-lap-joint laminated assembly (ASTM D 3165) all measure adhesive bond strengths. ASTM D 905 tests for strength properties of adhesive bonds in shear by compression loading. Another test, ASTM D 3433, tests fracture strength of adhesive bonds loaded in cleavage. As noted, all these currently available test methods for adhesive bonds load specimens to failure and measure strength.

Therefore, a new experimental technique is needed to study the bond line interfacial stiffness properties of wood strand composites. An experimental method was

developed here to study the role of the amount of glue on the stiffness of a double lap shear (DLS) specimen. DLS was used because it reduces out of plane loading when loaded in the direction parallel to the specimen. The interfacial stiffness was calculated from the DLS stiffness using shear-lag analysis. The glue line stiffness was studied as a function of resin coverage, type of glue, and type of wood strand. The interfacial stiffness from the DLS and other data were used to model the mechanical properties of OSB as a function of its interfacial properties.

2.1.1 Imperfect Interface

An analysis for the role of composite interfaces in composite stiffness was proposed by Hashin (Hashin 1991). He introduced a set of interfacial stiffness constants that quantify the degree of interfacial imperfection. Nairn (2007) has illustrated how to identify such interface parameters from experimental data in static loading. Bogren et al (2008) used a dynamic mechanical analyzer to measure Young's modulus and damping of wood-fiber reinforced polyactide. They claimed that the mismatch between the predicted and experimental values of Young's modulus may be attributed to imperfect interfaces with reduced stress transfer.

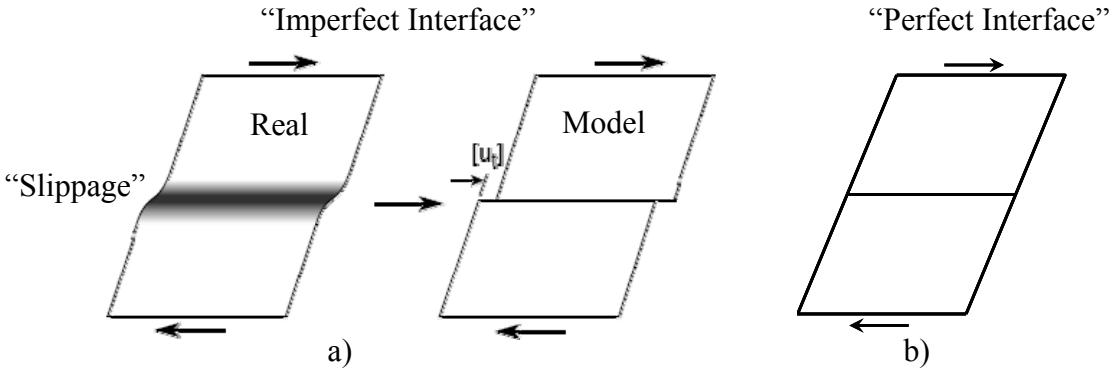

Figure 2.1. Glue line mechanics for perfect interface and imperfect interface. (Adapted from Nairn, 2007)

Most analyses of stress transfer, from a matrix to a fiber or from glue to wood, assume a perfect interface (Nairn 2007, Huang et al 2005). A definition of a perfect interface is that there is zero discontinuity along the interface. For an imperfect interface there is a slippage along the interface (see Figure 2.1). Figure 2.1 illustrates glue-line

mechanics for perfect and imperfect interfaces and shows a model for the glue line. Figure 2.1a shows complications in "real" glue-line because it includes the glue-line region and an interfacial zone. Figure 2.1a also shows a schematic drawing of simpler model representing the "real" interface as an "imperfect interface". The model allows displacement discontinuities to develop between adherends. The magnitude of the discontinuities is assumed to be proportional to the normal and shear stresses at the interface. The proportionality constants define the effective normal and shear compliance of the interface. The model uses zero compliance for a perfect interface (infinite stiffness or zero discontinuity) to infinite compliance for a debonded interface (or zero interfacial stress). More detailed discussion on the model is below.

Although the glue line in wood composites is not a 2D interface but rather a finite interphase region where glue may penetrate into the wood cell, an "imperfect interface" approach can avoid that complexity. "Imperfect interface" theory seeks to approximate a 3D interphase to a 2D interface by lumping all mechanical properties of the interphase into a small set of interface parameters (Hashin 1990) and all deformation into slippages. Hashin's model assumes the slippage is proportional to the interfacial stress. For shear loading (see Figure 2.1), the tangential slippage is:

$$[u_t] \propto \frac{\tau}{D_t} \qquad \text{(Eq. 2.1)}$$

where $[u_t]$ is the displacement jump along the interface, τ is the interfacial shear stress and D_t is an interfacial stiffness property. At $D_t \rightarrow \infty$, $[u_t] \rightarrow 0$ and the interface is perfect. When $D_t \rightarrow 0$, $\tau \rightarrow 0$ and the interface is debonded. All other values of D_t characterize an imperfect interface. D_t may also be negative ($1/D_t < 0$) and correspond to negative slippage due to an interphase that is stiffer than either adherend (Nairn 2007). The goal of this work was to use DLS specimens to load glue-lines in shear and to determine D_t for the glue bond.

2.2 Experimental

2.2.1 Materials

Low density hybrid poplar wood (*Populus deltoides x Populus trichocarpa*) cut into normal strands and processed into viscoelastic thermal compression (VTC) strands (Kamke and Kutnar 2007) from a plantation in Nortwest Oregon, were used in this study. Specimens were cut from 0.69 mm thick hybrid poplar strands. Individual strips were cut to 6 mm wide and 150 mm long with the grain direction parallel to the long axis of the strips. Specimens were then transferred to a conditioning room and equilibrated at 20 ^{o}C with 65% relative humidity for several days to reach 12% moisture content.

Two resins were used in this work. First was a typical commercial phenol-formaldehyde (FP) resin used in OSB, and manufactured by Georgia Pacific Resins, Inc. Second was a polyvinyl acetate (PVA) resin that is a typical wood glue manufactured by Tite Bond.

Wire-wound rods were used to precisely control the thickness of coating adhesive on the base plate and made by RD Specialties (Webster, New York, USA). A printing stamp was made of photopolymer with a surface texture composed of circular dots of various diameters in a square array and made by A-Z Stamps (Portland, OR, USA). The grey-scale of the plate was controlled by varying the diameter of the dots. The distance between the centers of adjacent dots on the printing stamps is given by the number of lines of dots per inch (lpi), or dot pitch (Smith 2003). The printing stamps used in this study to produce PF and PVA resin droplets had 25 lpi. A base plate made of 1/4-in-thick window glass was used with the printing stamps in the gluing process (see Appendix).

2.2.2 Methods and Procedures

In this study, the interfacial properties were measured by using the double lap shear (DLS) test. Figure 2.2 is the schematic representation of a DLS specimen. As shown, strand thickness is t, bond length is l and ends tabs have length L. The specimen width is W, elastic modulus is E, shear modulus is G. The shear moduli of the strands were estimated from axial elastic modulus using $G \approx E/15$ (Gibson and Ashby 1997).

In a DLS specimen, the calculation of interfacial properties depends on the MOE of each individual strand in the DLS specimen. Since MOE varies from specimen to

specimen, the MOE of each individual strand needed to be measured prior to gluing them together. We first prepared MOE specimens parallel to the grain by cutting 6 mm x 150 mm pieces out from individual strand. We then nondestructively measured modulus of elasticity (MOE) for each hybrid poplar specimen in tension parallel to the grain using Instron model 5445 with a clip gage. More than 1000 specimens were loaded in tension parallel to the grain for MOE results.

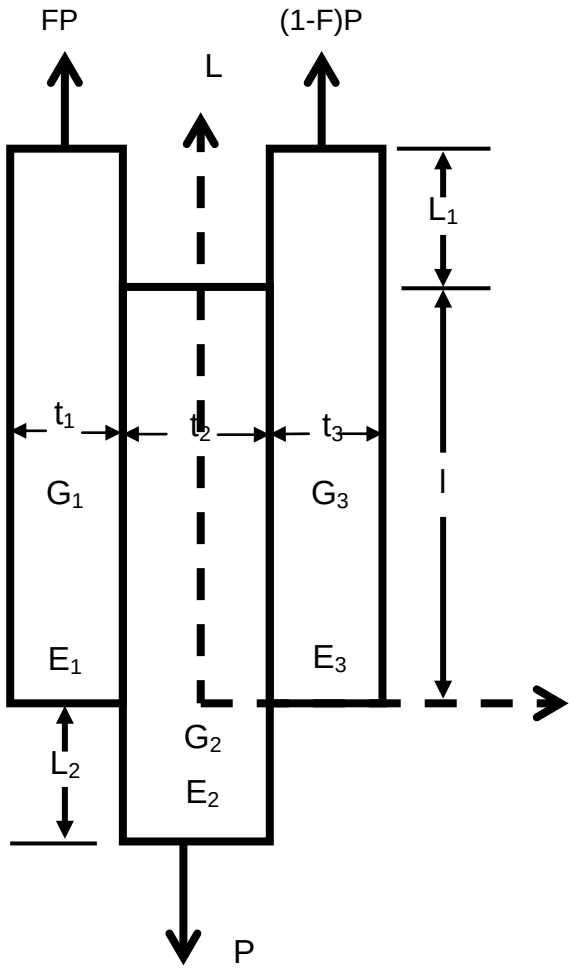

Figure 2.2. An asymmetric double lap shear specimen with strands of thickness t, bond lines of length l and ends tabs of length L. The specimen width is w, elastic modulus E, shear modulus G, P is load and F factor accounts for unsymmetric load.

The specimens with known MOE were then used to prepare DLS specimens by gluing them together using PF or PVA resin. The analysis is simplified if the DLS specimens are symmetric. To insure symmetry, we cut one strand with known MOE in

half and used these two halves for the two outside strands in the DLS specimen. The central strand was from a different strand.

The strands were coated with resin droplet arrays using a modified flexographic printing technique that was described by G. Smith (2003). The flexographic printing process is commonly used to produce newspapers and other printed materials. The surface of the printing-plate is composed of a multitude of raised dots; the diameter and local density of the dots determines the image that is printed. The printing-plates used in this work were composed of square arrays of circular dots and the distance between the centers of adjacent dots (the dot-pitch) was 25 lines per inch (lpi). The grey-scale of the plate was controlled by varying the diameter of the dots at the center of the pattern. Wire-wound rods were used to precisely control the thickness of coating adhesive on the base plate. The wire-wound rod consisted of a 1/2-inch-diameter stainless steel rod wound with the wire that had a diameter of 1mm. As shown by Smith (2003) a rod of 1/2-inch-diameter with the wire produced uniform adhesive layers of 1 μm.

A range of dot sizes was used to vary the adhesive surface coverage. Three different adhesive surface coverage area levels were applied for both PF and PVC and they were 1%, 25% and fully glued (100%) coverage. In the fully glued (100%) specimens, the adhesive was manually spread onto the strands. A total of over 500 DLS specimens were printed for the normal strands and viscoelastic thermal compression (VTC) strands (Kamke and Kutnar 2007).

After each DLS specimen was glued, they were then cured in a hot press at 100 psi and 180 ^{o}C for 5 minutes. The DLS specimens were then left in the control room for several days to get MC to 12%. Finally, the DLS specimens were loaded in tension using the Instron with an extensometer spanning the entire bond line section of the specimen. The global stiffness was measured from the load vs. displacement results.

2.2.3 Calculation of Interfacial Properties

The results for DLS stiffness were fitted to a shear-lag theory to extract the interfacial property D_t. The details of the shear-lag theory are described in Nairn (2007). The interfacial properties of individual specimens were measured and then averaged. Figure 2.2 is the representation of the DLS specimen. Because of the way specimens

were made, outer strands had the same MOE and thickness (E_1 and t_1). The central strand may be different (E_2 and t_2). The stiffness k for each specimen was determined from slope of the load versus displacement plot for the specimen.

Interfacial stiffness per surface area D_t (MPa/mm) was extracted using shear-lag theory with an imperfect interface. Let k be measured specimen stiffness, then

$$k = \frac{t_2 E_2 W}{\frac{C}{C_\infty}\frac{1}{(1+2R\lambda)} + \frac{L_1}{2\lambda R} + L_2} \qquad \text{(Eq. 2.2)}$$

where

$$\frac{C}{C_\infty} = 1 + \frac{(1-2R\lambda)^2 Tanh\left[\frac{l\beta}{2}\right] + (1+2R\lambda)^2 Tanh\left[\frac{l\beta}{4}\right]}{4lR\beta\lambda} + \frac{dkE_2 t_2 \beta^2 (1+2R\lambda)}{4l\beta} Csch\left(\frac{l\beta}{2}\right)$$

C/C_∞ is the ratio of the compliance of the bonded section of the specimen relative to the compliance where the three strands equally deform as a unit.

Here $\beta = \sqrt{\frac{\frac{1}{\lambda t_2 R E_2} + \frac{2}{t_2 E_2}}{\frac{\lambda t_2}{3G_1} + \frac{t_2}{6G_2} + dk}}$ is the shear-lag parameter, which in modern shear-lag theory can account for interfacial stiffness properties (Nairn 2004, 2007A).

$$dk = \frac{1}{D_t},\ \lambda = \frac{t_1}{t_2},\ R = \frac{E_1}{E_2},\ C_\infty = \frac{l}{t_2 W E_2 (1+2\lambda R)}$$

The only unknown in k is D_t or the interfacial property. Thus given experimental results for k and strand E and t, D_t can be calculated.

Figure 2.3 shows a sample shear-lag calculation of DLS specimen k as a function of interfacial stiffness. The stiffness deceases as $1/D_t$ increases. Given experimental results for specimen k, D_t can be found by numerical solution. The process is illustrated graphically in Figure 2.3 where "Expt k" is mapped to the curve, to find $1/D_t$. The dotted lines illustrate propagation of error in k (Δk) to error in $1/D_t$ ($\Delta(1/D_t)$). To minimize error in $1/D_t$, the curve should be as steep as possible. One way to achieve this goal is to keep bond length, l, as short as possible. All bond lengths here had l = 25 mm, which was

thought to be as short as possible while still having samples with reliable bonds and with ease of use in the mechanical tests.

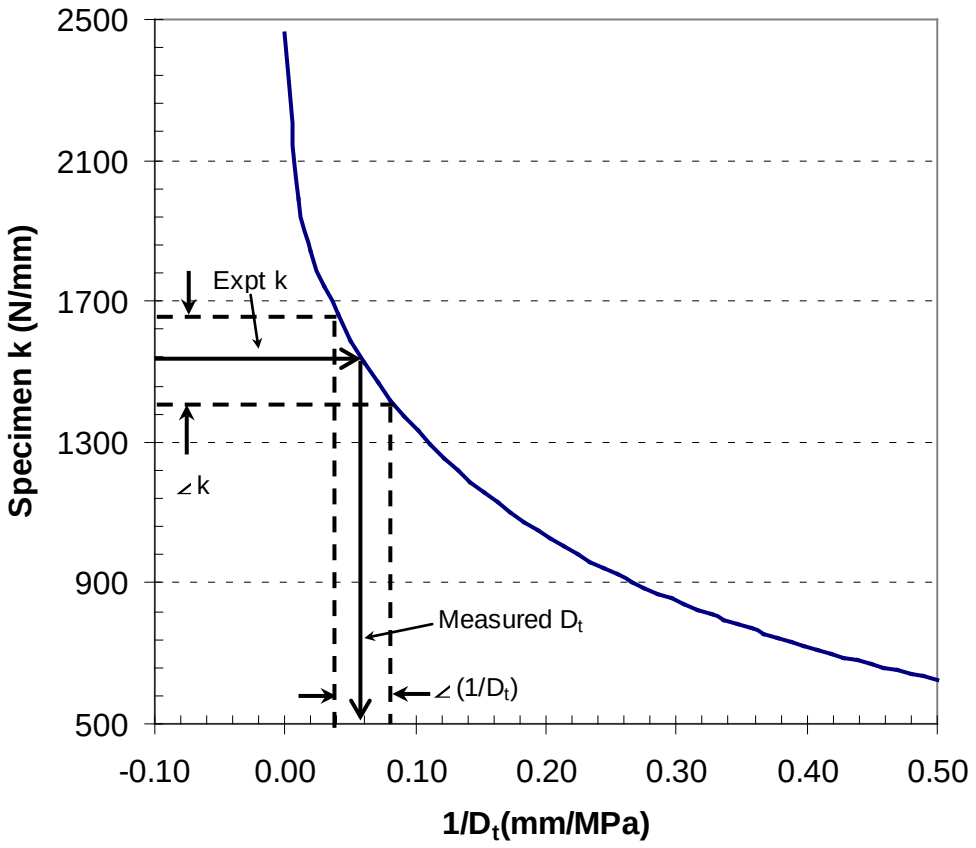

Figure 2.3. Analysis of interfacial stiffness.

2.2.4 Statistical Analysis of Experimental Data

Statistical analysis for these data was performed with standard one sample t-test using S-PLUS statistical software Version 8.0 and Microsoft Excel 2003 statistical analysis tools. All comparisons of interfacial properties and MOE were based on a 95% confidence level.

An analysis of variance (ANOVA) comparing different adhesive surface coverage was performed within the treatments and found that the interfacial property had statistically significant different results.

2.3 Results and Discussion

Figure 2.4 shows the mean modulus E in longitudinal direction of over 1000 specimens for both normal strands and VTC strands. The modulus for normal strands was close to solid wood for poplar wood which is 10GPa (Wood Handbook 2007). The Modulus E of modified VTC strands was much higher than the unmodified normal strands. Kamke and Kutnar (2007) demonstrated that the mechanical properties of modified VTC strands increases linearly as the level of density increases. This is the major advantage of modified VTC strands because the VTC process can utilize small logs and fast growing species like poplar and still obtain high MOE through densification.

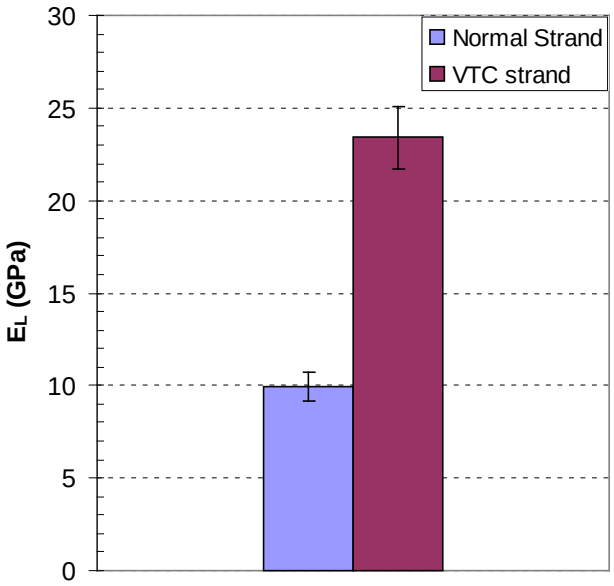

Figure 2.4. Modulus of Elasticity E_L for normal strand and VTC strand.

Over 300 DLS specimens were prepared and loaded in tension. The stiffness k was measured from the displacement and load. The stiffness and input geometries, elastic modulus and shear modulus were input into the shear-lag model to extract the interfacial properties. Three variations of adhesive coverage of PF resin and PVA were prepared, 1%, 25% and 100%. The 100% level is an extreme case of a lot more PF or PVA applied to glue each strand together for making DLS specimens. Table 2.1 lists the average values of interfacial properties and 95 percent confidence intervals for PF resin and PVA

wood glue at different adhesive coverages for normal and VTC strands. Although over 500 DLS specimens were prepared and tested, Table 2.1 only includes the last set of data that was tested using an Instron machine (model 5445 with clip gage). At 100% coverage both VTC and normal strands gave a negative D_t for PF resin but not for PVA glue with normal strands. VTC gave a better confidence interval than normal strands. PVA wood glue gave a smaller relative error than PF resin.

For a better representation of results in Table 2.1, Figure 2.5 shows the PVA adhesive compliance ($1/D_t$) for specimens with 1%, 25% and 100% coverage in DLS specimens with unmodified hybrid polar strands. No VTC experiments were done for the PVA resin. The adhesive stiffness property increased (compliance decreased) as the amount of glue coverage increased. Figure 2.6 plots the results for interfacial properties $1/D_t$ of Table 2.1 as the function of adhesive coverage for PF resin. VTC strands had a larger D_t than normal strands. As the level of adhesive coverage increased $1/D_t$ approaches zero or even become negative for both VTC and normal strands at 100% coverage. This demonstrates that as the adhesive goes from discrete droplets to a continuous line, the bonding stiffness of adhesive and wood is greater than the stiffness of the wood itself.

The surfaces of VTC strands were much smoother than normal strands (Kutnar and Kamke 2007) and densification was likely to limit resin penetration. This was confirmed by microscopy and SEM images of these bond lines (see appendix and Kutnar et al 2007). Nevertheless, the interfacial properties (D_t) of VTC were higher than for normal strands. Thus VTC strands should work well in OSB and may lead to better stress transfer between strands. Furthermore, the fact that higher D_t was achieved with less penetration suggest that penetration may not be important for good bonding.

Table 2.1: Average values, confidence interval of $1/D_t$ for PF resin and PVA based wood glue of normal and VTC strands

	$(1/D_t)$ in mm/MPa								
	PF resin						PVA Based		
Adhesive Coverage	VTC	95%*	NS**	Normal Strand	95%*	NS**	Normal Strand	95%*	NS**
1%	0.01177	± 0.00640	20	0.01628	± 0.01406	22	0.14645	± 0.05617	17
25%	0.00210	± 0.00343	20	0.01048	± 0.00995	22	0.06536	± 0.01832	16
100%	-0.00017	± 0.00032	20	-0.00022	± 0.00042	22	0.03693	± 0.01963	15

* 95% Confidence interval

** Number of DLS sample

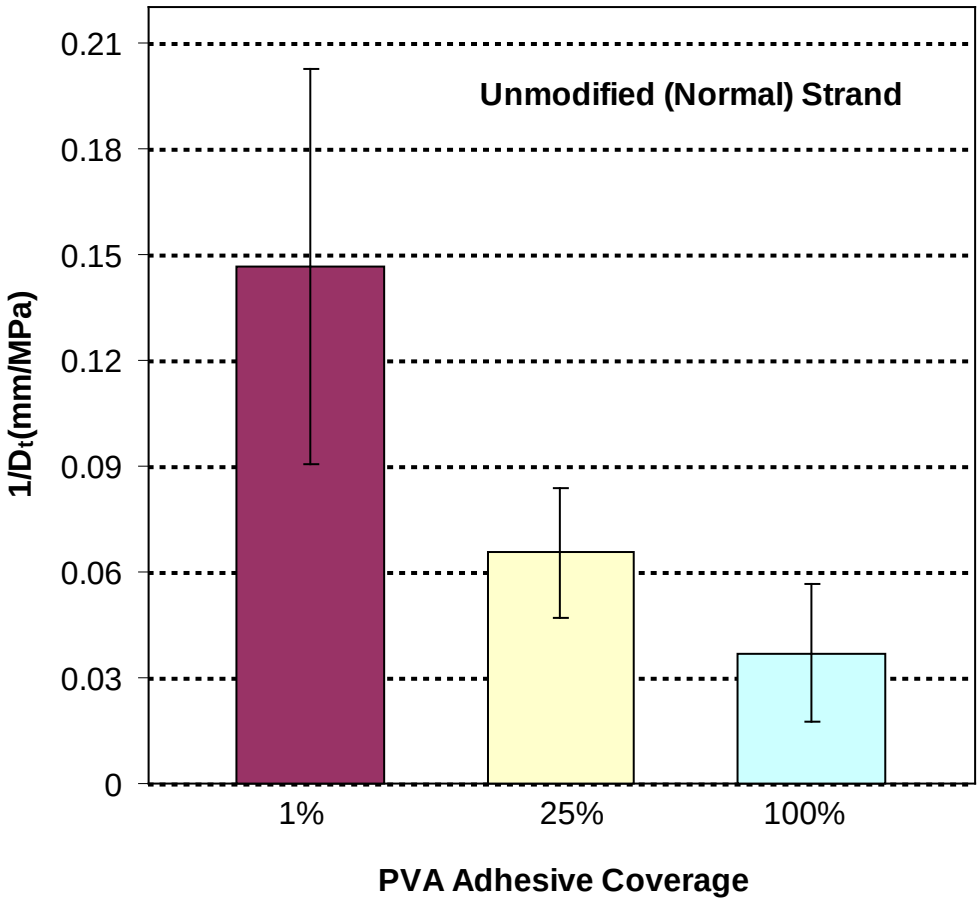

Figure 2.5. Measured adhesive compliance for PVA resin on normal (unmodified) strands for different percent of adhesive coverage.

For better comparison Figure 2.7 plots $1/D_t$ as the function of adhesive coverage for both PF resins and PVA wood glue. The PVA wood glue has much lower D_t than PF resins. At 100% coverage, the PVA glue bond, unlike PF glue bonds, did not perform as an interphase being reinforced by resin. The relative error bars for PVA were slightly better than for PF due to the larger magnitude of $1/D_t$, which resulted in larger displacements caused by glue-line deformation.

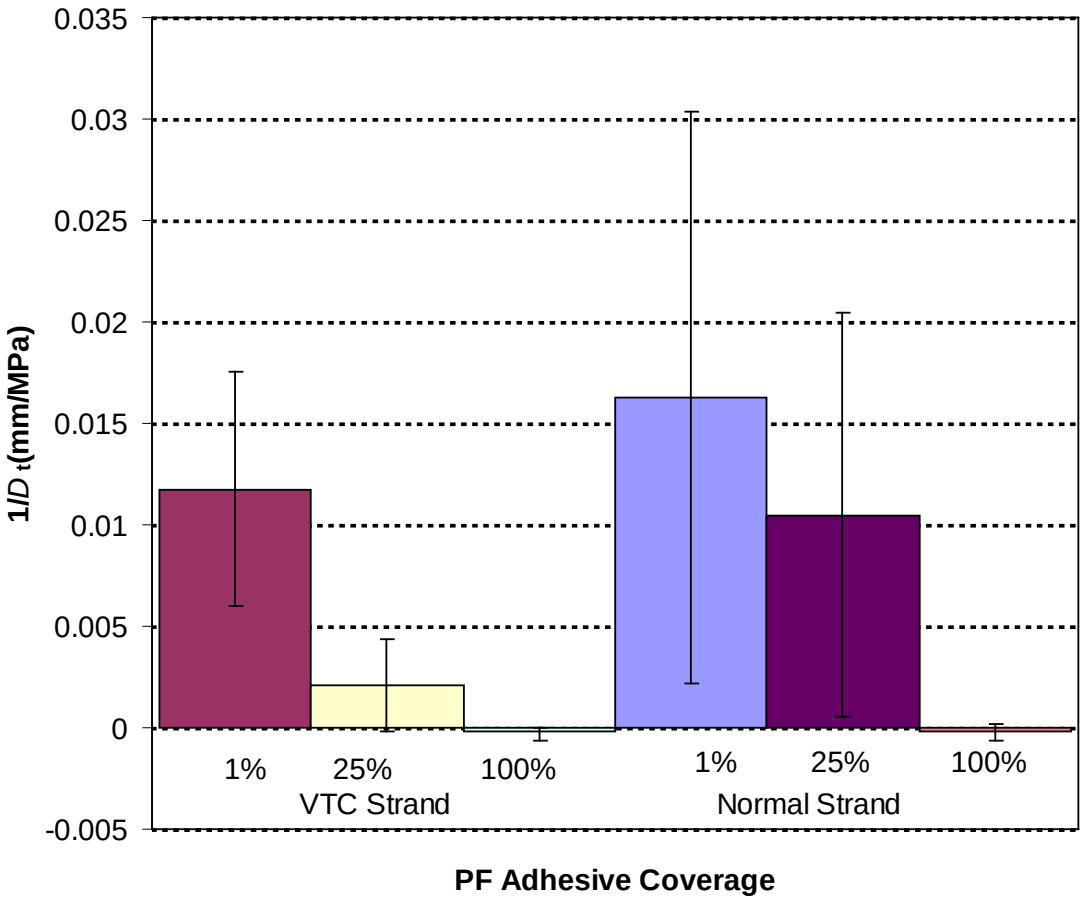

Figure 2.6. Measured adhesive compliance for PF resin on unmodified (normal strands) and VTC for different adhesive coverage.

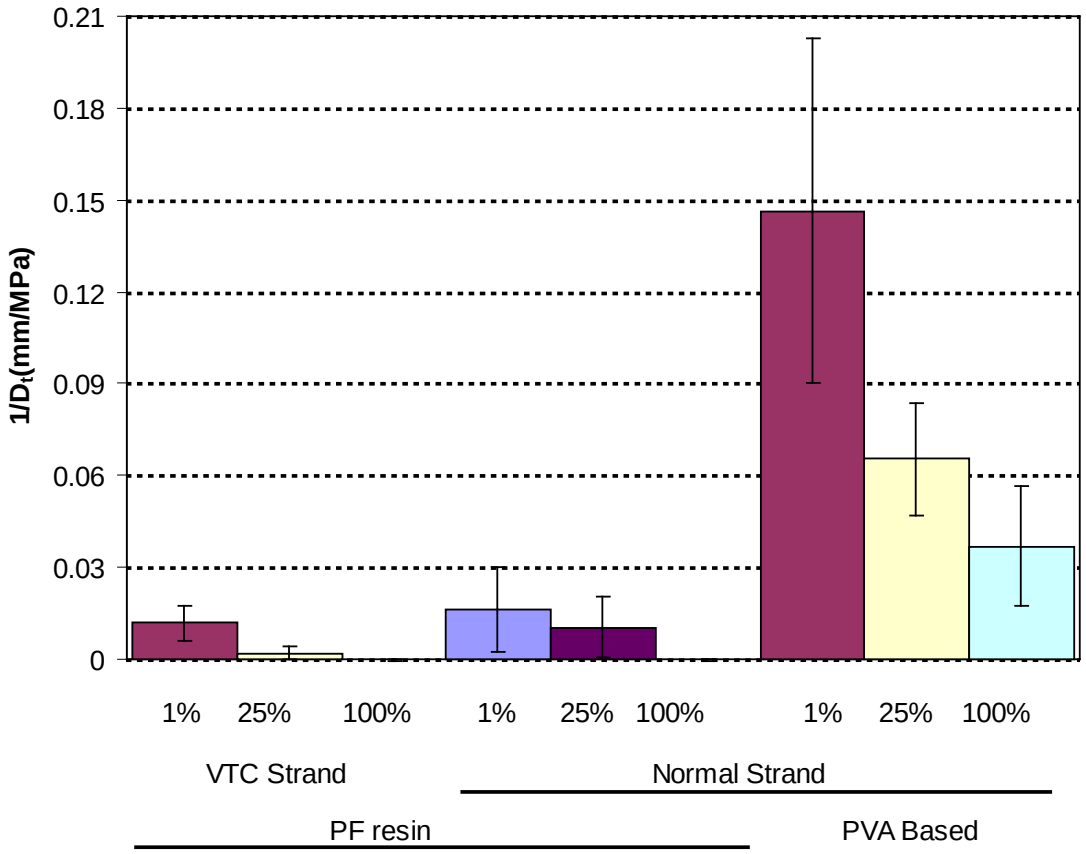

Figure 2.7. Interfacial compliance for specimens with various adhesive surface coverage area for VTC and normal strand with PF and PVA.

2.4 Summary and Conclusions

There was consistency in the values for specimen k for continuous bond lines (large amount of PF resin, 100%) compared to the k for 25%, and 1% adhesive coverage. Using shear-lag theory, we extracted the interfacial parameter D_t given specimen mechanical properties and geometries. The interfacial property varied significantly from discrete drops (1% coverage) to continuous bond line (100%). The interfacial property is highest for 100% and smallest for 1% adhesive coverage. There was a 60% increase in interfacial property from 1% to 25% adhesive coverage for normal strands with PF resin. The interfacial property D_t, is higher for PF resin than for PVA wood glue. D_t is also

higher for VTC strands than for normal hybrid poplar strands. As the level of adhesive increased from 1% to 100% coverage, the stiffness of the interface could become stiffer than the wood itself (negative values of D_t). This may be due to the penetration of the resin into the wood cell and consequently creating interfacial region stiffer than the wood.

In addition to the smoother surface of VTC strands, VTC strand allow less resin penetration into wood cells. Despite less penetration, the bond line D_t was higher. Perhaps, less adhesive penetration into the wood cells of VTC strands made more adhesive available at the surface to make a better bond line. Therefore, more work is needed to confirm how penetration of resin into wood cells affects the interfacial stiffness parameter. The observation here suggests penetration is not needed for good stress transfer (high D_t) and might even be somewhat detrimental to good composites.

Appendices

Appendix 2.1: Processes for making double lap shear (DLS) specimen from wood strands.

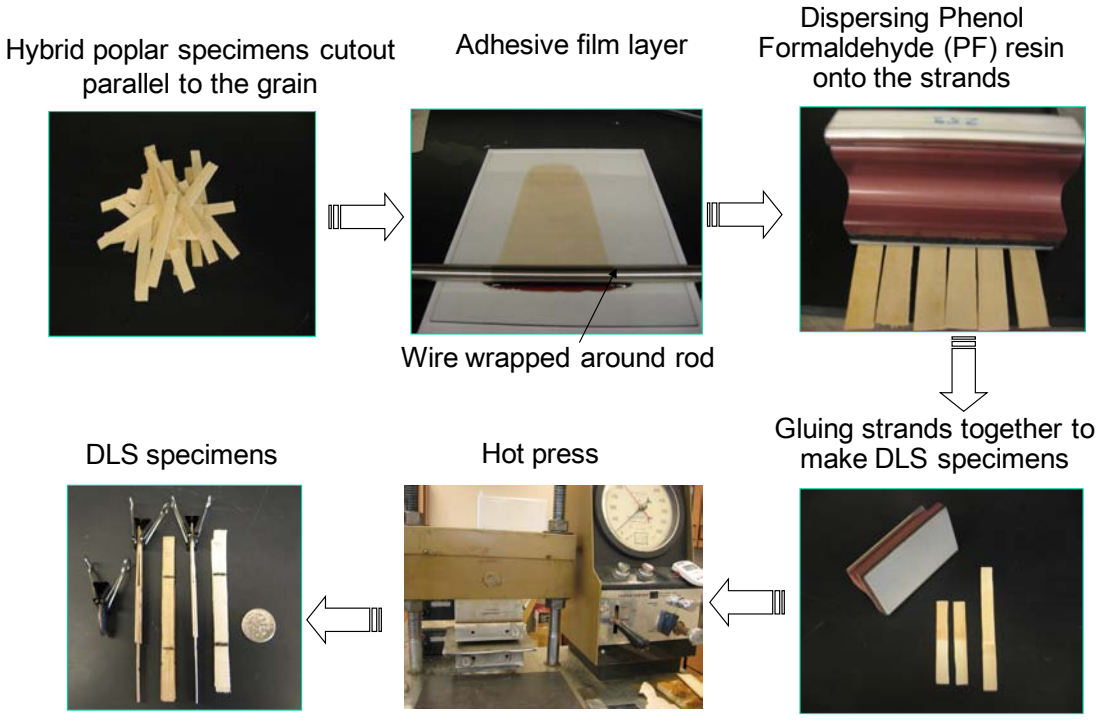

Appendix 2.2: SEM bondline images of VTC and unmodified strands

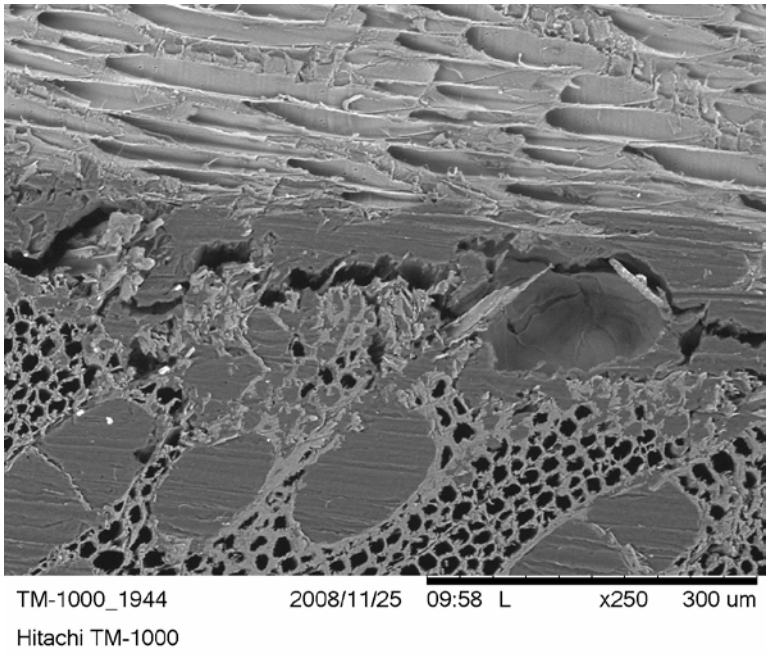

Figure 2.1A. SEM bondline image of unmodified strands.

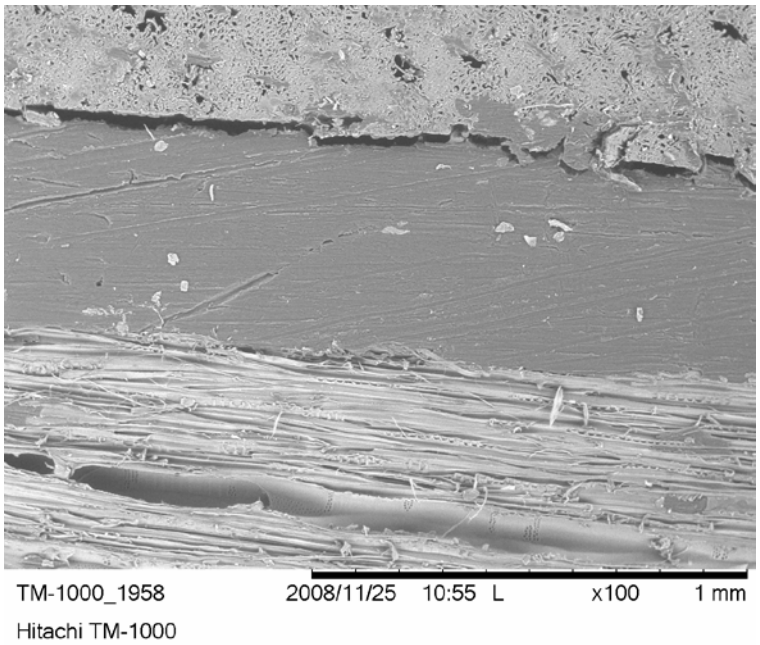

Figure 2.2A. SEM bondline image of VTC strands.

Figure 2.1A shows the bondline image of unmodified strand. PF resins were filled into the vessel. The crack line along the interface is due to image specimen preparation.

Figure 2.2A shows the bondline image of modified strands (VTC). Unlike Figure 2.1A, Figure 2.2A less adhesive moves (or penetrates) into the wood cells, more resin at the bondline. The crack line along the interface is due to image specimen preparation.

References

Ayilmis, N. et al. (2006) Effect of various fire retardants on surface roughness of plywood. Building and Environment, v. 41, pp 887-892.

ASTM (1989) Standard terminology of adhesives. Designation D907-89. Annual book of standards, vol. 15.6

Bascom, W. D., Yon, K. J., Jensen, R. M., and Cordner L. (1991) "The adhesion of Carbon Fibers to Thermoset and Thermoplastic Polymers," *J. Adhesion* vol. 34, 79-98.

Detassis, M., Pegoretti, A., and Migliaresi, C. (1996) J. Materials Science 31:2385-2392.

Dibenedetto, A. T. (1991) *Composites Science & Technology* 42:103-123.

Fraser, W. A., Ancker, F. H., DiBenedetto, A. T., and Elbirli, B. (1983) *Polymer Composites* 4:238-248.

Feillard, P., Desermot, G., and Favre, J. P. (1994) *Composites Science & Technology* 50:265-279.

Frihart, C. (2005) Wood adhesion and adhesives. In: wood chemistry and wood composites. Ed: R. Rowell. CRC press. pp. 215-278.

Frihart C. (2006) Wood Structure and Adhesive Bond Strength. In D. Stokke and L. Groom, eds. Characterization of the cellulosic cell wall, pp 241-253.Wiley-Blackwell.

Gibson, L. J., Ashby, M. F. (1997) Cellular Solids: Structure and Properties. Cambridge University Press, Cambridge.

Gardner D. (2006) Adhesion mechanisms of durable wood adhesive bonds. In D. Stokke and L. Groom, eds. Characterization of the cellulosic cell wall, pp 254-266.Wiley-Blackwell.

Huang, M., J. A. Nairn, F. Liu, and M. G. Lagally (2005) Mechanical stability of ultrathin Ge/Si film on SiO2: The effects of Si/SiO2 interface. J. Applied Physics, 97:116108.

He et al. (2007) Theoretical modeling of bonding characteristics and performance of wood composites. Part III. Bonding strength between two wood elements, Wood and Fiber Science, 39 (4), pp566-577.

Hill, M. D., and J. B. Wilson (1978) Particleboard strength as affected by unequal resin distribution on different particle fractions. Forest Prod. J. 28(11):44–48.

Kamke, F. A., E. Kultikova, and C. A. Lenth (1996) OSB properties as affected by resin distribution. Pages 147–154 in The Fourth International Panel and Engineered-Wood Technology Conference & Exposition, Atlanta, GA.

Katz, L. et al (2008) On the anisotropic elastic properties of woods. *J. Mater Sci* 43:139-145.

Keimel, F. A. (2003) Historical development of adhesives and adhesive bonding. In Pizzi. A.and Mittal K. L. Handbook of adhesive technology. Marcel Dekker. pp. 1-12.

Kutnar A., Kamke F., Nairn J., and Sernek M. (2008) "Mode II Fracture Behavior of Bonded Viscoelastic Thermal Compressed Wood," Wood and Fiber, 40, 362-373.

Lehmann, W. F. (1970) Resin efficiency in particleboard as influenced by density, atomization, and resin content. Forest Prod. J. 20(11):48–54.

Marra, A. (1992) Technology of wood bonding: Principles in practice. Van Nostrand Reinhold.

Melanitis, N., Galiotis, C., Tetlow, P. L., and Davies, C. K. L. (1993) J. Composites 24:459-466.

Nairn A. J. and Kim W. B. (2002) "Observations of Fiber Fracture and Interfacial Debonding Phenomena Using the Fragmentation Test in Single Fiber Composites," J. Comp. Mat., 36, 1825-1858.

Nairn, J. (2007) Numerical implementation of imperfect interfaces. *Computational Materials Science*, 40, 525-536.

River, B. (1991) Wood as an adherent. Marcel Dekker.

Robinson, I. M., Zakikhani, M., Day, R. J., Young, R. J., and Galiotis, C. (1987) J. Materials Science Letters 6:1212-1214 (1987).

Smith, G. (2003) The lap-shear strength of droplets arrays of a PF-resin on OSB strands. *Forest Prod. J.* 53(11/12):1-7.

Smith, G. 2003. A laboratory technique for coating strand with resin droplets of controlled size and spacing. *Forest Prod. J.* 53(7/8):70-76.

United State Department of Agriculture (1999) Wood handbook: Wood as an Engineering Material. USDA Forest Service. Forest Product Laboratory. FPL-GTR-113.

Youngquist, J. A., G. C. Myers, and L. L. Murmanis (1987) Resin distribution in hardwood: evaluated by internal bond strength and fluorescence microscopy. Wood Fiber Sci. 19(2):215–224.

U.S. Department of Agriculture (1987) Wood Handbook. Agriculture Handbook No. 72, Superintendent of Documents, Washington D.C. 466pp.

Verpoest, I., Desaeger, M., and Keunings, R. (1990) *Controlled Interphases in Composite Materials,* 653-666.

CHAPTER 3 – NUMERICAL SIMULATION OF WOOD-STRANDS AND WOOD-BASED COMPOSITES: PART 1. EFFECT OF GLUE-LINE INTERFACE AND STRAND UNDULATING ON MECHANICAL PROPERTIES

Abstract

The use of wood-strand composites, such as oriented strand board (OSB) and oriented strand lumber (OSL) is increasing for structural applications. In order to meet this high demand, maintain mechanical strength and stiffness, and lower costs, manufacturers need to look at all aspects from material costs, logging, and processing to factors that contribute to the final mechanical properties. One way to increase stiffness of panels may be to increase the amount and the quality of the resin but this will increase cost. Choosing the optimum resin consumption while maintaining mechanical performance is thus very important in the development of wood-strand composites.

In this study, we focused on the effect of the glue-line (amount and type of resin) on the mechanical properties of wood-strand composites. To study strand undulation, the properties were also investigated as a function of the amount of compaction of a realistic strand mat into an OSB structure. Strand undulations developed as the mat compacted.

Modeling the compression of wood strands and wood based composites was done using an emerging numerical method called the material point method (MPM). The mechanical properties of individual strands and the glue line properties were determined by experiment and used as input to the numerical model. To help interpret the importance of glue-line properties and undulating strands, a simple homogenized rule of mixtures (HROM) was developed for OSB and OSL structures. The results of MPM were compared to the HROM model. The results show that typical glue properties have a significant effect on mechanical properties of OSB. Furthermore, the role of the interface in tension properties is greatly amplified by strand undulation in typical OSB structures.

3.1 Introduction

There is increasing demand for wood-based composites as structural materials for residential and commercial applications such as oriented strand boards (OSB), oriented strand lumber (OSL), plywood, laminated veneer lumber (LVL), glue-lam and I-beams. Wood-based composites can be used as sheathing, in cases of OSB and plywood, or as beams for high load members, such as glue-lam beams and I-beams. These composites need to have high stiffness and strength while maintaining low cost of manufacturing. Therefore, modeling the mechanical properties and understanding the factors that control them is very important for designing wood composites for specific applications.

Most wood-based composites that are used in structural applications are subjected to bending loads. Many failures in bending of wood-based composites occur by the failure in tension first then in compression (Bond and Jayne 1982). Moreover, most of the literature on wood-based composites reports the mechanical properties as modulus of elasticity (MOE) and strength (modulus of rupture [MOR]) measured using bending tests. Therefore it is important to look at wood-based composites subjected to loads both in tension and in bending.

The mechanical properties of wood-strand composites depend on the properties of the wood-strands, the adhesive, and how the strands are bonded together (Wood Handbook 1999). The orientation of the strands, surface roughness, and voids in the wood can contribute to the bonding (Wood Handbook 1999). This bonding consequently affects the overall mechanical properties of wood-strand composites. As previously studied, the wood strands are the major contributor to the mechanical properties (Suchsland 1972, Price 1976, Geimer et al 1985, Lee and Wu 2003). These strand properties depend both on initial strand properties and how the strands are processed. Due to microcracks that may be produced during processing and other effects in fabrication, the tensile properties of strands can be reduced as much as 50% compared to solid wood properties (Price 1976, Geimer et al 1985). Similarly, processing pressures may compress cell walls and alter strand properties in the composite (Kortschot et al 2005). It is very difficult to observe or study these effects experimentally. Therefore, computer simulation

can be a useful tool for studying the effects of bonding, densification, and processing on morphology and/or mechanical properties of the final product.

Little research has been conducted on modeling mechanical properties of wood-strand composites. An early study by Hunt and Suddarth (1974) predicted tensile modulus of elasticity and shear modulus of medium-density homogenous flake board using a linear elastic finite element analysis together with Monte Carlo methods. The model under estimated the experimental tensile modulus by 8% for aspen and 6% for Douglas fir, whereas the shear modulus was overestimated by 20% and 13% for aspen and Douglas fir, respectively. More recently, Triche and Hunt (1993) developed a linear elastic finite element model capable of predicting the tensile strength and stiffness of a parallel, aligned, wood-strand composites with controlled geometry. The model considered each strand to have three layers of pure wood, resin and an interface. The properties of the individual constituents were used as input. Excellent accuracy for the predicted modulus of elasticity was reported (from 0.0% to 11.1% error). However, predictions of maximum stress were inconsistent and in as least one case unacceptable (from 1.2% to 1001.1% error). Cha and Person (1994) developed a two dimensional (2D) finite element model to predict the tensile properties of a three-ply veneer laminate, consisting of an off-axis core ply of various angles. Good agreement was obtained between predicted and experimental strains at maximum load. Recently, Wang and Lam (1998) developed a three-dimensional (3D), nonlinear, stochastic finite element model to estimate the probabilistic distribution of the tensile strength of parallel aligned wood-stand composites. The model was based on longitudinal tensile strength and stiffness data of individual strands. The model was verified through comparison of predictions to experimental data for four- and six-ply laminates. Clouston and Lam (2001) modeled strand-based wood composites using a nonlinear stochastic model to simulate the stress-strain behavior.

All prior research, such as Wang and Lam (1998), focused on linear elastic constitutive theory and none has considered the effect of the bond-lines or the structure that develops during processing. Previous studies have not accounted for the effect of compaction during the processing of strand-based composites; which is unrealistic for

composites such as OSB and OSL. In other word, none of these models are capable of accounting for undulating strands with realistic morphologies seen and many composites.

Considerable research has been done on the influence of controlled fiber waviness on the elastic behavior of synthetic composites produced with woven fabrics or unidirectional fibers. Ishikawa and Chou (1983) analyzed the effects of fiber undulation on the elastic properties of woven fabric composites using a 1-D model and concluded that it leads to softening of the in-plane stiffness. Yadama et al (2005) studied elastic properties of wood-strand composites with undulating strands. They concluded that strand undulation degraded Young's modulus of yellow-poplar laminates in both tension and compression, with more severe effects in compression. The experimental results from compression tests were in good agreement with the predictions.

In this study, the mechanical properties for strands that were determined by experiment were used as an input for numerical modeling. The interfacial stiffness properties were also measured in a previous study (Nairn and Le 2009 and Chapter 2) and used here as an input for numerical simulations. The mechanical properties of strand-based composites were then simulated as a function of glue-line interface for different levels of compactions. A new numerical technique was used in this study called the material point method (MPM). This numerical method is able to handle contact between strands (needed to model compaction), glue-line effects between strands, strand undulation and strand compaction. It has previously been shown to work well with other complicated compaction problems (Nairn 2006, Bardenhagen et al 2004) and for problems with imperfect interfaces (Nairn 2007E).

3.2 Numerical Simulation by Material Point Method (MPM)

Finite element analysis (FEA) is a common method for numerical modeling of structures but FEA has difficulty modeling realistic wood specimens (Bardenhagen et al 2005, Nairn 2007). The structure of wood is complex and it is very difficult to discretize such structures into an FEA mesh. FEA is also limited in dealing with the details of failure mechanics of such structures (Smith et al 2003). Furthermore, the densification of wood-based composites involves contact between strands in OSB. Although contact

methods are available in FEA, they are not fully developed for analysis of arbitrary contact. As a result, it would be difficult to mesh contact elements within realistic structures such as between wood strands in wood-based composites.

The material point method (MPM) has been developed as a numerical method for solving problems in dynamic solid mechanics (Sulsky et al 1994, Sulsky et al 1995, Sulsky and Schreyer 1996, Zhou 1998). In MPM, a solid body is discretized into a collection of points. As the dynamic analysis proceeds, the solution is tracked on the material points by updating all required properties such as position, velocity, acceleration, stress state, etc. The equations of motion are solved with the aid of a background grid. The grid remains fixed and thus does not distort at large deformation. A problem in early MPM (Sulsky 1994) was development of numerical noise when displacements became large enough that particles crossed element boundaries in the grid. This issue can be solved using the generalized interpolation material point method (GIMP) (Bardenhagen and Kobe 2005) (see Appendix).

This combination of meshless (the particles) and meshed (the grid) methods has proven useful for solving problems that are difficult for FEA such as compaction (Bardenhagen at al 2000), fluid-structure interactions (Guilkey at al 2004), wood densification (Nairn 2006), arbitrary crack propagation (Nairn 2003, Guo and Nairn 2004), torso injuries for soft tissue failure (Ionescu et al 2006), and elastic-decohesive model to model dynamic sea ice (Sulsky et al 2006).

The Material Point Method (MPM) is an extension to solid mechanics of a hydrodynamics code called Fluid-Implicit Particle (FLIP), which evolved from the Particle-in-Cell method dating back to pioneering work of Harlow (1964). MPM uses a background grid and is frequently compared to Finite Element Method (FEM). A GIMP derivation of MPM (Bardenhagen and Kober, 2004), however, shows it to be a Petrov-Galerkin method (Atluri and Shen 2002, Belytschko et al 1994) that has more similarities with meshless methods. Unlike conventional computational mechanics methods, MPM does not use rigid mesh connectivity like in FEM, Finite Difference Method (FDM), Boundary Element Method (BEM) or Finite Volume Method (FVM). The meshless

aspect of MPM derives from the fact that the body and the entire solution are described on the particles while the grid is used solely for calculations.

Unlike, FEA, MPM does not require remeshing steps and remapping of state variables, and therefore is better suited to the modeling of large material deformations such as high levels of compaction seen in OSB processing. In MPM it is very easy to discretize complex geometries of materials compared with mesh generation needed for numerical techniques such as FEM. Because of the fixed regular grid employed by MPM, it eliminates the need for costly searches for contact surfaces needed by FEM (Xue et al 2006). The meshless features of MPM have advantages for simulation of transverse compression in wood (Nairn 2007) and wood-based composites compaction (such as OSB [oriented strand board] and OSL [oriented strand lumber]).

The goal of this study was develop the Material Point Method (MPM) as a potential tool for numerical modeling of wood-based composites that is capable of modeling many details of wood-based composites processing to predict mechanical properties during OSB compaction. The idea for use of MPM on wood was derived from the recent successful application of MPM to 3D foams (Bardenhagen et al 2005, Brydon et al 2005) and wood densification (Nairn 2006). They demonstrated that prior problems associated with numerical modeling of compaction are less severe when using MPM (Bardenhagen et al 2005). MPM automatically handles contact and can be applied to high strain for compaction of OSB without numerical difficulty. It had been shown by Nairn (2006) that MPM can handle realistic structures such as wood-based composites.

3.2.1 Disadvantages of MPM

MPM is more expensive in terms of storage than other methods, as MPM makes use of a mesh as well as particle data. There are also spurious oscillations that may occur as particles cross the boundaries of elements in the MPM grid, although this effect can be minimized by using generalized interpolation methods (GIMP). Oscillations also occur if the time steps are too large or too small. Oscillations can sometimes be minimized by various damping methods or material constitutive laws.

3.3 Mechanical Properties of One Strand

Nairn (2006) used MPM to study the transverse compression of wood in the radial and tangential directions. Similarly, much of the early work of Gibson and Ashby (Gibson et al 1982, Gibson and Ashby 1997) focused on densification of foam and cellular materials. Transverse compression is an important phenomena in compaction of an OSB panel.

3.3.1 Compression Stress-Strain Law and Power Law

During the compression of wood in the transverse direction, it first behaves as an elastic material then as a plastic material (or elastic buckling) and finally there is a densification regime. Figure 3.1 shows idealized experimental stress versus strain curves for wood (aspen) in transverse compression (Tabarsa and Chui 2000). Figure 3.2 shows implementation of this behavior in the MPM model. These curves were generated by incorporating a power-law (Simo and Hughes 1997) into an elastic-plastic material with an anisotropic Hill yielding criterion (Hill 1948). Further discussion of this Hill plastic is discussed in the next section. The assumed work hardening law gives yield stress as a function of plastic strain in the form:

$$\sigma_Y = \sigma_0 + K\varepsilon_p^{\,n} \qquad (3.1)$$

where σ_Y, σ_0 and ε_p are yield stress, initial yield stress, and equivalent plastic strain. K and n are constants that determine the plastic behavior and the curvature of the stress-strain relation. In Figure 3.2, several pairs of n and K were run to get the approximate stress values of ~30MPa at 50% strain, which matches typical experimental values from Gibson and Ashby (1982), Steiner and Simon (2002), and Tabarsa and Chui (2000). The pair of n=4 and K=120 MPa was used for all subsequent calculations in this study because it was judged to be close to results on real wood specimens (Steiner and Simon 2002, Tabarsa and Chui 2000).

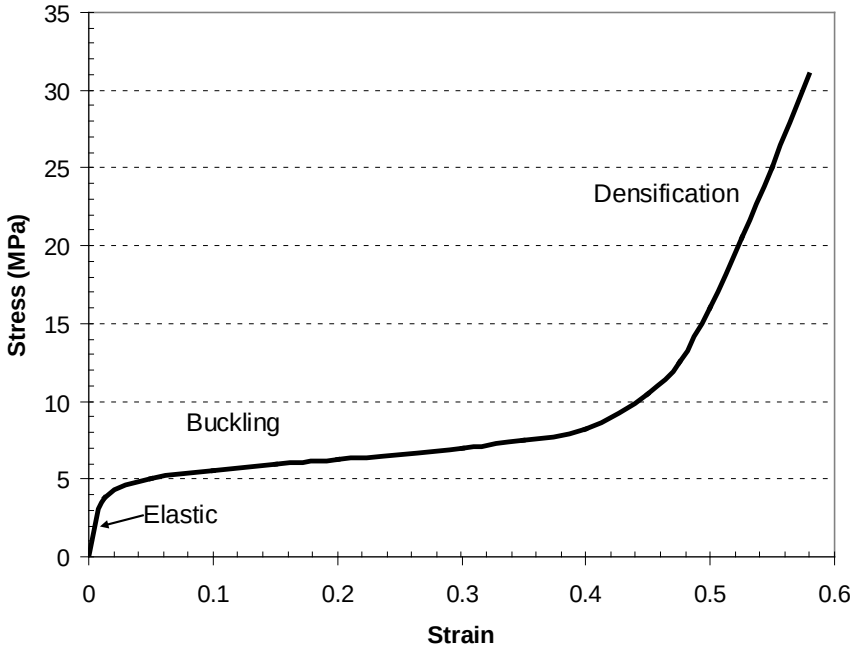

Figure 3.1. Experiment stress strain for wood (aspen) in transverse compression (digitized from plot in Tabarsa and Chui 2000).

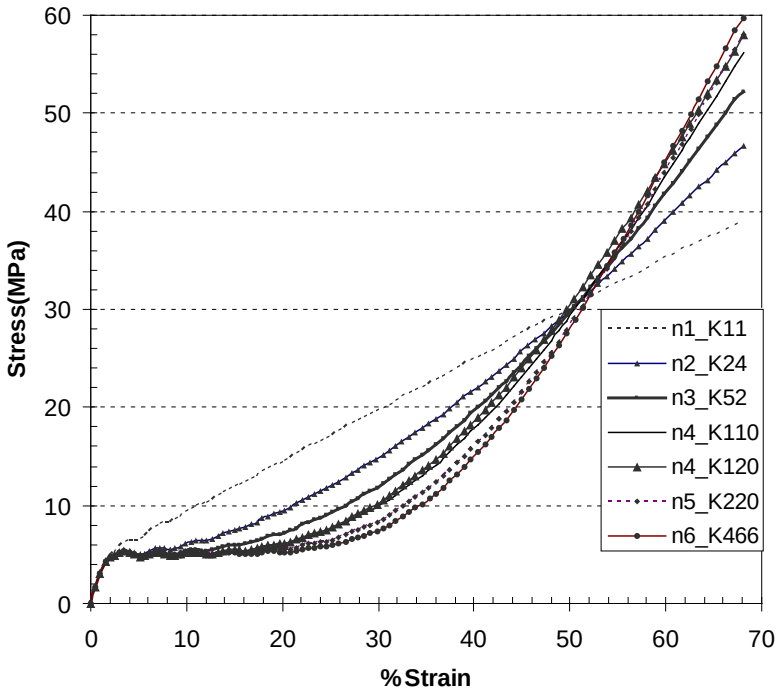

Figure 3.2. Stress versus strain for different core strand properties (n, K).

3.3.2 Hill Plasticity Material (Model)

All of the previous material studies of wood composites (such as on OSB, PSL, I-beam) have used Finite Element Analysis (FEA). Bai et al. (1999) modeled the behavior of Moso bamboo-reinforced OSB composite beams. In the model, OSB was assumed to be an elastic-orthotropic material. The study focused on flexural behavior as related to the combined effects of bamboo, OSB, and the adhesive layers. Moris et al (1995) developed a two dimensional FEA model to predict the shear strength of OSB webbed I-beams with and without a circular opening. OSB was treated as a linear elastic orthotropic material and a Tsai- Hill failure criterion was applied in tension while the compressive strength and yield of OSB were neglected. Saliklis and Mussen (2000) investigated the buckling behavior of OSB panels using the FE method. OSB was modeled as an elastic orthotropic material in an eigenvalue buckling analysis, and in a nonlinear buckling analysis it was modeled as a bilinear elasto-plastic material with the second portion of the constitutive curve having either a small or a zero modulus. The yield stress was taken to be 95% of the ultimate stress. Guan et al (2005) used an elastic-plastic stress-strain relationship to develop an FE model to simulate OSB in compression and in tension. A parabola-like curve between initial yield and the ultimate stress, which represents the nonlinear stress-strain relationship of OSB was developed.

In this study plasticity of the strands was modeled using J_2 plasticity theory (Simo and Hughes 1997), an anisotropic Hill yielding criterion (Hill 1948), and the power-law work hardening term (Simo and Hughes 1997) from the previous section. The plain strain plastic potential for this material response was

$$f = \sqrt{\left(\frac{\sigma_x}{\sigma_x^Y}\right)^2 + \left(\frac{\sigma_y}{\sigma_x^Y}\right)^2 + \left(\frac{\sigma_z}{\sigma_z^Y}\right) - F\sigma_y\sigma_z - G\sigma_x\sigma_z - H\sigma_x\sigma_y + \left(\frac{\tau_{xy}}{\tau_{xy}^Y}\right)^2} - (1 + K\varepsilon_p^n) \tag{3.2}$$

where σ_i and τ_{xy} are the normal and shear stresses in the material's axis system, σ_i^Y is the tensile yield stress in material direction *i*, and τ_{xy}^Y is the shear yield stress in the material's x-y plane,

$$F = \frac{1}{\left(\sigma_y^Y\right)^2} + \frac{1}{\left(\sigma_z^Y\right)^2} - \frac{1}{\left(\sigma_x^Y\right)^2},\ G = \frac{1}{\left(\sigma_z^Y\right)^2} + \frac{1}{\left(\sigma_x^Y\right)^2} - \frac{1}{\left(\sigma_y^Y\right)^2}, \text{ and}$$

$$H = \frac{1}{\left(\sigma_x^Y\right)^2} + \frac{1}{\left(\sigma_y^Y\right)^2} - \frac{1}{\left(\sigma_z^Y\right)^2} \qquad (3.3)$$

This potential predicts yielding to occur when $f = 0$. The hardening parameters are *K* and *n*, and ε_p is the cumulative equivalent plastic strain that evolves during the computation (Simo and Hughes 1997).

The properties assumed for unmodified wood and for VTC wood are listed in Table 3.1. The longitudinal moduli for strands were measured. Other properties were estimated by scaling to similar properties in solid wood (Bodig and Jayne 1982). The transverse yield stresses (σ_R and σ_T) of unmodified strands were taken from typical wood properties. The transverse yield stresses for VTC strands were estimated using yield strength scaling laws with density given by cellular mechanics theories (i.e. σ_Y scales with cube of the density [Gibson et al 1982]). The hardening parameters were not measured, but were chosen to match transverse compression stress-strain curves for solid wood with a plateau in stress followed by rapid increase in the stress after about 30% compression strain (Nairn 2006, Steiner and Ellis 2002, Tabarsa and Chui 2000)

Table 3.1: Mechanical properties for unmodified and VTC strands.

Property in MPa	Unmodified Strands	VTC Strand
E_L	9936	24311
E_R	914	2153
E_T	427	1005
G_{RL}	745	1616
G_{TL}	686	1486
G_{RT}	109	235
μ_{RL}	0.028	0.028
μ_{TL}	0.017	0.017
μ_{TR}	0.33	0.33
σ_L(yield)	∞	∞
σ_R(yield)	5	5
σ_T(yield)	5	5
σ_{RT}(yield)	2.5	10

Because the L direction is the fiber direction it will have much less yielding than the transverse direction. Here we assumed no axial yield which was achieved by having σ_L set to ∞ (see Table 3.1). Since the compaction is in the transverse direction (radial or tangential directions), there is not expected to be L direction yielding. According to Hill criteria (and its need for square root term in Equation 3.2 to be real and positive), an assumption that $\sigma_L = \infty$ implies the σ_R and σ_T must be the same. To model wood with σ_R and σ_T different using the Hill method would require use of a finite value of σ_L.

3.4 Glue-Lines

3.4.1 Interface of the Glue-Lines

The thin adhesive lines were modeled using imperfect interface methods for composite stiffness (Hashin 1990, Nairn 1997). The model deals with adhesive bond lines between strands by creating a crack/interface between the strands. The D_t interfacial

properties are then treated as a crack line property. These interfaces allow displacement discontinuities, [u] to develop between neighboring strands. The magnitude of discontinuities is proportioned to shear stress at the interface as $[u] = \frac{\tau}{D_t}$. A perfect interface means zero discontinuity ($D_t \rightarrow \infty$) and a debonded interface means zero interfacial stress ($D_t \rightarrow 0$). The interfacial properties of PF as a function of adhesive coverage were obtained from experiments, as described in Nairn and Le (2009) and in the previous chapter. Here $1/D_t$ was varied from $1/D_t = 0$ to values of few times greater than $1/D_t$ (1%) where D_t (1%) is the value measured for 1% PF resin coverage.

3.5. Simulation of OSB

3.5.1 Model Composites

MPM simulations were performed on two classes of composites utilizing NairnMPM code (Nairn 2003). Details of the MPM algorithm can be found in (Nairn 2003). An anisotropic elastic plastic model constitutive material using the Hill yield criteria has been implemented in the NairnMPM code for these plane-strain 2D simulations (see previous section).

Commercial OSB mats consisted of three different layers. The top layer had 25% of the strands, the core layer had 50% of the strands, and the remaining 25% of the strands were in the bottom layer. The grain directions of the top and bottom layers were parallel to each other and perpendicular to core layer. For surface strands, the initial *x-y-z* directions were the *L-R-T* directions (for longitudinal, radial, and tangential) of the wood. For the core strands, the initial *x-y-z* directions were the *T-R-L* directions of wood. Thus, for these 2D, x-y plane-strain analyses, the core strands had the transverse plane of the strands. To account for strand undulation, the rotation of the materials's *x* direction to its initial *x* direction was tracked throughout the simulations (i.e. rotation about the z axis).

For simulations of OSL, all layers were the same and had parallel grain directions. In other words all strands were like surface strands in OSB.

The process for modeling OSB and OSL was as follows:

1. Individual layers of a strand mat were created by laying down strands separated by gaps where strand lengths and gap spacings were randomly selected using input averages and standard deviations for lengths and gap spacings.

2. Stacking together layers of strands and gaps from step 1 created a full strand mat. For OSB, the surface layers had strand grain direction along the x axis of the analysis and radial direction along the y axis. The core strands had radial direction along the y axis and grain direction perpendicular to the analysis plane (z direction). Figure 3.5A shows an uncompacted strand mat created by this process. The volumes of surface and core layers were equal with half the surface layers being on each surface of the OSB. For OSL there was no core layer. Instead OSL specimens had only surface layers.

3. An MPM simulation was used to compact the strand mat. The individual strands were modeled as an anisotropic elastic-plastic material (Hill yielding criterion [Hill 1948]) with work hardening. Figure 3.5A-D shows stages of a strand mat that has been compacted from 0% to 40%. During the simulation, the analysis tracked the surfaces (as cracks) between the strands and tracked the local grain angles as the strands developed undulation. Figure 3.3 shows the average strand stress versus global strain ($\Delta h / \Delta h_o$) for commercial OSB for several different runs. Figure 3.4 is a zoom-in of the early part of Figure 3.3. The value of the yield stress is lower than for solid wood (Figure 3.2) because yielding starts at the first location that reaches the yield stress while the average stress will be lower; it is lower because of all material that has not yet yielded. At high strain, the stress increase due to work hardening and densification.

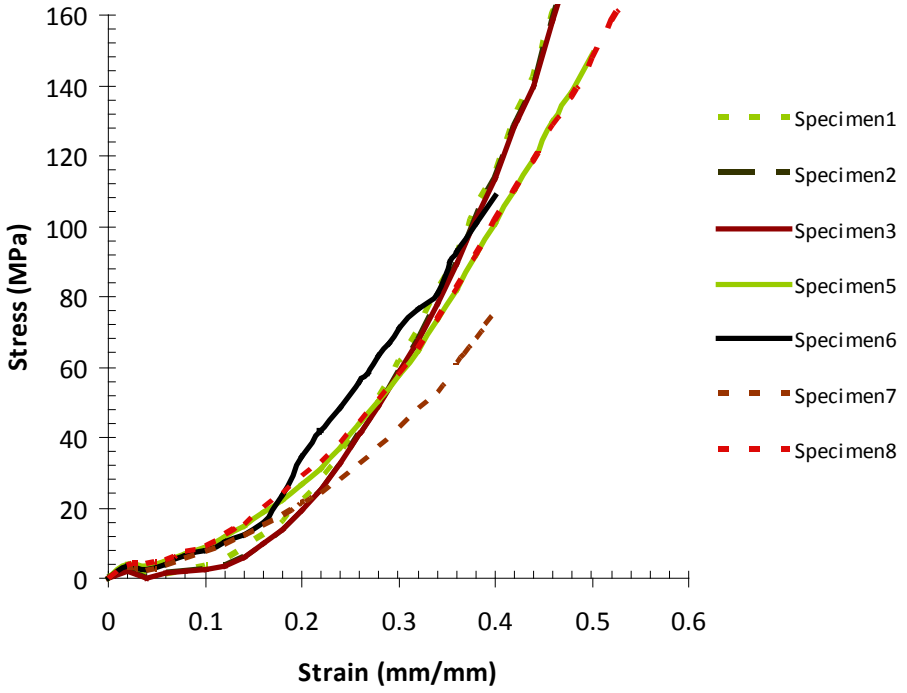

Figure 3.3. OSB stress versus strain for different specimen.

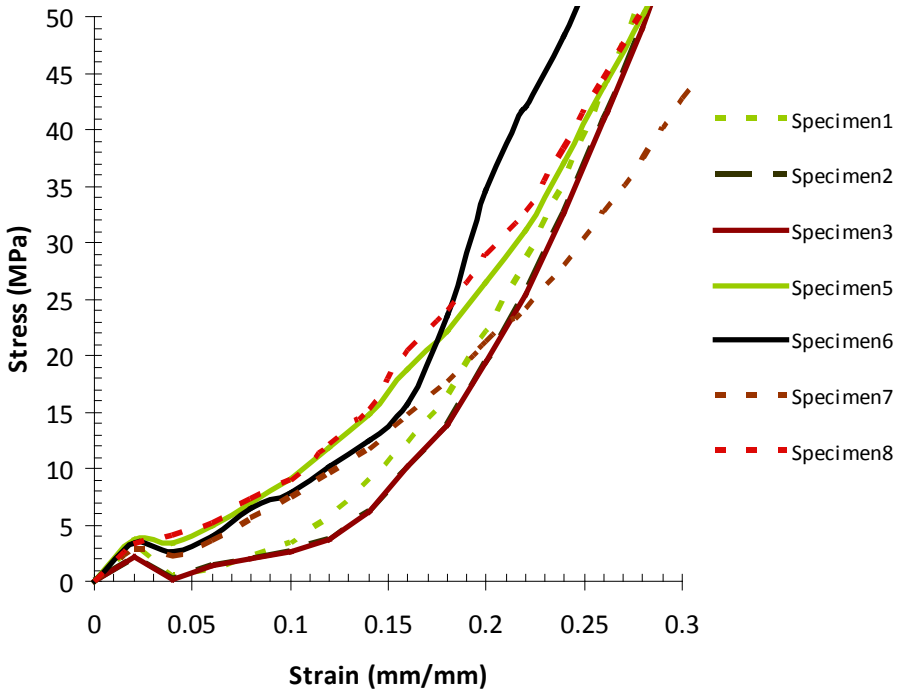

Figure 3.4. Zoom-in of Figure 3.3.

4. Finally, the particle locations of the compacted mats were input into a new MPM simulation for tensile loading (in the horizontal direction of Figure 3.5). The tensile simulation used fiber angles from the undulating strands and implemented imperfect interfaces between strands using imperfect interface methods for MPM (Nairn 2007A). The numerical calculations gave tensile properties as a function of mat compaction and interface parameter D_t. The various values of D_t spanned the range from perfect interface ($1/D_t = 0$) to beyond experimental results for D_t of PF resin (Nairn and Le 2009).

5. Because the mats were randomly created, all simulations were repeated for five randomly selected initial mat structures. Error bars of some curves show standard deviation or 95 percent confidence interval range of modulus results from the various structures.

For numerical temporal convergence, the MPM time step was set to 0.4 d/c, where d is the dimension of the elements in the background grid and c is the maximum wave speed in the strand. For wood, the maximum wave speed is in the longitudinal direction and for unmodified and VTC strands it is:

$$V = \sqrt{\frac{E}{\rho}} = \sqrt{\frac{9.936GPa}{350kg/m^3}} = 5328m/s \text{ and } V_{VTC} = \sqrt{\frac{E}{\rho}} = \sqrt{\frac{24GPa}{910kg/m^3}} = 5136m/s.$$

Four material points were used for each background element or cell. For spatial convergence, there has to be a sufficient number of particles in the thickness direction of each strand. The simulations that were first tried had one cell or two particles in the thickness direction, but the results did not work well. They failed to resolve the glue-line. We then moved to 4, 6 and 8 particles. The simulations with 6 and 8 particles gave reasonable and similar stress, strain and strand undulation at higher levels of compaction. However, the simulations with 8 particles took too long to finish. Therefore, all simulations used 6 particles (3 cells) across the thickness of each strand.

The OSB structures were generated based on the strand length, and width, strand gaps, and their standard deviations. In this study (this chapter), the strand length was 150 mm with standard deviation of 20 mm. The strand end to end spacing or gap was 15 mm with standard deviation of 4.95 mm. In the core plies, the strand width was 25 mm with standard deviation of 3 mm. The strand side-to-side spacing or width gap was 10 mm with standard deviation of 1 mm. Figure 3.5 shows a sample MPM simulation of commercial OSB at different levels of compaction, from 0 percent compaction to 40 percent compaction. There was more undulating of strands as the level of compaction increased.

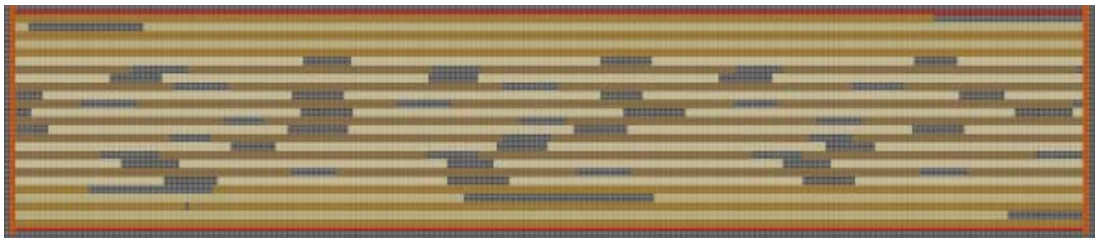

a) 0% compaction

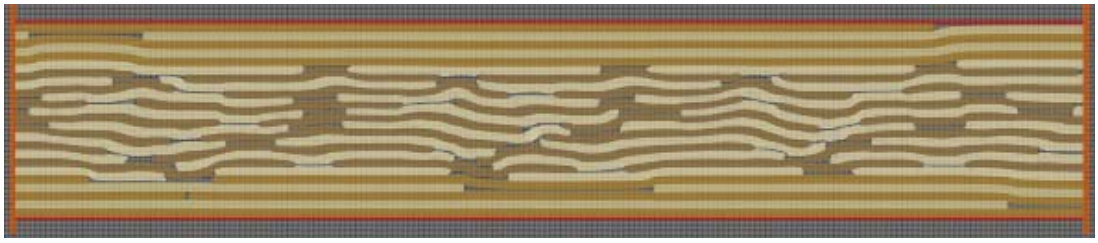

b) 10% compaction

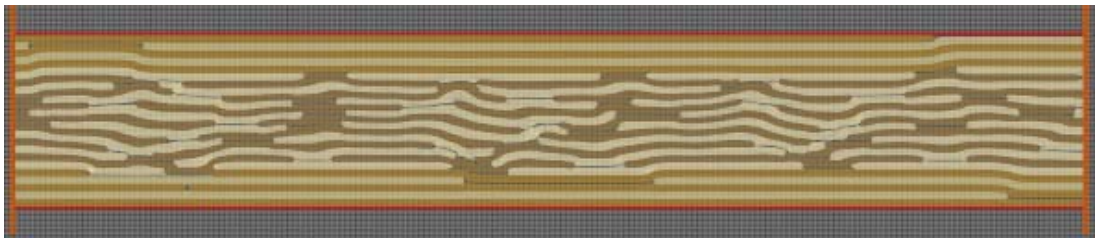

c) 20% compaction

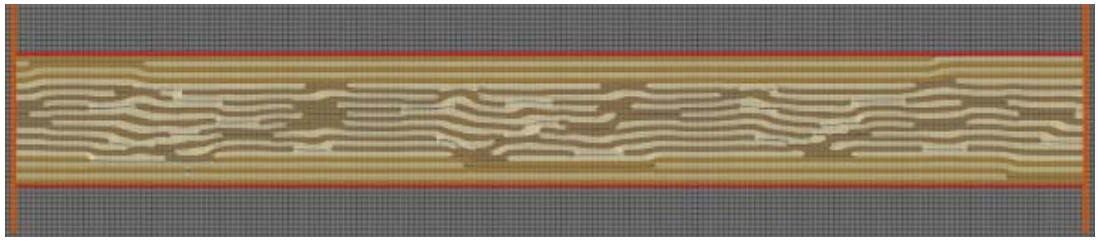

d) 40% compaction

Figure 3.5. Sample simulation of OSB at different levels of compaction.

3.5.2 Tension Method

The OSB structures were compacted to different levels of densification with the rate of 2m/sec. Archives of MPM results were saved at increments of 2% compaction. The output of mat structures for specific levels of compaction were then simulated by loading them in tension. The loading in tension was done for compactions of 0%, 10%, 20%, 30% and 40%. The tension results were used to find OSB tensile modulus. To keep

the tension test in the elastic region, the tensile load was applied only for very small strain and the plastic energy was tracked during the analysis. During elastic loading, the total elastic energy for a composite with imperfect interfaces is (Hashin 1990):

$$U_{tot} = \int_V \frac{1}{2}\sigma C \sigma dV + \int_{S_{\text{int}}} \frac{1}{2} D_t [u_t]^2 dS \qquad (3.4)$$

where U_{tot} is the total energy that includes elastic strain energy (first term) and interface energy (second term), V is volume, C is stiffness matrix, σ is stress tensor, S_{int} is interfacial surface area, D_t interfacial stiffness parameter, and $[u_t]$ is slippage (displacement) along the interface. The MPM output was set to record both the elastic strain energy and the interface energy. From the output, total potential energy was used to calculate the modulus of elasticity. By definition, the total energy during tensile loading is related to effective modulus in that direction, E_{eff}, by

$$U_{tot} = \tfrac{1}{2} E_{eff} \varepsilon^2 Lth \qquad (3.5)$$

where t is thickness =1mm, h is compressed height, and L is length of specimen in mm. Rearranging gives

$$E_{eff} = \frac{2U_{tot}}{\varepsilon^2 Lth} \qquad (3.6)$$

The output results for interfacial energy and elastic strain energy were summed and used to calculate modulus. Simulations were run for various D_t and for different levels of compaction. The results of elastic modulus as a function D_t for different levels of compaction are disused below.

3.5.3 Verify the Model

To verify the simulation method for MOE, a test simulation was run on a homogenous specimen with known MOE. Figure 3.6 shows an MPM model for a block of material loaded in tension in the x direction. The input MOE was 11000 MPa, Poison's ratio was 0.33 and density was 0.5 gram/cm^3. To calculate MOE, the strain energy was recorded (here there was no interfacial energy). Figure 3.7 plots effective elastic modulus

(MOE) by Eq 3.6 versus time. At early times there are dynamic effects. But after t = 0.021 sec, the effective modulus levels off and is close to the input MOE (11000 MPa). To understand the time to level off, the transit time for stress waves was calculated. The axial wave speed for a tensile stress wave is:

$$\boldsymbol{V}\approx\sqrt{\frac{E_A}{\rho}} \qquad (3.7)$$

where ρ is density and E_A is axial stiffness. The transit time is L/V, where L is the simulated specimen length (100 mm). This test run material (similar to wood) had ρ = 0.5 gram/cm^3, E_A = 11,000 MPa and L = 100 mm. Therefore the transit time is

$$\Delta t = \frac{L}{V} = \frac{L}{\sqrt{E_A/\rho}} = \frac{0.1m}{4690m/\sec} = 0.021m\sec$$

Thus the time to pass dynamic effects is similar to time it takes the stress wave to pass through the specimen. To get stable results, all simulations were run for multiple transit times (at least 4 or here at least 0.084 msec).

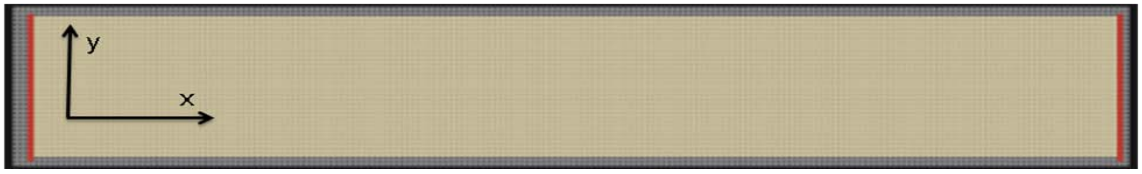

Figure 3.6. Test geometry of 0% compaction in tension of fixed one end (right) and rigid material on the other end (load end, left end), load rate 5m/second, cell size is dx=dy=0.2666 mm.

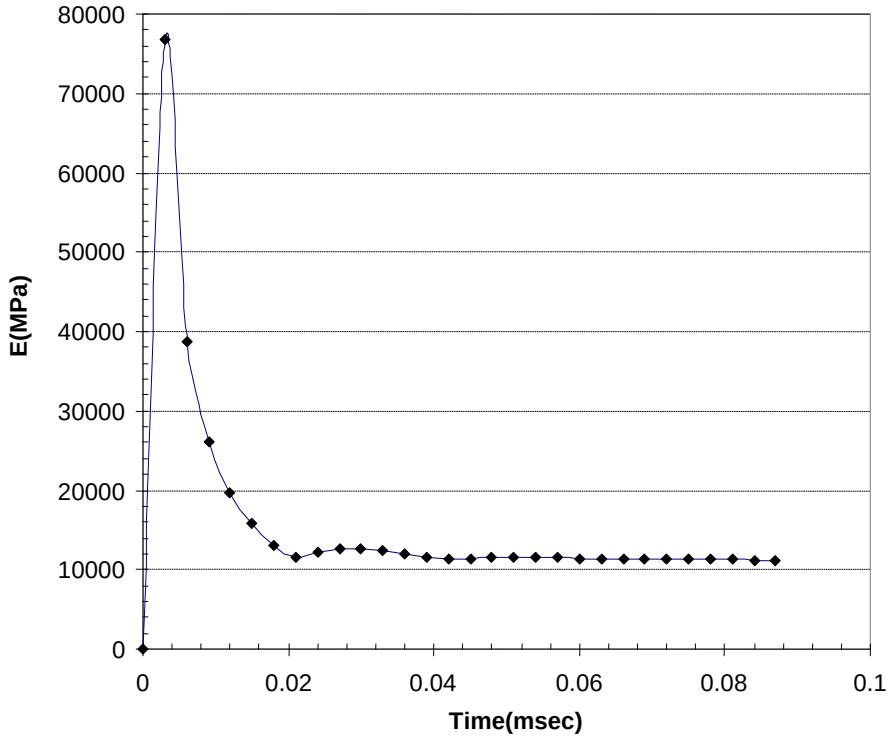

Figure 3.7. Simulated modulus as function of time.

3.6 Results and Discussion

3.6.1 Numerical Modeling of OSB

All calculations were done using two-dimensional, explicit MPM code called NairnMPM (Nairn 2005a). This serial code was run on dual-processor, Linux cluster nodes with 2.8GHz processor speeds. In explicit code, the time step is limited to $t_{step} \leq d/c_s$ where d is the minimal dimension of the elements in the background grid and c_s is the maximum wave speed of the typical hybrid poplar strand material. The longitudinal wave speed of the assumed hybrid poplar strand material was $c_s = (E/\rho)^{0.5} = (9.936\text{GPa}/350\text{kg/m}^3) = 5328\text{m/s}$ and typical element dimensions were d = 0.2666mm. The transverse wave speed of the assumed hybrid poplar strand material was $c_s = (E/\rho)^{0.5} = (0.425\text{GPa}/350\text{kg/m}^3) = 1102\text{m/s}$. Typical time steps were therefore based on the faster longitudinal wave speed and were about $5\text{x}10^{-6}$ms. These small time steps precluded simulations at typical loading rates used in OSB fabrication.

Work on compression of foam, however, shows that quasi-static results can be obtained provided the loading rate is lower than about 3% of the wave speed of the material (Bardenhagen et al 2005). The compaction of OSB was first run using 2m/sec (0.18% of transverse wave speed) but it took too long to finish (one month per calculation). Accordingly, the transverse compression in the radial direction of OSB specimen was then tried at 4m/s (0.36% of transverse wave speed), 8m/s (0.73% of transverse wave speed), 16m/s (1.45% of transverse wave speed), 32 m/s (2.9% of transverse wave speed) and 64m/s (5.81% of transverse wave speed) to compression ratio of 0.6. All these speeds were less than 1% of longitudinal wave speed and gave similar results. The compaction speed used to compact OSB panel was thus set to 32 m/sec (see chapter 6 for details on how compaction rate affects density profile) to give faster simulations with minimal artifacts due to loading rate.

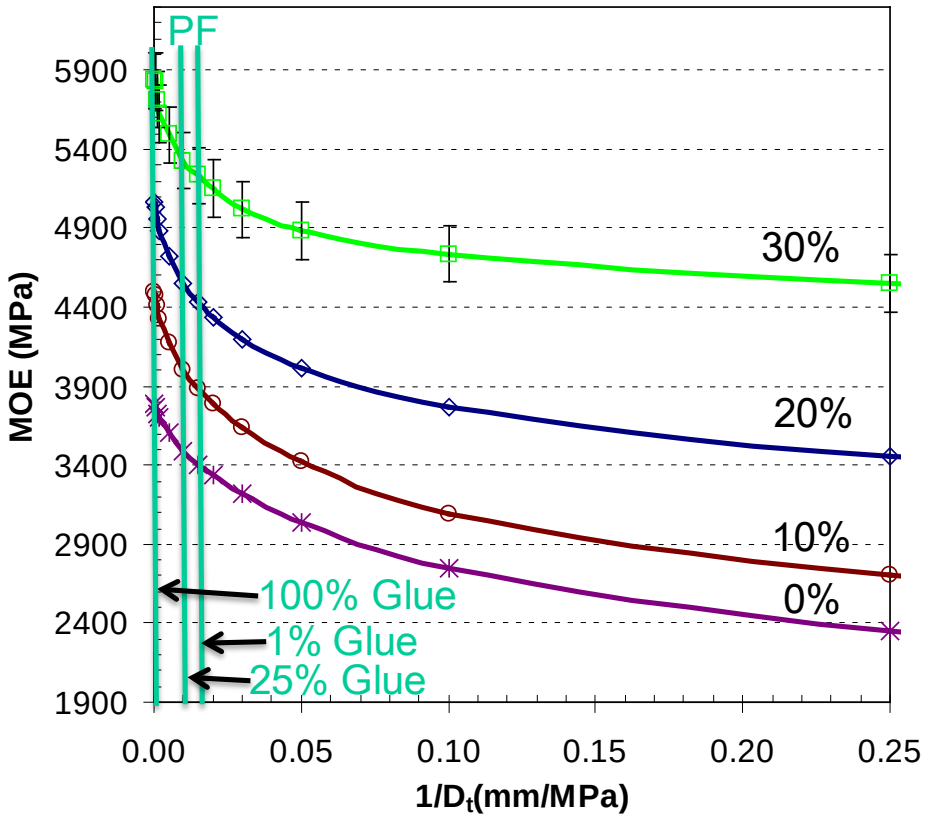

Figure 3.8. Simulation results of MOE versus $1/D_t$ at different levels of compaction with commercial OSB.

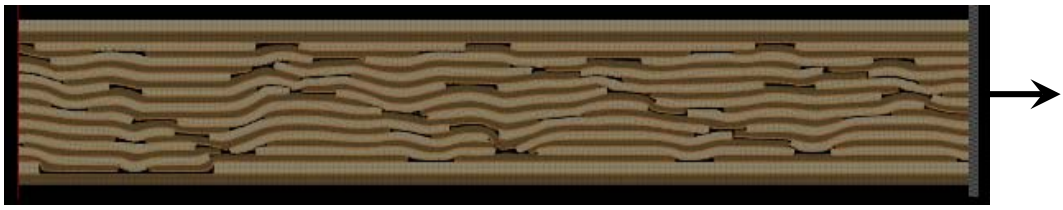

Figure 3.9. Sample simulation of OSB that loaded in tension.

Next, structures at selected compactions were input into new MPM simulations and loaded in tension. The loading rates were set to 5 m/sec which is 0.094% of longitudinal wave speed. Figure 3.9 represents tension test that was fixed on one end (left) and pulled on the other end (right end). A series of simulations were run with different values of D_t and MOE was found by the energy methods described before. Figure 3.8 and 3.10 shows the results of axial MOE versus $1/D_t$ as different levels of compaction for commercial OSB. Figure 3.10 is the zoom-in of Figure 3.8 for 0% to 30% compaction. As the level of compaction increased, MOE increased. Using experimental results for D_t (in previous study, chapter 2) for PF resins, if the strands are covered 1% (by area) with glue, the stiffness of the OSB panel would be about 14% lower than could be expected for a panel with 100% coverage and about 10% lower than it could be for 25% rather 100% coverage. In Figure 3.8, all the data in this plot are obtained from average of at least five runs. The error bars on one curve show the standard deviation of the results. There was little change in standard deviation for different values of $1/D_t$.

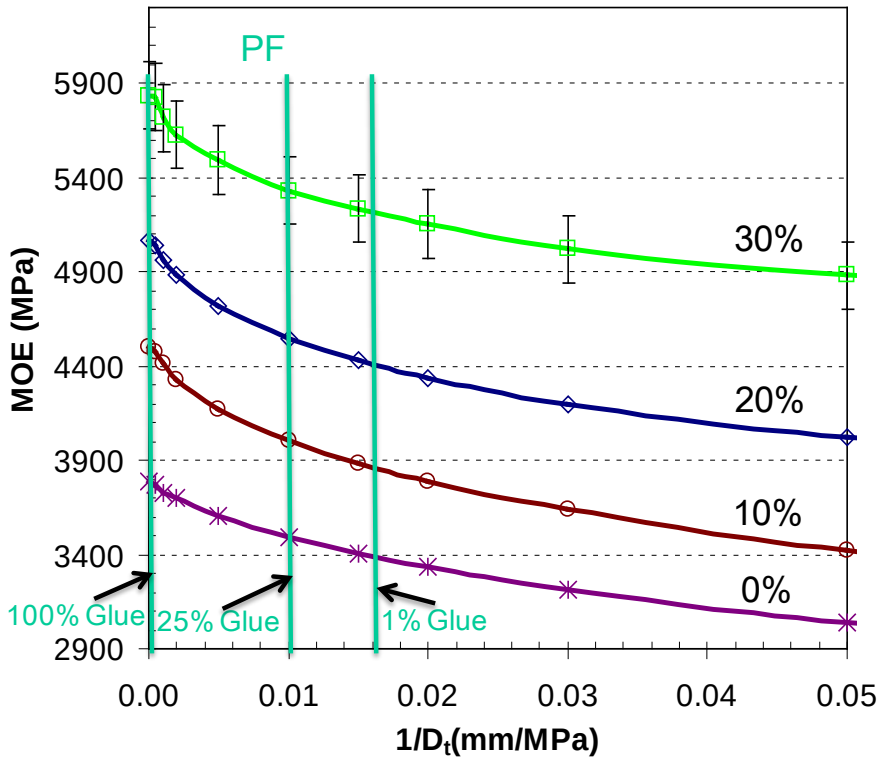

Figure 3.10. Simulation results of MOE versus $1/D_t$ at different levels of compaction with no VTC strands on face layers.

3.6.2 Numerical Modeling of OSL

For OSL simulations all strands were surface strands with grain direction in the x-axis direction. The total number of strands across the thickness was still 20. The strand length and gap spacing were the same as for surface layers of OSB. Figure 3.11 shows the results of MOE versus $1/D_t$ at different levels of compaction for unmodified strands. The same behavior is observed for OSL as for OSB. However, in this case MOE is much higher than in the case of OSB. This is due to the fact that the applied load in the direction of analysis is parallel to the longitudinal direction of the strands or parallel to the grain direction of the wood. Figure 3.11 also demonstrates that interfacial stiffness has a larger effect on mechanical properties in OSL than in OSB. There is about 34.5%

decrease in MOE between 100% and 1% glue coverage, about 17.2% decrease in MOE from 100% to 25% glue coverage and 3.6% decrease in MOE from 25% to 1% glue coverage. In Figure 3.11, all the data in this plot are obtained from average of at least five runs. The error bars on one curve show the standard deviation of the results. There was little change in standard deviation for different values of $1/D_t$.

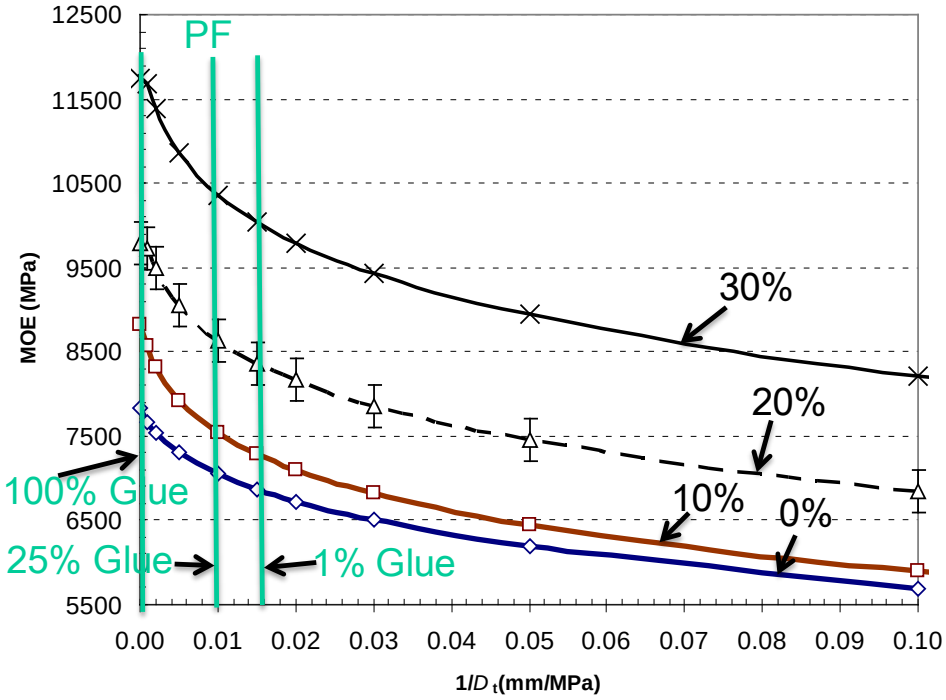

Figure 3.11. Simulation results of MOE versus $1/D_t$ at different levels of compaction for OSL.

3.6.3 Plywood – Numerical Modeling of OSB with No Gaps

If gaps are eliminated from the OSB simulations, the structure has continuous layers and is essentially a 3-layer plywood. When plywood is compressed, the layers densify, but there is no undulation (see Figure 3.12). These simulations with no gaps can assess the role of strand undulation in glue-line effects.

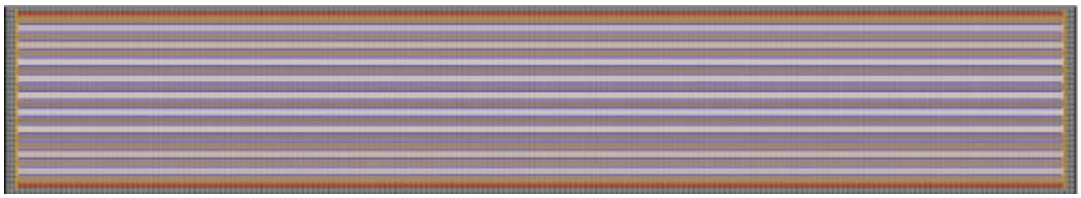

a) 0% compaction

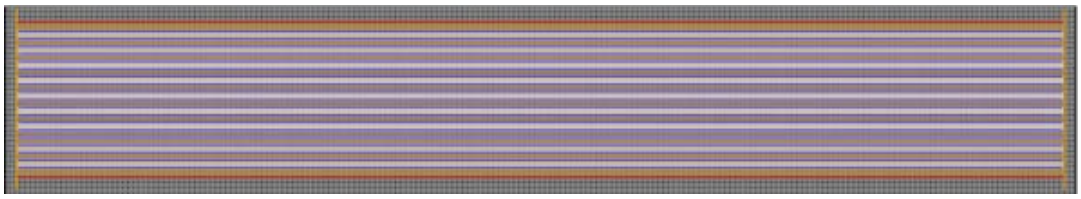

b) 10% compaction

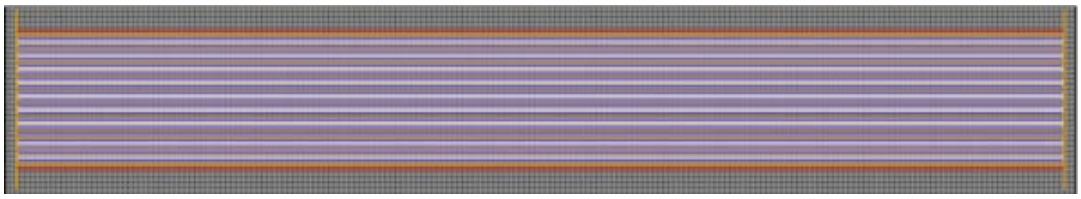

c) 20% compaction

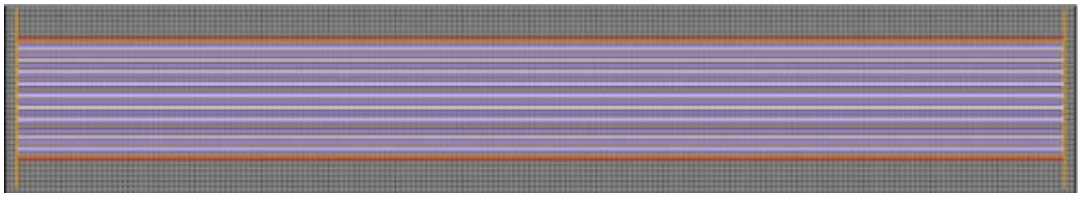

d) 30% compaction

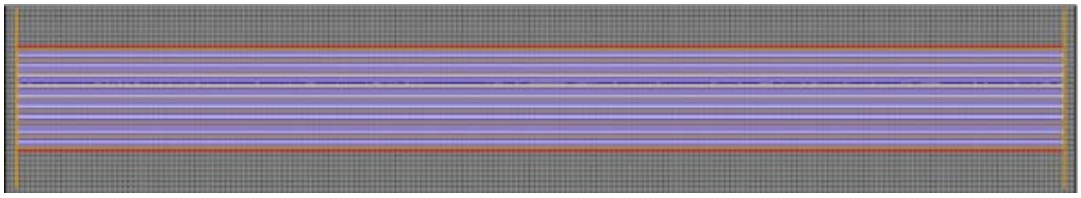

e) 40% compaction

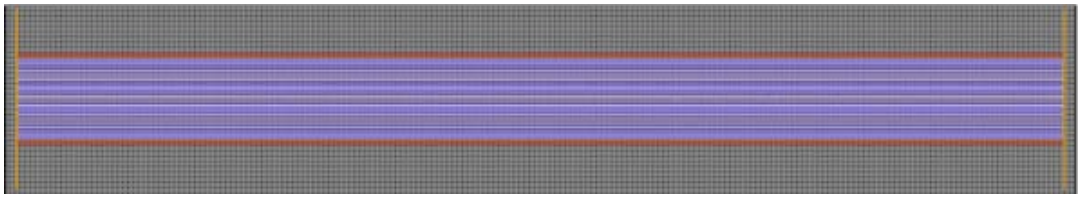

f) 50% compaction

Figure 3.12. Sample simulation of OSB with no gaps at different levels of compaction.

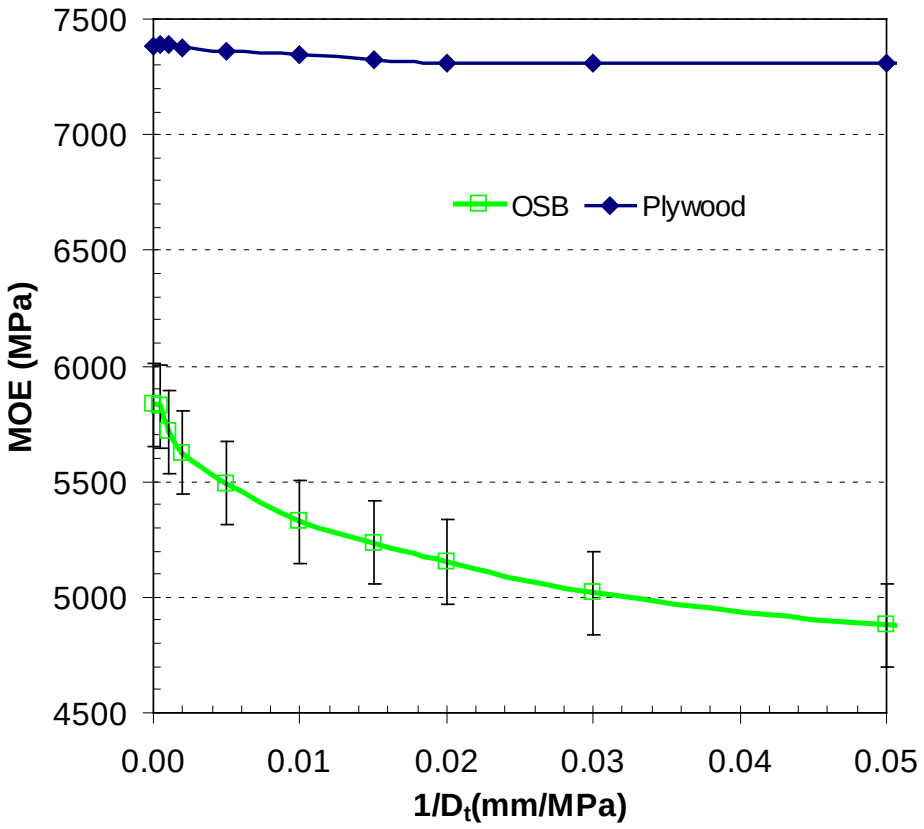

Figure 3.13. Simulated MOE versus $1/D_t$ for plywood and OSB at 30% compaction

Figure 3.13 shows results of axial MOE versus $1/D_t$ at 30% compaction for OSB and plywood. The plywood is just a special case of OSB with no gaps. In Figure 3.13 OSB results depended on the interface but plywood did not. As $1/D_t$ increased, plywood gave a straight horizontal line or was nearly independent of D_t. Furthermore, the MOE in tension for plywood was much higher than for OSB. Therefore, as the strand length increases and/or the gap spacing decreases, the mechanical properties of OSB will increase and approach the mechanical properties of the analogous plywood. In Figure 3.13, all data were obtained from an average of at least five runs. The error bars on the OSB curve show the standard deviations of these results. There are no error bar on plywood because only one structure could be analyzed (i.e., no way to repeat for different structures).

Similarly, if gaps are removed for OSL simulations, the structure is essentially LVL (laminated veneer lumber) and strand undulation stops. Figure 3.14 shows results of axial MOE versus $1/D_t$ at 10% compaction for OSL and LVL in tension. The mechanical properties of the LVL are higher than OSL. The error bars in Figure 3.14 on the OSL curve represents the standard deviation from average of five runs. As $1/D_t$ increased, LVL gave a straight horizontal line or was independent of D_t. Therefore, as the strand length increases and/or the gap spacing decreases, mechanical properties of OSL panel will approach the mechanical properties of LVL. In other words, they will improve and become less affected by D_t.

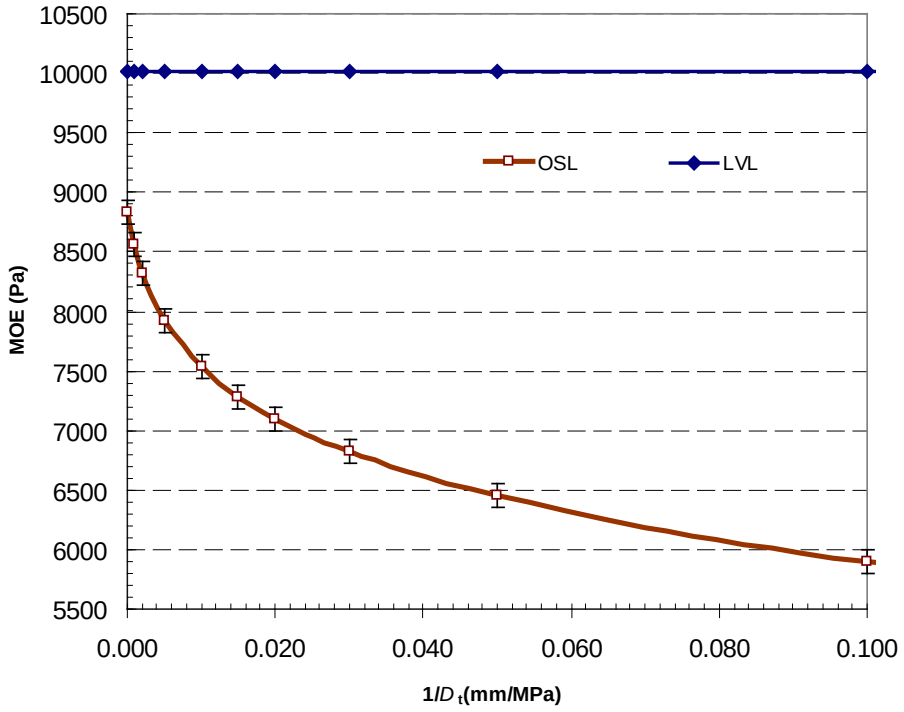

Figure 3.14. Simulated MOE versus $1/D_t$ for LVL and OSL at 10% compaction

3.6.4 Numerical Modeling of OSB with Surface VTC Strands

To study the effect of VTC strands on the mechanical properties of OSB panels, the surface layers were replaced by VTC strands. The VTC strands were placed on both surface layers using three differences cases. The first case had 20% by weight of VTC strands placed on the top and bottom surface layers (10% each surface). The second case had 40% by weight of VTC strands placed on the top and bottom surface layers. In the third case, instead of weight percent, there was 50% by volume of VTC strands for the two face layers (about 75% by weight of VTC). The first two cases mimic an experimental study to Rathi (2009). The third case, which is discussed first, replaces all surface strands with VTC strands to compare to the previous results on commercial OSB.

3.6.4.1 50% VTC by Volume

In this case, 50% VTC strands by volume were placed on the two face layers (25% on each face). The VTC strands in this case had the same thickness and length as the normal strands. Compared to the case in Figure 3.10, only the face (surface) layer strands were changed to VTC strands. The core remained as unmodified strands. Figure 3.15 gives the MPM calculations for axial modulus for these OSB panels as a function of mat compaction and glue-line stiffness. Like OSB with unmodified strands, the modulus decreased as the interfacial compliance ($1/D_t$) increased. The MOE values are much higher compared to the results without VTC (see Figure 3.10) because the surface strands provide most of the stiffness and these strands were replaced by VTC strands. A panel with 1% coverage would have an axial modulus about 25% lower than one with 100% coverage. The result shows the influence of interfacial stiffness was higher when using VTC strands. Comparing the case without VTC (Figure 3.10) to this case (Figure 3.15), there is at least 93% increase in modulus at the same levels of compaction. In Figure 3.15, all the data in this plot are obtained from average of at least five runs. The error bars on one curve show the standard deviation of the results. There was little change in standard deviation for different values of $1/D_t$.

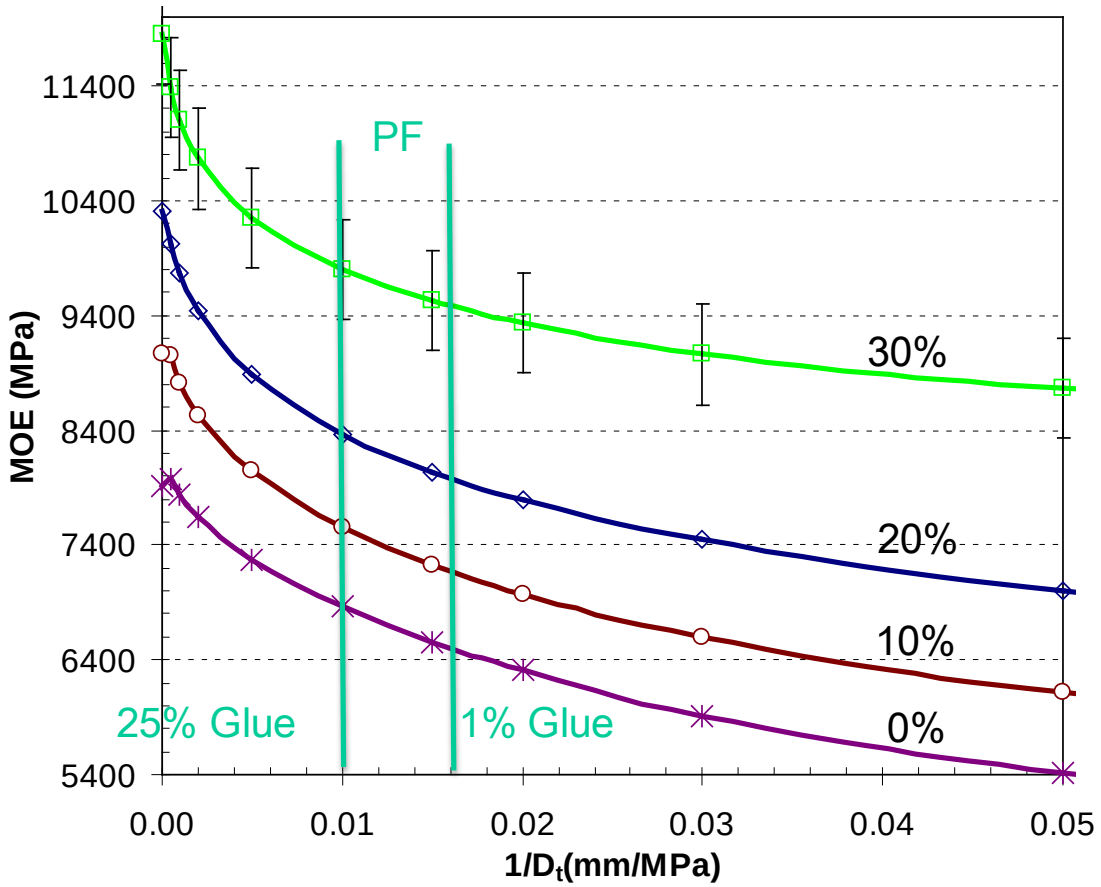

Figure 3.15. Simulation results of MOE versus $1/D_t$ at different levels of compaction with all VTC strands on face layers.

3.6.4.2 20% and 40% of VTC by Weight

To test the role VTC strand at constant weight fraction, experiments by Rathi (2009) and simulations were run with 20% and 40% by weight VTC strands on the surface. These results were compared to control specimens with 20% and 40%, by weight normal strands on the surface. Instead of 90 degree orientation to the surface layers, all these specimens had a randomly oriented core layer. Although full simulation with random core requires 3D analysis, here we did approximate 2D analysis by rotation of strand properties according to random angle for all core strands. The mechanical properties for different grain angles were rotated around z and calculated accordingly using stiffness matrix rotation (see appendix for details on rotation matrix). Using the

transformed stiffness matrix, a new approximate orthotropic material was obtained. The core strands had correct axial moduli, but the 2D calculations cannot account for tension-shear coupling because that is a 3D effect.

The modeling of OSB with VTC strands followed the methods described earlier for normal strands. In this case, the geometry (length and width) of the normal strands was the same as before but the length of the VTC strands were 125 mm (25 mm shorter than the normal strands). Real VTC strands were thicker but here we had to use same thickness to align with the grid. To account for thickness, strand length and weight for the 20% weight VTC, there were two VTC strand layers (one on each surface) out of 21 strands total (19 normal strand layers were randomly oriented). This structure was as close as possible to 20% by weight we could achieve as the grid and it gave 19.7% VTC by weight. For 40% weight VTC strands, the closest possible structure has two VTC strands on each surface out of 18 total strands (14 normal strands randomly for core layer). The actual MPM simulation of VTC weight was 40.0% for the 40% VTC case.

To get the base line for comparison between VTC and normal strands, we also did simulations for the control cases for 20% and 40% of weight of normal strands on the surface. In the 20% control case, there were total of 4 normal strands on the surfaces (2 for each surface) out of 20 total strands (16 normal strands randomly for core layer). In the 40% control case, there were 8 normal strands on the surfaces (4 for each surface) out of 20 total strands (12 normal strands randomly for core layers). Both these cases exactly matched to target weight fraction.

There was at least a 7 % increase in MOE for 20% weight VTC compared to the control. This result is shown in Figure 3.16. This trend is the same for the case of 40% weight VTC on the surface layers, but there was a 28% increase in MOE for 40% weight VTC compared to no VTC control (see Figure 3.17). The values of MOE decreased as $1/D_t$ increased and the difference got slightly smaller at high $1/D_t$.

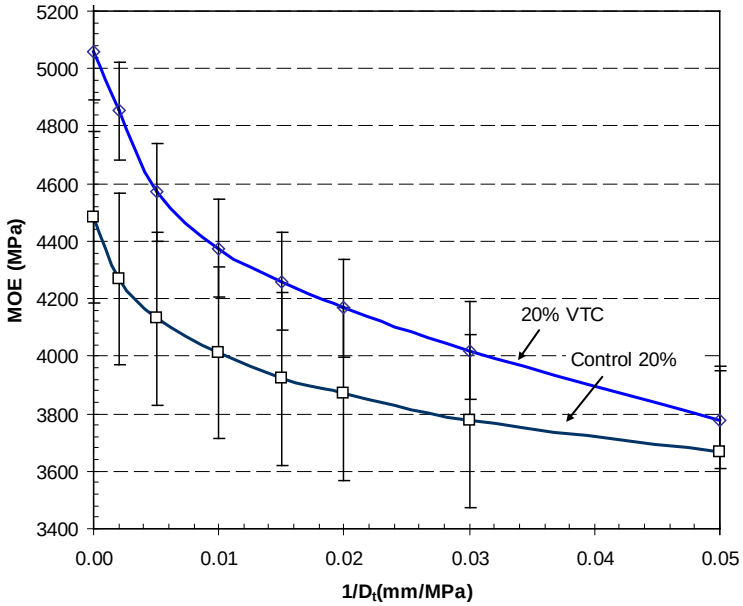

Figure 3.16. Comparison of MPM calculation of modulus of OSB panel with 20% by weight of VTC on the surface to the control at 20% compaction.

Table 3.2 has a summary of simulated moduli results of Figure 3.16 and Figure 3.17 for different values of adhesive coverage compared to experimental results (Rathi 2009). The experimental results were in bending but the MPM simulations were in tension. Bending MOE is expected to be much higher in MOE than tension MOE (as it is) but relative changes provide some indication of the validity of the model results. In studies by Rathi (2009), the 20% control is 11.6GPa +/- 1.57GPa for MOE and for 20% VTC, MOE is 12.4 +/-1.57 for a 6.9% increase. In the case of 40% control, MOE is 12.9 +/-1.72 GPa and for 40% VTC, MOE is 16.1+/-2.47 GPa for a 24.8% increase. The results in our studies vary with the interfacial stiffness. In our simulation of 20% VTC, there is 7.9% increase in MOE for 1% adhesive coverage and 9.1% increase in MOE for 25% adhesive coverage levels and 12.9% increase in MOE for 100% glue. For 40% VTC, there is 23 % increase in MOE for 1% adhesive coverage, 27% increase in MOE for 25% adhesive coverage levels, and 31% increase in MOE for 100% adhesive coverage. In average there is 9% increase in MOE for 20% VTC and 26% increase for 40% VTC which is close to experiment values of Rathi (2009).

In Figure 3.16 and Figure 3.17 the error bars represent one standard deviation for 10 simulation runs. In Figure 3.17 the error bars of the 20% control and 20% VTC overlapped. This is because some simulated mats had no continuous layer of VTC for the case of 20% VTC. Furthermore, the strand length of VTC was 25 mm shorter than the normal strands in the core (see chapter 6 for effect of strand length on mechanical properties). However, for 40% VTC, there was always continuous path through the VTC strands on the surface layers, which resulted in more increase in MOE. As showed in Figure 3.17, there was no overlap of error bars between control and VTC panels.

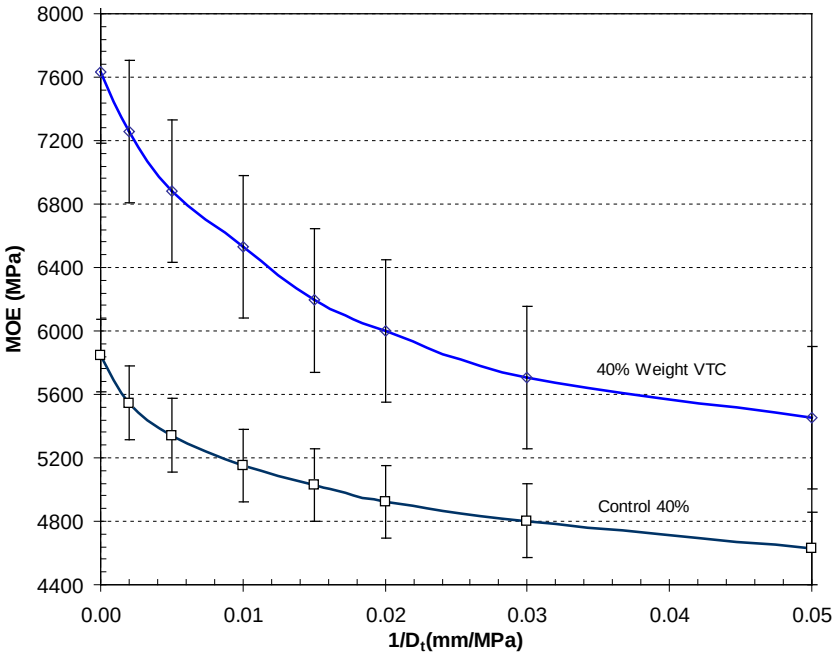

Figure 3.17. Comparison of MPM calculation of modulus of OSB panel with 40% by weight of VTC on the surface to the control at 20% compaction.

The 40% control MOE is higher than the 20% control MOE (see Figure 3.16 and Figure 3.17). This is because the 40% control had more strands aligned parallel to the axis of analysis. The 40% control is even higher than the case with 50% surface strands in Figure 3.10. This is because the core strands in the 40% control was randomly oriented, thus contributed more to MOE than the 90 degree core plies in Figure 3.10.

Table 3.2: Experiment (in bending) and MPM simulation (in tension) moduli for control and different weight VTC addition.

	MOE (GPa)				
Surface Content	**Control**	**Stdv**	**VTC**	**Stdv**	**% Increase[1]**
20% Expt	11.6	1.57	12.4	1.57	6.9%
20%, 1% PF MPM	3.9	0.71	4.2	0.81	7.9%
20%, 25% PF MPM	4.0	0.71	4.4	0.78	9.1%
20%, 100% PF MPM	4.5	0.68	5.1	0.84	12.9%
40% Expt	12.9	1.72	16.1	2.47	24.8%
40%, 1% PF MPM	5.0	0.41	6.2	1.06	23%
40%, 25% PF MPM	5.2	0.40	6.5	1.07	27%
40%, 100% PF MPM	5.8	0.41	7.6	1.13	31%

1) Increase for VTC compared to control.

3.7 Modeling

3.7.1 Homogenized Model

A homogenized rule of mixtures (HROM) was developed to help interpret results at different levels of compaction. The OSB composites are approximately a three-layer structure. For each layer, the axial modulus was replaced by an homogenized modulus by considering the volume fraction of gaps within each layer. The moduli of the surface (E_s) and core (E_c) layers were thus replaced by:

$$E_S \approx E_L \frac{\langle L \rangle}{\langle L \rangle + \langle G_L \rangle} \qquad \text{and} \qquad E_C \approx E_R \frac{\langle W \rangle}{\langle W \rangle + \langle G_W \rangle} \qquad (3.7)$$

where E_L and E_R are the longitudinal and radial modulus of the strands, $\langle L \rangle$ and $\langle W \rangle$ are the average length and width of the strands, and $\langle G_L \rangle$ and $\langle G_W \rangle$ are the average gaps between strands in the surface and core layers (see "homogenize" step in Figure 3.18). Next, it was assumed that these moduli increased uniformly due to compaction to $E_S/(1-C)$ and $E_C/(1-C)$, where C is the fraction compaction (see last step in Figure 3.18).

Finally, a simple rule of mixtures was used to find effective tensile modulus of compacted OSB as:

$$E^* = \frac{E_S V_S + E_C V_C}{1 - C} \tag{3.8}$$

where V_S and V_C are the volume fractions of surface and core strands. In the case of OSB in sections 3.4.1 and 3.4.5.1, both V_S and V_C are equal to 1/2. For 20% and 40% OSB in section 3.4.5.2 V_S and V_C are different and E_R is replaced by random modulus of the core.

For OSL structures there is no core layer, so V_C = 0 and V_S = 1 and equation 3.8 becomes:

$$E^*_{OSL} = \frac{E_S}{1 - C} \tag{3.9}$$

These equations predict a linear relation between OSB modulus, OSL modulus and 1/(1-C) where C is fraction of compaction. However, this HROM is not able to model interface effects, account for undulating strands or account for non uniform compaction in the layers. These parameters do not enter this simple model. Deviations from this model may be explained by one or more of these effects.

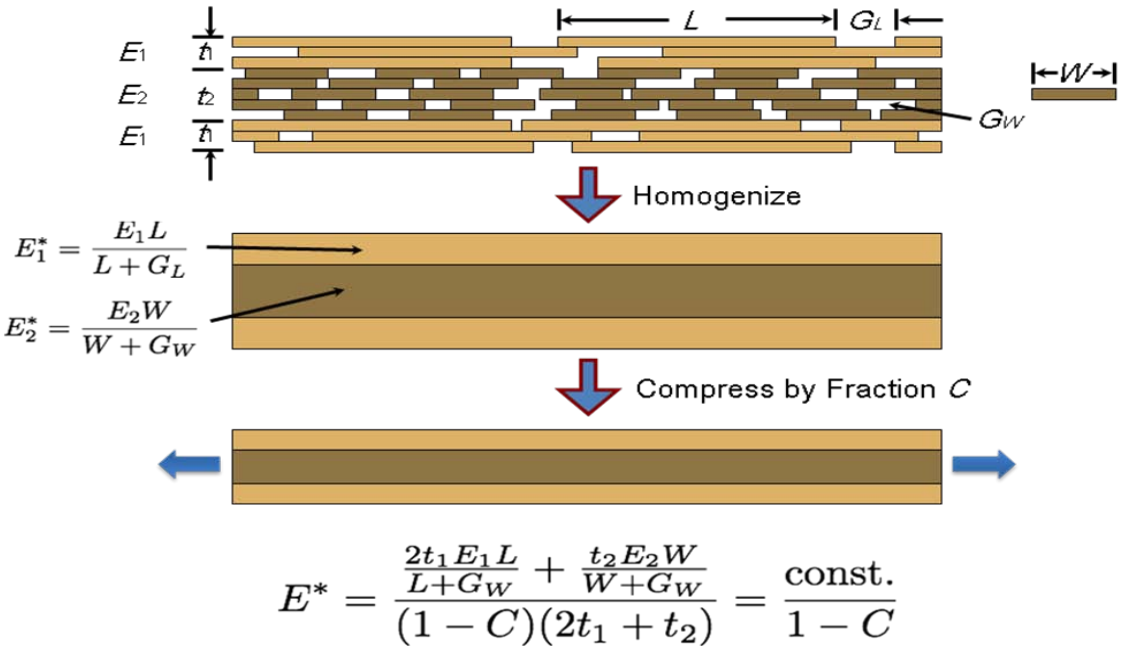

Figure 3.18. Homogenized lamination theory (rule of mixture).

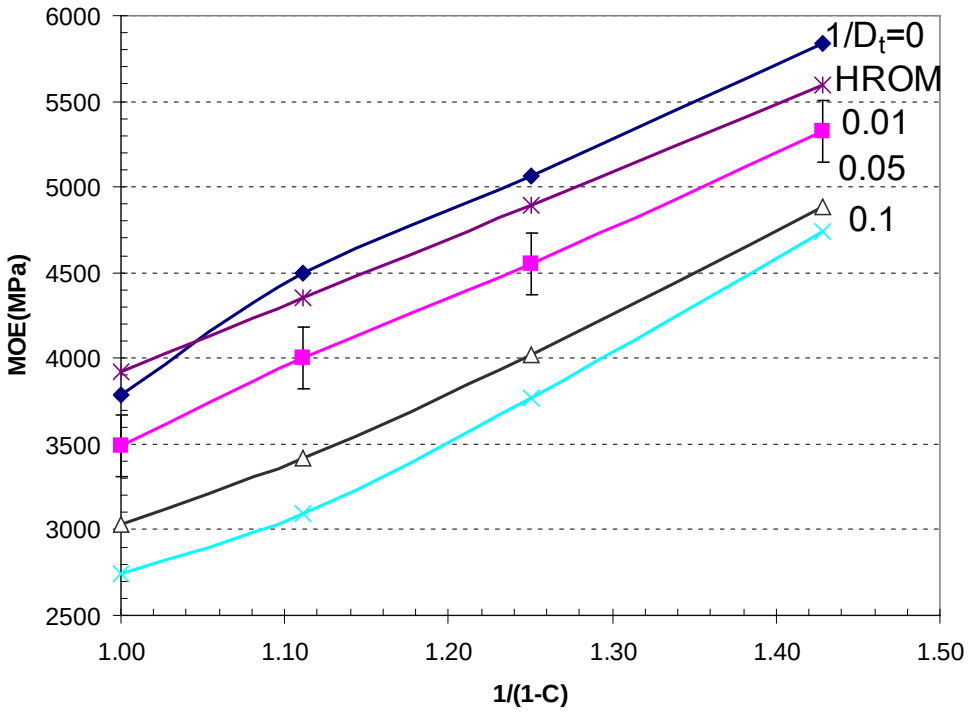

Figure 3.19. MPM calculation of MOE of OSB panel with unmodified strand as a function of 1/(1-*C*) and the glue line stiffness.

Figures 3.19 and 3.20 re-plot the results of Figures 3.10 and 3.15 as a function of 1/(1-*C*) along with the homogenized model in equation 3.8. The different curves are various values of $1/D_t$. The numerical results are approximately linear but deviate from the simplistic modeling. The results for a perfect interface ($1/D_t=0$) are close to the linear model, but simulation results with unmodified strands are nonlinear and higher than the model, while simulations results with VTC strand are nonlinear and lower than the model. These shifts are a consequence of non-uniform compression in the layers. In real OSB panels, the surfaces are denser than the core. This effect is reproduced in the simulations where the surface layers are compacted more than the core layers (see chapter 6). Since the surface layers contribute most of the modulus, extra compaction in these layers leads to higher modulus than expected from the simplistic uniform compaction model (see Figure 3.19). When using VTC strands, however, the surface layers are already densified and thus densify less than the core layers during mat

compaction. Thus the numerical results are lower than the uniform compaction model (see Figure 3.20).

Another difference between simulations and the simplistic model is that the model cannot predict the influence of interfacial stiffness (D_t). The model consists of three parallel layers loaded by uniform deflection to find the modulus. Since no shear will develop during axial loading, there will be no interfacial slippage. A numerical model is needed to study the effect of $1/D_t$ on MOE. The results in Figure 3.19 and 3.20 show a drop in MOE as $1/D_t$ increases. All curves are approximately linear in 1/(1-C) but do show same non linearities.

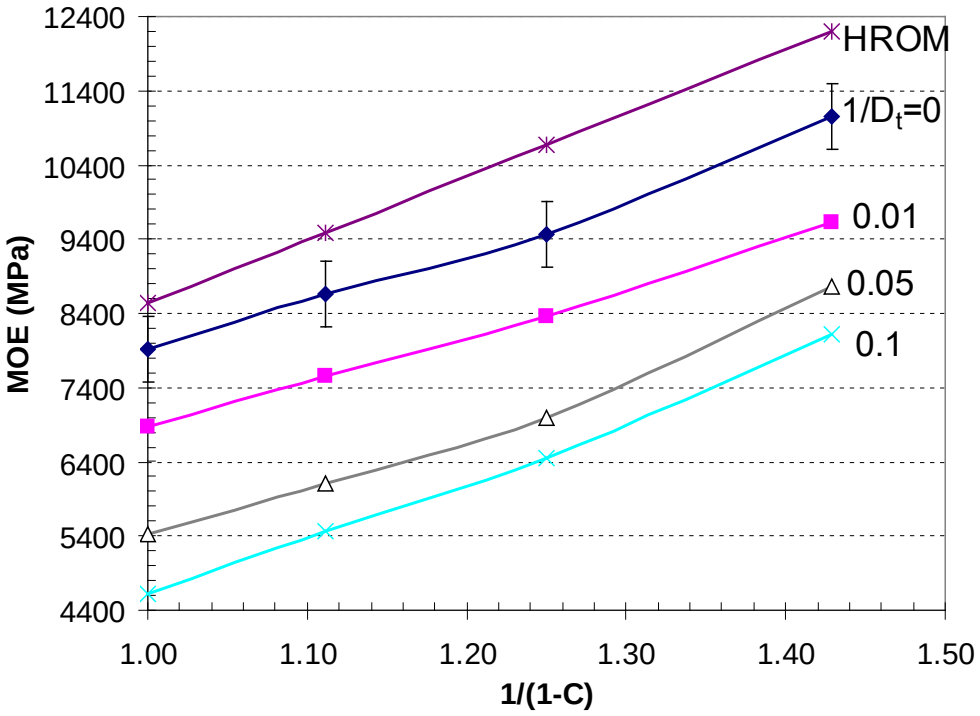

Figure 3.20. MPM calculation of MOE of OSB panel with modified VTC strands as a function of 1/(1-*C*) and the glue line stiffness.

To calculate effective modulus using HROM for samples with a random core, the modulus for the randomly orientation (core) strands was set to 2422MPa, which is much higher than the transverse (radial or tangential) elastic modulus of wood. This value was obtained from laminated plate theory for an isotropic laminate of wood strands. Figure

3.21 and 3.22 compare simulated results to HROM as function of 1(1-C) for two values of $1/D_t$ for 20% control and 20% VTC surfaces. For control specimens, V_S=0.2 and V_C =0.8; for 20% VTC specimens V_S=2/21 (0.095) and V_C =19/21 (0.905). For commercial OSB, the 20% control is higher than HROM, due to input, more compaction on the surface. The 20% VTC, however is also higher the HROM, while before VTC results were lower. This difference is likely due to the random core. Since that modulus is higher, it contributes more to MOE and the model using a single E_C might not be as accurate compared to simulations where simulated strands had a distribution in moduli.

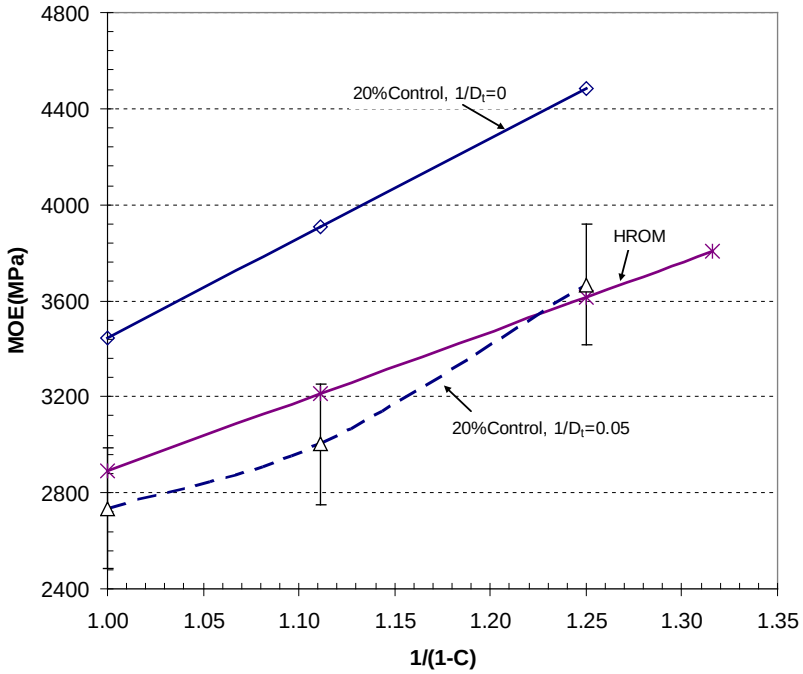

Figure 3.21. MPM calculation of MOE of OSB panel for control 20% modified strand as a function of 1/(1-*C*) and the glue line stiffness.

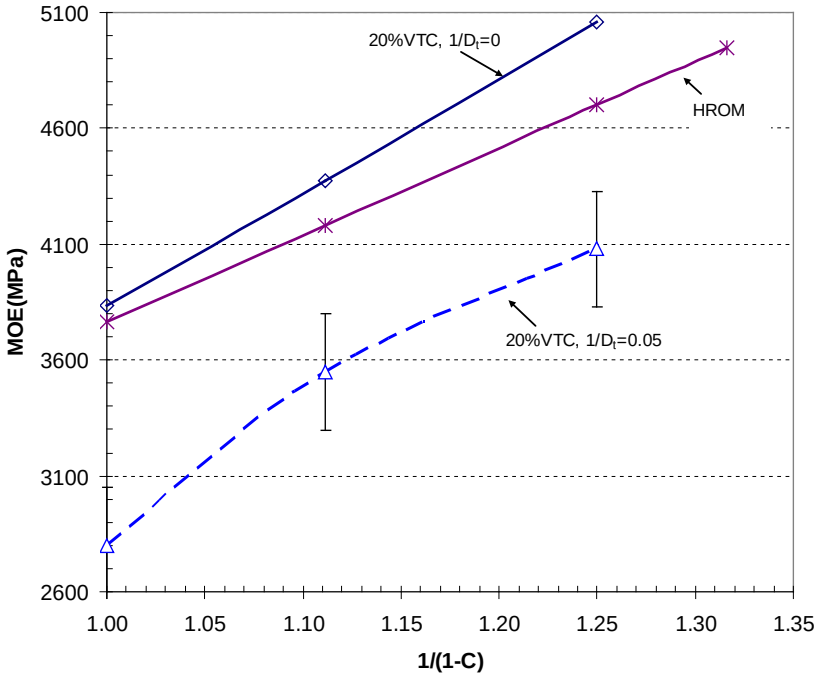

Figure 3.22. MPM calculation of MOE of OSB panel for 20% modified strand as a function of 1/(1-*C*) and the glue line stiffness.

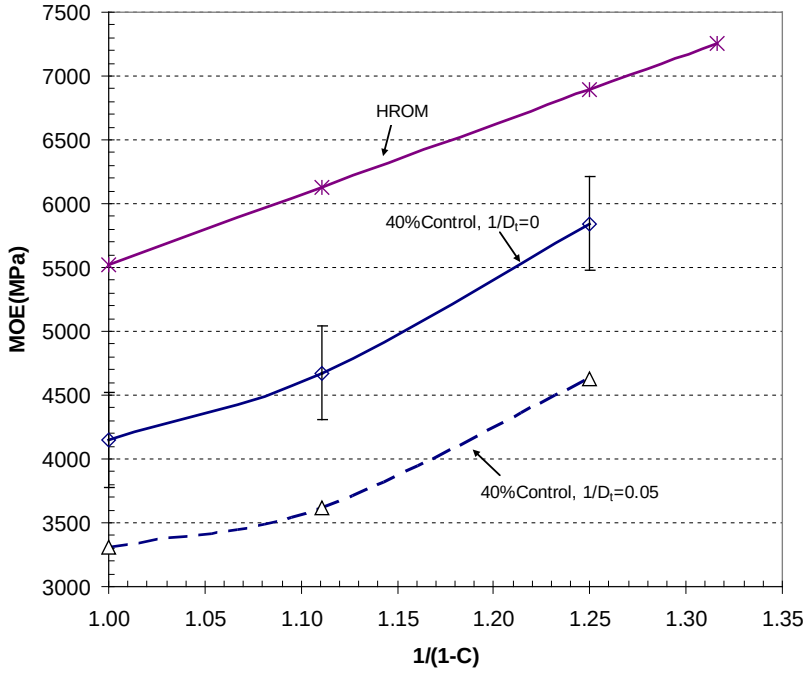

Figure 3.23. MPM calculation of MOE of OSB panel for 40% control modified strand as a function of 1/(1-*C*) and the glue line stiffness.

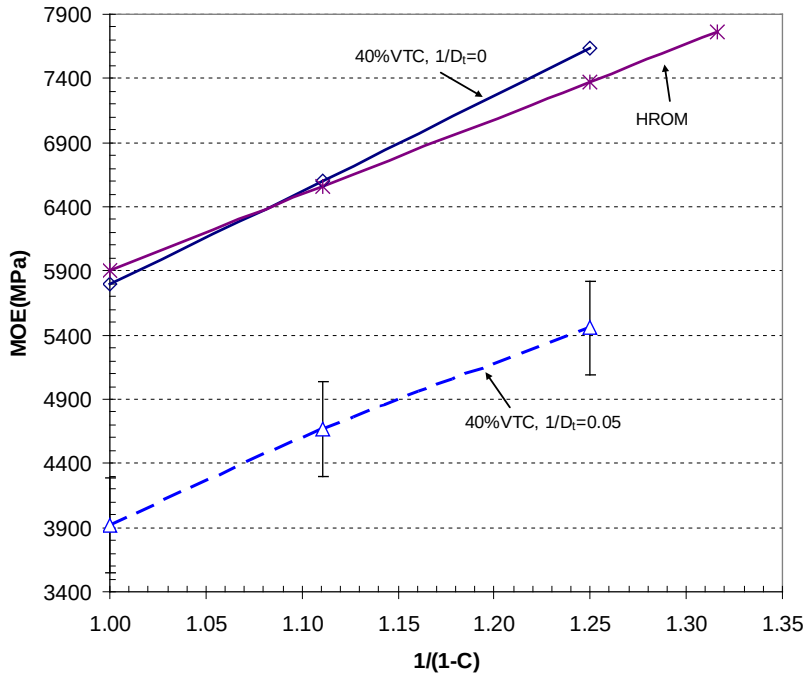

Figure 3.24. MPM calculation of MOE of OSB panel for 40% modified strand as a function of 1/(1-*C*) and the glue line stiffness.

Similarly, Figure 3.23 and Figure 3.24 plot the results for simulated values of moduli as a function for 1/(1-C) along with the homogenized model for two different values of $1/D_t$ for 40% control VTC. For control specimens of 40%, V_S = 0.4 and V_C = 0.6; for 40% VTC specimens V_S = 4/18 (0.222) and V_C = 14/18 (0.778). The same trend is obtained as in the case of 20% control and 20% VTC as the level of compaction increased. However, in this case, the moduli in HROM is higher than numerical data for all cases. Unlike in the case of 20% by weight which was very sensitive to the initial structure and the location of where VTC strand is added, in this case (40% VTC), there is a continuous layers of VTC on the surface. As a result, the modulus is less likely to vary due to random structure when mats are formed. Furthermore, in this case there are fewer randomly oriented strands in the core compared to the case of 20 percent VTC. Thus the core in 40% VTC contributed less to the calculated stiffness in HROM.

3.8 Summary and Conclusions

This study has demonstrated that MPM can handle large-scale, morphology-based models of real wood-based composites including glue-line effects, strand undulation and compaction effects. It is easy to generate a wood-strand composite structure based on strand length, strand gap, and strand thickness. Once the random structure of a wood-strand composite is completed, it can then be compressed. The structure can also include elastic-plastic and work hardening properties during compaction and yielding. Once the structure is compressed, tension load can be applied to find MOE.

The mechanical properties increased as compaction levels increased. Furthermore, the numerical calculation can also test mechanical properties as a function of interfacial properties. A glue-line interfacial property affects the mechanical properties of the entire composite. As the interfacial properties increased (from discrete droplets [1%] to continuous bond line [100%]), the mechanical properties of strand-based composites increased. There are higher mechanical properties when using VTC strands in the surface layers with 20% and 40% weight fractions. There is more increase in mechanical properties when using VTC strands in all the surface layers. In order to compare the stiffness values to the experiment data, more work is needed to determine the amount of compaction in the OSB panels.

Appendices

Appendix 3.1: Generalize interpolation material point method (GIMP) derivation

In solid mechanics, the deformation of a continuous solid body under load is governed by conservation of mass and momentum. The virtual work or power can be formulated as a general equation of momentum as:

$$\int_V \rho\vec{b}\cdot\delta\vec{u}dV + \int_{S_T}\vec{T}\cdot\delta\vec{u}dS + \sum_P \vec{F}_P\cdot\delta\vec{u} = \int_V \rho\vec{a}\cdot\delta\vec{u}dV + \int_V \sigma:\nabla\delta\vec{u}dV \qquad (3.10)$$

where σ, ε and u are stress, strain and displacement. $\vec{b}$ and $\vec{F}_P$ are specific body force (such as gravity) or point loads. $\vec{T}$ is surface traction, $\vec{a}$ is acceleration, $\delta\vec{u}$ is virtual displacement and ρ is density. In MPM, this equation is solved in a Lagrangian frame on a grid.

A Lagrangian formulation means that the acceleration does not contain the convection term which can cause significant numerical errors in purely Eulerian approaches. During this Lagrangian phase of the calculation, each element is assumed to deform in the flow of the material so that points in the interior of the element move in proportion to the motion of the nodes. That is, given the velocity at the nodes determined from Eq. (3.10), the element shapes are updated by moving them in this single-valued, continuous velocity field. Similarly, the velocity and position of a material point is updated by mapping the nodal accelerations and velocities to the material point positions.

In this method, the mesh does not conform to the boundary of the object being modeled. Instead, a computational domain is constructed in a convenient manner to cover the potential domain for the boundary-value problem being solved. Then the object is defined by a collection of material points. As material points move, they transport material properties assigned to them without error. In MPM, the material points carry enough information to reconstruct the solution; therefore one can choose whether to continue the calculation in the Lagrangian frame or map information from the material points to another grid. This feature avoids mesh tangling which can occur in a purely Lagrangian calculations under large strains, and allows one to choose the grid for

computational convenience. In practice, the deformed grid is discarded after each time step and the next time step begins with a new, regular mesh.

In MPM the body is divided into particles of mass m_p representing small volume m_p/ρ_p. In generalized interpolation material point method (GIMP), any function can be expanded in a particle basis using:

$$f(x) = \sum_P f_P \chi_P(\vec{x}) \qquad (3.11a)$$

where f_ρ is property or volume function f on the particle and $\chi_P(\vec{x})$ is a particle shape function. For example, density is expanded as

$$\rho(x) = \sum_P \frac{m_P}{V_P} \chi_P(\vec{x}) \qquad (3.11b)$$

$$f_P = \rho_P = \frac{m_P}{V_P} \qquad (3.11c)$$

The particle characteristic (shape function) is required to integrate to particle values in the initial configuration and undeformed state as $\int_V \chi_P(\vec{x}) dV = V_P$. The force that is distributed over the volume of particles P is then:

$$\rho\vec{a} = \sum_P \frac{m_P}{V_P} \frac{d\vec{v}_P}{dt} \chi_P(\vec{x}) = \sum_P \frac{\dot{\vec{P}}_P}{V_P} \chi_P(\vec{x}) \qquad (3.11d)$$

where $\dot{\vec{P}}_P$ is momentum of particle *p* and equal to mass times velocity. The internal stress is then: $\sigma = \sum_P \sigma_P \chi_P(\vec{x})$, $\chi_P \neq 0$ only near particles *p*, otherwise it is 0. At the start of the time step, all the information on the particles is projected to the grid (such as mass, velocity, internal force, etc.). Equation (3.10) with particle expansions becomes

$$\sum_P \int_V \frac{m_P}{V_P} \chi_P(\vec{x}) \vec{b} \cdot \delta\vec{u} dV + \int_S \vec{T} \cdot \delta\vec{u} dS + \sum_P \vec{F}_P \cdot \delta\vec{u} =$$
$$\sum_P \int_V \frac{\dot{\rho}_P}{V_P} \chi_P(\vec{x}) \cdot \delta\vec{u} dV + \sum_P \int_V \tilde{\tilde{\sigma}}_P \chi_P(\vec{x}) : \nabla\delta\vec{u} dV$$

The next step is to distribute $\vec{F}_P$ over one particle according to the $\chi_P(\vec{x})$ function.

$$\vec{F}_P = \frac{\vec{F}_P}{V_P}\int \chi_P(\vec{x})dV \tag{3.12a}$$

The sum of the forces that are distributed over entire particle *p* is then:

$$\sum_P \vec{F}_P \cdot d\vec{u} = \sum_P \frac{\vec{F}_P}{V_P}\int_V \chi_P(\vec{x}) \cdot \delta\vec{u} \tag{3.12b}$$

The next step is to expand the virtual displacement in terms of grid based shape functions

$$\delta\vec{u} = \sum_i \delta\vec{u}_i N_i(\vec{x}) \tag{3.13a}$$

leading to

$$\sum_i \sum_P \int_V \frac{m_P}{V_P}\chi(\vec{x})\vec{b} \cdot d\vec{u}_i N_i(\vec{x}) = \sum_i \sum_P m_P \vec{b}\left(\frac{1}{V_P}\chi(x)N_i(\vec{x})\right) \cdot \delta\vec{u}_i \tag{3.13b}$$

$$\int_S \vec{T} \cdot \delta\vec{u}dS = \sum_i \int_S \vec{T}N_i(x) \cdot \delta\vec{u}dS \tag{3.13c}$$

$$\sum_P \vec{F}_P \cdot d\vec{u} = \sum_i \sum_P F_P\left(\frac{1}{V_P}\int_V \psi_P(x)N_i(x)dv\right) \cdot \delta\vec{u}_i \tag{3.13d}$$

$$\sum_P \int_V \frac{\dot{\rho}_P}{V_P}\chi_P(\vec{x}) \cdot \delta\vec{u}dV = \sum_i \sum_P \dot{\rho}_P\left(\frac{1}{V_P}\int \chi(x)N_i(x)dv\right) \cdot d\vec{u}_i \tag{3.13e}$$

$$\sum_P \int_V \tilde{\tilde{\sigma}}_P \chi_P(\vec{x}) : \nabla\delta\vec{u}dV = \sum_i \sum_P \left(V_P \tilde{\tilde{\sigma}}_P \frac{1}{V_P}\int \chi_P(x)\nabla N_i(x)dV\right) \cdot \delta\vec{u}_i \tag{3.13f}$$

By theorem of virtual work, $\delta\vec{u}_i$ is arbitrary. Thus equating all terms in summations over i gives:

$$\sum_P \dot{\rho}_P \bar{S}_{iP} = \sum_P V_P \tilde{\tilde{\sigma}}_P \cdot \nabla\bar{S}_{iP} + \sum_P m_P \vec{b}\bar{S}_{iP} + \int_S \vec{T}N_i(x)dS + \sum_P F_P \bar{S}_{iP} \tag{3.14a}$$

which can be written as:

$$\dot{P}_i = f_i^{\text{int}} + f_i^b + f_i^s + f_i^{ext} \tag{3.14b}$$

$$\dot{P}_i = \sum \rho_P \bar{S}_{iP} \tag{3.14c}$$

$$\text{where } f_i^{\text{int}} = -\sum_P V_P \tilde{\tilde{\sigma}}_P \nabla\bar{S}_{iP} = -\sum_P m_P \tilde{\tilde{\sigma}}_P^{(s)} \cdot \bar{\nabla}\bar{S}_{iP} \tag{3.14d}$$

$$f_i^b = -\sum_P m_P \vec{b} \bar{S}_{iP} \tag{3.14e}$$

$$f_i^S = \int_S \vec{T} N_i(x) dx = \int_S \rho \tilde{\tilde{\sigma}}^{(S)} \cdot \hat{n} N_i(x) dx \tag{3.14f}$$

$$\text{and } f_i^{ext} = \sum_P F_P \bar{S}_{iP} \tag{3.14g}$$

Here the rate change of momentum on the grid is denoted by $\dot{P}_i$, the "internal force" due to stress is denoted by f_i^{int}, and the forces due to body forces, surface tractions and external load are denoted by f_i^b, f_i^s, f_i^{ext} respectively.

The functions $\bar{S}_{iP}$ and $\bar{\nabla}\bar{S}_{iP}$ are particle shape, and gradient shape functions respectively. Note that both are implicit functions of grid vertex position.

$$\bar{S}_{iP} = \frac{1}{V_P} \int_S \chi_P(\vec{x}) N_i(\vec{x}) dV \tag{3.14h}$$

The interpolation function is formed by gradients of shape functions by:

$$\bar{\nabla}\bar{S}_{iP} = \frac{1}{V_P} \int_S \chi_P(\vec{x}) \nabla N_i(\vec{x}) dV \tag{3.14i}$$

When MPM was first introduced, $\chi_P(\vec{x})$ was effectively equal to $V_P \delta(\vec{x})$ where $\delta(\vec{x})$ is Dirac delta function. This assumption leads to

$$\bar{S}_{iP} = N_i(\vec{x}_P) \text{ and } \bar{\nabla}\bar{S}_{iP} = \nabla N_i(\vec{x}_p)$$

This approached could result in numerical noise when particles cross element boundaries in the grid. The noise was caused by discontinuities in $\nabla N_i(\vec{x}_p)$. The problem is greatly minimized in GIMP by choosing $\chi_P(\vec{x})$=1 over a volume V_P around the particle and 0 elsewhere. The resulting $\bar{\nabla}\bar{S}_{iP}$, unlike $\nabla N_i(\vec{x}_p)$, has no discontinuities.

Appendix 3.2: Calculated mechanical property from elastic modulus

The experiments on double lap shear specimens gave results for interfacial properties (D_t). For modeling of OSB, we also needed orthotropic material properties of the strands. The strands, however, are too small for most tests except axial modulus. For modeling we estimated all other properties by ratios from measured modulus derived from solid wood properties. The results are described here.

The hybrid polar strands (OSB type) were cut into small sizes to prepare for the double lap shear tests. MOE was measured for each individual strand. During DLS tests, over 1000 individual strands were loaded in tension. The results for these MOE parallel to grain were E_L=9936±935MPa.

Hybrid poplar is a combination of Western and Eastern poplar. From the Wood Handbook (Table 4-1), solid yellow poplar properties have the ratios E_T/E_L = 0.043, E_R/E_L = 0.092, G_{LR}/E_L = 0.075, G_{LT}/E_L = 0.069, G_{RT}/E_L = 0.011. We therefore estimated hybrid poplar strand properties using E_T = 9936*0.043 ± 935*0.043 = 427 ± 40MPa, E_R = 9936*0.092 ± 935*0.092 = 914 ± 86MPa, G_{LR} = 9936*0.075 ± 935*0.075 = 745 ± 6Mpa, G_{LT} = 9936*0.069 ± 935*0.069 = 686 ± 64MPa, G_{RT} = 9936*0.011 ± 935*0.011 = 109 ± 10MPa. These results are shown in Table 2.1 as well. The Poisson's ratio were assumed to be the same as yellow poplar or μ_{LR}=0.31, μ_{LT}=0.39, μ_{RT}=0.70, μ_{TR}=0.33, μ_{RL}=0.03, and μ_{TL}=0.02.

For orthotropic materials, such as wood, Poisson's ratios are different in each direction (x, y, and z). Additionally, pairs of Poison ratios are related by:

$$\frac{\mu_{ij}}{E_i} = \frac{\mu_{ji}}{Ej},\ i \neq j \quad \text{i, j =L, R, T} \tag{3.15}$$

after substituting L,R, and T we have: $\frac{\mu_{LR}}{E_L} = \frac{\mu_{RL}}{E_R}$, $\frac{\mu_{LT}}{E_L} = \frac{\mu_{TL}}{E_T}$, $\frac{\mu_{RT}}{E_R} = \frac{\mu_{TR}}{E_T}$. The results of Poisson's ratio are calculated using the relationship from equation 3.15. The Poisson's ratio of hybrid poplar is show in Table 3.3. μ_{TR} is the highest and μ_{TL} is the lowest. From Table 3.3, the trend of elastic properties values from the experiment is consistent with others such as the example from Katz et al (2008) that E_L is the largest and E_T is the

smallest. The COV (coefficient of variation) and standard deviation were similar (but better) to Wood Handbook (United State Department of Agriculture, 1999). The literature value of COV is 25 for tension parallel to grain, whereas we obtained 16 for our results.

Similarly, the mechanical properties of VTC strands were calculated from strand MOE and the results are given in Table 2.2. Due to densification effects in VTC, all stiffnesses were higher. The Poisson ratios were assumed to be the same.

Table 3.3: Elastic properties of yellow poplar and hybrid poplar.

Properties in GPa	E_1	E_2	E_3	G_{13}	G_{12}	G_{23}	μ_{13}	μ_{12}	μ_{32}	μ_{23}	μ_{31}	μ_{21}	**Reference**
	E_L	E_T	E_R	G_{LR}	G_{LT}	G_{LR}	μ_{LR}	μ_{LT}	μ_{RT}	μ_{TR}	μ_{RL}	μ_{TL}	
Yellow poplar	10.890	0.470	1.000	0.820	0.750	0.120	0.310	0.390	0.700	0.330	0.030	0.020	Katz et al, 2008
	Psi												
Hybrid poplar strand	9.936	0.427	0.914	0.745	0.686	0.109	0.326	0.465	0.706	0.327	0.029	0.017	Our Experiment
Stdev	1.608	0.069	0.148	0.121	0.111	0.018	0.053	0.075	0.114	0.053	0.005	0.003	
COV	16%	16%	16%	16%	16%	16%	16%	16%	16%	16%	16%	16%	

	μ_{LR}/E_L	μ_{RL}/E_R	μ_{LT}/E_L	μ_{TL}/E_T	μ_{RT}/E_R	μ_{TR}/E_T
Yellow poplar	0.031	0.033	0.039	0.047	0.766	0.772

Table 3.4: Mechanical properties for unmodified and VTC strands.

Property in MPa	Unmodified Strands	VTC Strand
E_L	9936	24311
E_R	914	2153
E_T	427	1005
G_{RL}	745	1616
G_{TL}	686	1486
G_{RT}	109	235
μ_{RL}	0.028	0.028
μ_{TL}	0.017	0.017
μ_{TR}	0.33	0.33
σ_L(yield)	∞	∞
σ_R(yield)	5	5
σ_T(yield)	5	5
σ_{RT}(yield)	2.5	10

Appendix 3.3: Calculated mechanical property for random core

According to general mechanics, rotation of the compliance tensor, about z axis gives xy-plane properties:

$$\frac{1}{E_{xx}} = \frac{1}{E^S_{xx}}\cos^4\theta + (\frac{-2\upsilon^s_{xy}}{E^S_{xx}} + \frac{1}{G^S_{xz}})\sin^2\theta\cos^2\theta + \frac{1}{E^S_{zz}}\sin^4\theta \quad (3.15)$$

$$\upsilon_{xy} = \upsilon_{TL}\cos^2\theta + \upsilon_{TR}\sin^2\theta \quad (3.17)$$

$$G_{xy} = G_{TL}\cos^2\theta + G_{TR}\sin^2\theta \quad (3.18)$$

$$E_{yy} = E_R \quad (3.19)$$

The resulting compliance matrix in 2D that was used is

$$\left(\left(\frac{1}{E_{xx}}, \frac{-\upsilon_{xy}}{E_{xx}}, 0\right); \left(\frac{-\upsilon_{xy}}{E_{xx}}, \frac{1}{E_{xx}}, 0\right); \left(0, 0, \frac{1}{G_{xy}}\right)\right) \quad (3.20)$$

Full rotation would have nonzero S_{13}, S_{23}, S_{31}, S_{32} but that can‘t be in a 2D plane strain material.

We also have to rotate yield stresses. Figure 3.1A shows the assumed represented yield $\sigma_{x\tau}$, $\sigma_{y\tau}$, $\sigma_{z\tau}$, and $\sigma_{x\tau}$ as function of rotational angle.

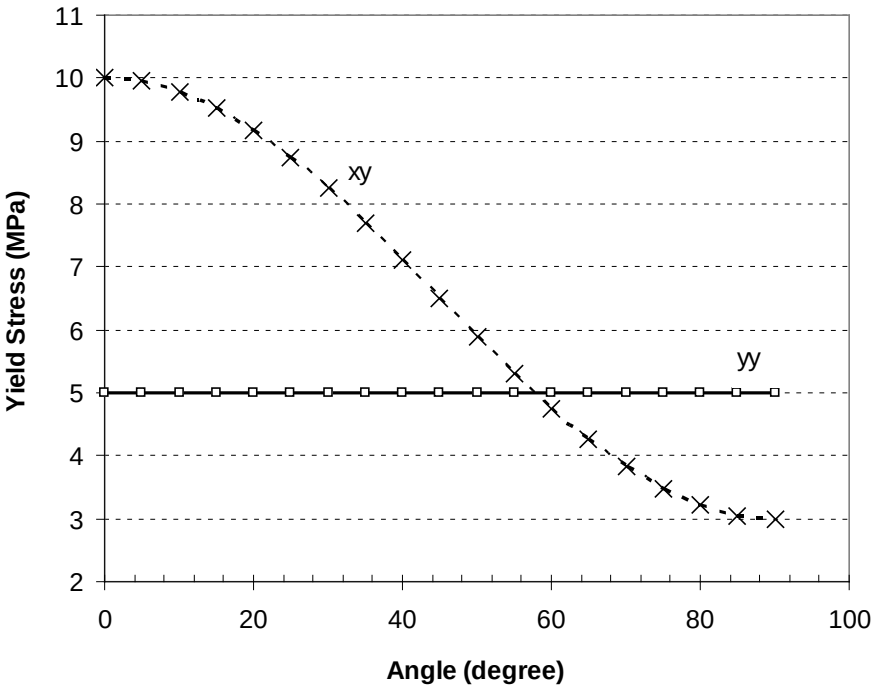

Figure 3.1A. Yield stress as function of rotational angle for σ_{yy} and σ_{xy}.

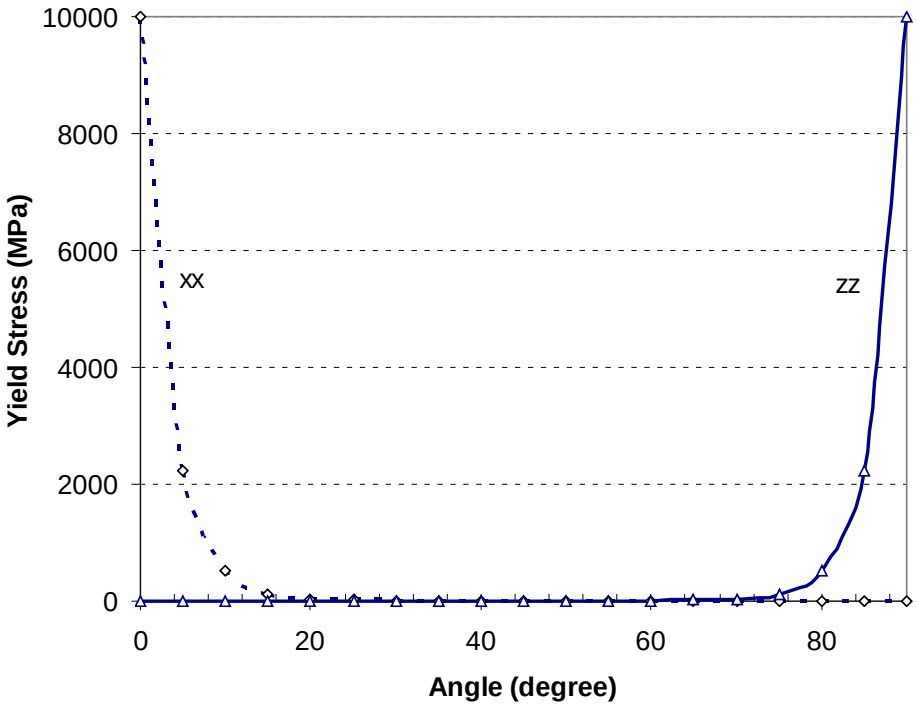

Figure 3.2A. Yield stress as function of rotational angle for σ_{xx} and σ_{zz}.

Appendix 3.4: Compaction Movies

Movie 1: Compaction of OSB structure.

Movie 2: Compaction of OSB with no gaps (plywood structure).

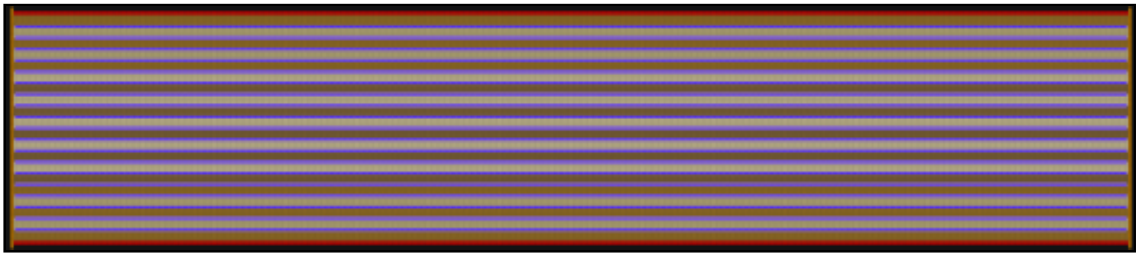

References

Atluri, S. N., and S. P. Shen (2002) The meshless local Petrov-Galerkin (MLPG) method. Tech. Science Press, Forsyth, GA.

Bai X, Lee AWC, Thompson LL, Kosowsky DV (1999) Finite element analysis of Moso bamboo-reinforced southern pine OSB composite beams. Wood Fiber Sci 31(4):403–415.

Belytschko, T., Y. Y. Lu, and L. Gu (1994) Element-free Galerkin methods. Int. J. Num. Meth. Eng. 37:229–256.

Bodig, J. and B. A. Jayne (1982) Mechanics of wood and wood composites. Van Nostrand Reinhold Company, New York, NY.

Brydon, A., S. Bardenhagen, E. A. Miller, and G. T. Seidler (2005) Simulation of the densification of real open cell foam microstructures. J. Mech. Phys. Solids. 53:2638–2660.

Budman, H., G. Painter and M. Pritzker (2006) Prediction of oriented strand board properties from mat formation and compression operating conditions. Part 2: MOE prediction and process optimization, Wood Sci Technol (2006) 40: 291–307.

Ellis, S., and P. Steiner (2002) The behavior of five wood species in compression. IAWA Journal, Vol 23(2): 201-211.

Saliklis E. P. and Mussen A. L (2000) Investigating the buckling behavior of OSB panels. Wood Fiber Sci 32(3):259–268.

Guan, Z., E. Zhu, P. Rodd and D. Pope (2005) A constitutive model for OSB and its application in finite element analysis. Holz Roh-Werkstoff 63:87–93

Smith, I., E. Landis, and E. Gong (2002) Fracture and fatigue in wood. John Wiley & Sons, Ltd., New York, NY.

Sulsky, D, Z. Chen, and H. L. Schreyer (1994) A particle method for history-dependent materials. Comput. Methods Appl. Mech. Engrg., 118:179–186.

Sulsky, D., S.-J. Zhou, and H. L. Schreyer (1995) Application of a particle-in-cell method to solid mechanics. Comput. Phys. Commun., 87:236–252.

Cha, J. K., and Pearson, R. G. (1994) ‘‘Stress analysis and prediction in 3-layer laminated veneer lumber: Response to crack and grain angle.’’ Wood and Fiber Sci., 26(1), 97–106.

Clouston L. Peggi and Frank Lam (2001) Computational Modeling of Strand-Based Wood Composites. J. Engrg. Mech., Volume 127, Issue 8, pp. 844-851.

Ionescu I., Weiss J., Guilkey J., Cole M., Kirby R., and Berzins M. (2006) "Ballistic Injury Simulation Using The Material Point Method", in *Medicine Meets Virtual Reality 14. eds, J. Westwood et al., IOS Press, 2006, pp.* 228-233.

Ishikawa T. and T.-W. Chou (1983) Nonlinear Behavior of Woven Fabric Composites. *Journal of Composite Materials*, Vol. 17, No. 5, 399-413.

Lee, J.N. and Q.Wu (2003) Continuum Modeling of engineering constants of oriented strandboard. Wood & Fiber Sci. 35(1):24-41.

Morris V, Gustafsson PJ, Serrano E (1995) The shear strength of light-weight beams with and without a hole- a preliminary study. Workshop on mechanical properties of panel products, March, 1995, Watford, UK

Nairn, J. A. (2003A) Material point method calculations with explicit cracks. Computer Modeling Eng. Sci. 4:649–664.

Nairn, J.A. (2005B) Generalized Shear-lag Analysis Including Imperfect Interfaces, Advanced Composite Letters, 13, 263-274.

Nairn, J.A. (2006C) Numerical simulation of transverse compression and densification in wood, Wood and Fiber Science, 38(4), pp576-591.

Nairn, J.A. (2006D) On the calculation of energy release rates for cracked laminates with residual stresses, International Journal of Fracture, 139, pp 267-293.

Nairn, J.A. (2007E) Numerical implementation of imperfect interface. Computational Materials Science, 40:525-536.

Nairn, J.A. (2007F) A numerical study of the stransverse modulus of wood as a function of grain orientation and properties. Holzforschung, 61:406-413.

Gibson, L. J., and M. F. Ashy (1997) Cellular solids: Structure and properties. Cambridge University Press, UK.

Guilkey. J. E., T. Harmon, B. Kashiwa, A. Xia, and P. A. Mcmurtry (2003) An Eulerian-Lagrangian approach for large deformation fluid-structure interaction problems, part 1: algorithm development. Proc. 2nd Inter. Conf. on Fluid-Structure Interactions. June 24–26, 2003, Cadiz, Spain.

Guo, Y., and J. A. Nairn (2004) Calculation of J-Integral and stress intensity factors using the material point method. Computer Modeling Eng. Sci. 6:295–308.

Hashin, Z. (1991) Composite Materials with Viscoelastic Interphase: Creep and Relaxation, Mechanics of Materials, 11(2): 135–148.

Hill, J. R. (1948) A theory of the yielding and plastic flow of anisotropic metals. Proc. Roy. Soc. London, 193:281-297.

Kamke, F. A. and V. Rathi (2009) Modified hybrid poplar for structural composies. In: Proc. 4th European Conference on Wood Modification, Stockholm, Sweden, April 27-29, pp 397-400.

Kamke, F. A. and L. Rautkari (2009) Modified wood veneer for structural application. In: Proc. Fourth International Symposium on Venner Processing and Products, May 24-27, Espoo, Finland. pp 2007-212.

Kutnar A., Kamke, F. A. and M. Sernek (2008) The mechanical properties of densitfied VTC wood relevant for structural composites. Hoz als Roh-Werkst. 66(6): 439-446.

Sulsky, D., H. Schreyer, K. Peterson, R. Kwok, and M. Coon (2007) Using the material point method to model sea ice dynamics, J. Geophys. Res., 112.??

Harlow, F.H. (1964) "The Particle-in-Cell Computing Method for Fluid Dynamics in Fundamental Methods in Hydrodynamics," Experimental Arithmetic, High-Speed Computations and Mathematics, Edited by B. Alder, S. Fernbach and M. Rotenberg, Academic Press, pp. 319 345.

Bardenhagen, S.G., and E. M. Kober (2004) The generalized interpolation material point method. Computer Modeling Eng. & Scie. B: 477-496.

Bardenhagen, S.G., J. U. Brackbill, and D. Sulsky (2000) The material point method for granular materials. Computer Methods Appl. Mech. Eng. 187:529–541.

Bogren, K., Gamstedt, K., Neagu, C., Akerholm, M. and Lindstrom, M. (2008) Dynamic-Mechanical Properties of Wood–Fiber Reinforced Polylactide: Experimental haracterization and Micromechanical Modeling, J. of Thermoplastic Composite Materials, Vol. 19: 613-636.

Rathi V (2009) Bending property enhancement of wood strand composite using viscoelastic thermal compression *MS Thesis* Oregon State University, Corvallis, OR.

Simo J C and T J R Hughes (1997) Computational Inelasticity. Sprinerger-Verlag, New York.

Steiner P and Simon E (2002) The behavior of five wood species in compression. IAWA Journal, Vol. 23 (2), pp201-211.

Sulsky D, Chen Z and Schreyer H L 1994 *Comput. Methods Appl. Mech. Eng.* **118** 179-86.

Sulsky D, Zhou S J and Schreyer H L (1995) Application of a particle-in-cell method to solid mechanics. *Comput. Phys. Commun* **87** 236-52.

Sulsky D and Schreyer H K (1996) Axisymmetric form of the material point method with applications to upsetting and Taylor impact problems. *Comput. Methods Appl. Mech. Eng.* **139** 409-29.

U.S. Department of Agriculture (1987) Wood Handbook. Agriculture Handbook No. 72, Superintendent of Documents, Washington D.C. 466pp.

Xue, L., Borogin, O., Smith, G., and Nairn, J. (2006) Michomechanics simulation of the viscoelastic properties of highly filled composites by the material point method (MPM), Modeling Simul. Matter. Sci. Eng. 14, pp 703-720.

Yadama, V., M. P. Wolcott, and L. Smith (2005) Elastic properties of wood-strand composites with undulating strands. Composites: Part A 37: 385-392.

Zhou S (1998) The numerical prediction of material failure based on the material point method *PhD Thesis* University of Mexico, Albuquerque, NM.

CHAPTER 4 – EFFECT OF ELASTIC PROPERTIES IN BENDING OF WOOD-STRAND COMPOSITES WITH GLUE-LINE INTERFACE AND STRANDS UNDULATING

Abstract

The mechanical properties of wood-based composites depend on interfacial properties, phases properties (wood species), and the adhesive used. Due to anisotropic properties of wood-strands, the mechanical properties of the final product depend on the load path that is applied. Therefore, understanding mechanical properties of wood-based composites under both tensile and bending loading can help to tailor panels with optimal load carrying ability.

The previous study in chapter 3 covered the tensile mechanical properties of wood-strand composites. In this study, an emerging numerical model called the material point method (MPM) was used to study the mechanical properties of wood-strand composites (OSB, OSL, plywood and LVL) that are loaded in bending as a function of bondline interfacial stiffness, strand properties (normal and modified strands), and strand undulation at different levels of compaction. Results show that interfacial properties are even more important for composites loaded in bending than in tension because the properties are affected even in the absence of strand undulation. Modified stands with higher mechanical properties improve the mechanical properties of the panel and especially enhance bending properties when used on the surface of the OSB.

4.1 Introduction

To meet high demand, maintain mechanical strength and stiffness, lower cost, and tailor wood-based composites in structural applications, manufacturers need to look at all aspects from material costs, logging, processing, and factors that contribute toward the mechanical properties. Due to the anisotropic properties and the complexity of the anatomy of wood, the mechanical properties of wood differ in different loading directions. Furthermore, the structural details of wood composites may make their mechanical properties such as modulus of elasticity (MOE) and modulus of rupture

(MOR) different for loads applied in tension or bending. These properties will depend on arrangement of strands or plies in the composite.

Most wood-based composites that are used in structural applications are loaded under bending, such as the web in I-beams, floor beams, ceiling rafters in houses, and many more. It is also notable that many of the published values for mechanical properties of wood and wood-based composites are obtained by experiments in bending. Therefore, studying (experiment or numerical modeling) the effect of glue-line and strand undulation on mechanical properties of wood-strand composites that are loaded in bending is of much interest for structural applications.

Lee and Wu (2003) presented a continuum model capable of predicting the MOE of OSB based on laminate plate theory and the mechanical properties of the flakes and the resin. However, their model predictions exhibited some discrepancies from experimental results. In another study, Lee (2003) studied an optimization of OSB manufacturing that focused on the continuous pressing process, but did not consider the mechanical strength of the panel.

Much of the literature concerning OSB strength is focused on experiments to develop an empirical relationship between processing parameters and MOR. Barnes (2000) developed an empirical model that included wood content, resin content, in-plane orientation, strand length, strand thickness, fines content, and flake orientation. Budman et al. (2006) used the output from a mat formation simulation and a compression model (Painter et al. 2005), which considered the flake size from the mat formation model and the vertical density profile (VDP) from the compression model, to calculate total volume of each layer after compression. They used this structure in conjunction with laminate theory with input empirical parameters in a Hankinson-type equation (Bodig and Jayne 1982, Wood Hand book 1998) to find flake modulus versus angle to predict the effective tensile and bending modulus of the entire panel. The model was able to predict VDP well but was not able to incorporate the resin content or realistic morphology (strand undulating effects). Although the vertical density profile (VDP) has a significant effect on the MOE (Kelly 1977), it has been ignored in most models.

In this study, we looked at the effect of the glue-line (varying the amount of resin) on the bending mechanical properties of wood-strand composites. The predictions of bending mechanical properties were done as a function of compaction and glue-line stiffness in the OSB composites. The effect of using improved wood strands (modified strands) in the face layers was also studied.

4.2 MPM Simulations

The MPM simulations for wood-strand composites such as OSB, OSL, and LVL in bending used the same approach as in the previous study (Chapter 3). The OSB mats consisted of three different layers as in the previous study (Chapter 3). The compaction of OSB and OSL were done by the same MPM methods (Chapter 3). The mats were formed with random distributions in dimensions and gaps. The face strand length was 150 mm with standard deviation of 20 mm. The face strand gap was 15 mm with standard deviation of 4.95 mm. The strand width in the core layers was 25 mm with standard deviation of 3 mm. The strand width gap (side-to-side space) was 10 mm with standard deviation of 1 mm). After the mats were compacted, the archived compacted results were used as an input for new MPM bending simulations.

In all calculations, each wood strand was uniform in thickness with rectangular geometry. Longitudinal stiffness properties were measured experimentally while other elastic constants were calculated from elastic constant ratios (Bodig and Jayne 1982; Gibson and Ashy 1997) (see chapter 3 for details).

The bending properties were studied using the simulation of a cantilever beam. The specimen was held at one end and the other end was loaded by a bending moment. The moment was applied by equal but opposite transverse loads on the top and bottom surfaces of the beam (see Figure 4.1). Figure 4.2 shows a cantilever beam model before and after loading. For total load P, the applied moment is M=Ph, where h is thickness of the simulated beam.

In bending, the load is carried mainly by the top and bottom surfaces (Wood Design Book 2006). The middle portion of the beam is mainly acting as a transfer medium for the load to move to the surface. Thus, in order to achieve the highest

stiffness in bending in such designs, the higher stiffness material is often placed on the outer most surfaces.

The MOE in bending was found by an energy analysis. For a cantilever beam that is fixed on one end and loaded by a moment *M* on the other end (see Figure 4.1). The total energy is area under the moment-curvature plot times length:

$$U = \frac{1}{2} M \kappa L = \frac{M^2 L}{2 E_b^* I} \tag{4.1}$$

where $M = Ph$, κ is the curvature, E_b^* is effective bending modulus, I =Bh^3/12. B is depth, h is height of the beam and L is the length. The total energy is then:

$$U = \frac{12 P^2 h^2 L}{2 E_b^* B h^3} = \frac{6 P^2 L}{E_b^* A} \tag{4.2}$$

where A= Bh is cross sectional area of the beam. Finally, the effective MOE in bending is

$$E_b^* = \frac{6 P^2 L}{UA} \tag{4.3}$$

Given MPM results for *U*, specimen dimensions and load, E_b^* can be found.

Figure 4.1. Schematic of cantilever beam for bending test of MPM calculation.

4.2.1. Validation of Model (Sensitivity Study)

The energy method was used to calculate the effective modulus of elasticity for all the calculations loaded in bending. To validate the energy approach, an isotropic material was tested. The beam was 100 mm long, 10 mm high and with *E* =2500MPa, Poisson ratio = 0.33, density (rho) = 1g/cm^3. Due to the isotropic material properties that were used, the results of the calculation of bending MOE by the energy method (equation 4.3) should be same as the input tensile E= 2500 MPa. Figure 4.3 shows energy

calculated by Eq (4.3) as function of time for beam loaded up to 2N with loading rate of 20 N/msec and then held. The curve shows an initial peak due to dynamic effects, but eventually settles down to E close to the expected result (E=2500 MPa).

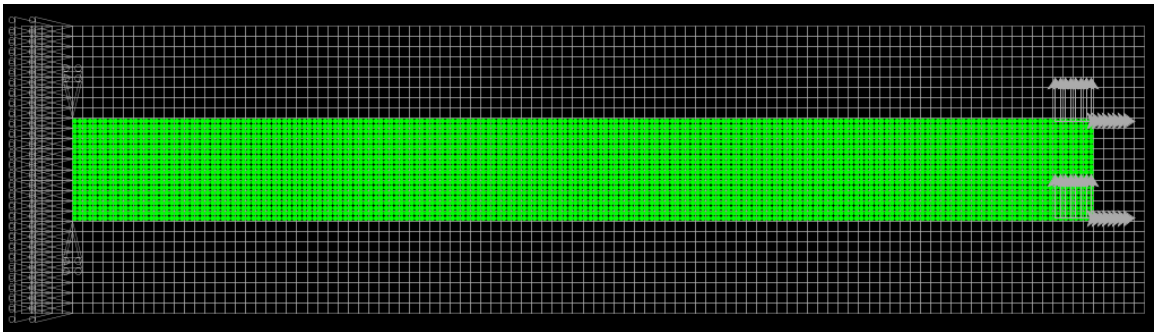

a) Unload

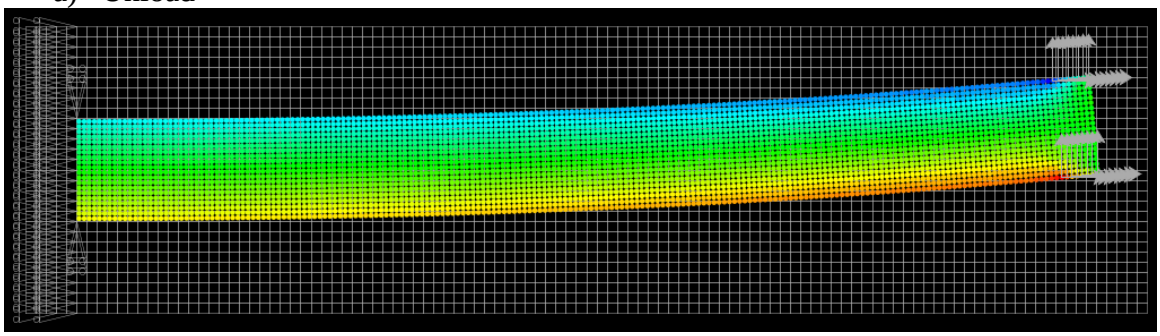

b) Load

Figure 4.2. Setting up of cantilever beam for bending test of isotropic properties in MPM; a) no load, b) loaded.

As discussed earlier (in chapter 3), there are dynamic effects in MPM that need to be understood to find MOE. Figure 4.3 shows the dynamic effects on the elastic properties in MPM simulations with damping and without damping. When there was no damping, there were oscillations of MOE over time but less oscillation occurred when damping was used. At early time, there was a large oscillation of MOE but the results stabilize at long time. To calculate MOE the strain energy was recorded (here there was no interface energy). All calculations needed to wait for E_b^* to reach a constant value. In Figure 4.3, the results of a simulated homogenous beam are plotted over loading time. In the early time there are dynamic effect but after 25-30 msec, the effective modulus levels off and is close to input MOE (2500 MPa).

To compare dynamic effects to expected time scales, the natural frequency of the cantilever beam was calculated (Goldsmith, 1962):

$$f = \frac{x^2}{2\pi L^2}\sqrt{\frac{EI}{\rho A}} \qquad (4.4)$$

where E is modulus, L is length (100mm), ρ is density (1g/cm^3=1000kg/m^3), A is the cross sectional area, and I is moment of inertia and equal to Bh^2/12, B is width and h is height. The oscillation time for a complete cycle is $\tau = \frac{1}{f}$. The term x, which corresponds to vibration modes, is found from solution to cos(x)cosh (x) =-1. The first root, for the fundamental frequency, is x =1.985. Plugging in all values, the oscillation time for one cycle is 3.9 msec. As seen in Figure 4.3, 3.9 msec is close to the simulated oscillation period. It takes 5 to 10 times this period for MOE to level off. Adding damping helps the process. Note that the time to get MOE in bending (about 20 msec) is about 1000 times longer than the time to get MOE in tension (0.021 msec, see chapter 3). The bending calculations thus took much longer.

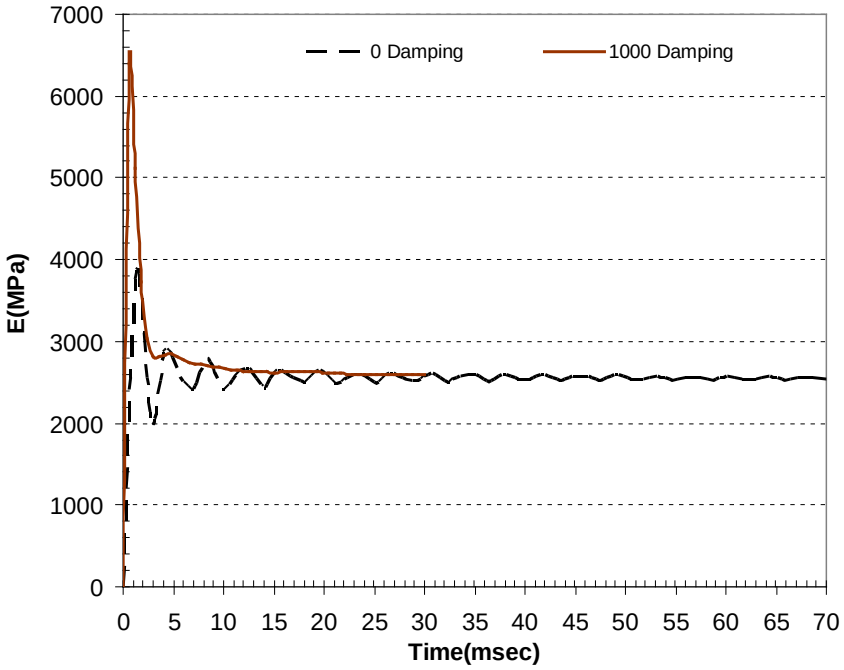

Figure 4.3. Dynamic effects on modulus.

4.3 Results and Discussion

4.3.1 Numerical Modeling of OSB in Bending Mode

All calculations were done using two-dimensional, explicit MPM code (Nairn 2005a). To insure the simulation was in the elastic region, the plastic energy was tracked and the deformation was limited to small strains. The small deformation was done by applying a small load; the specimen was loaded with constant P = 2 N (or moment, M = $2h_0$[1-C] N*mm because h=[1-C]*h_0, where C is level of compaction and h_0=16mm).

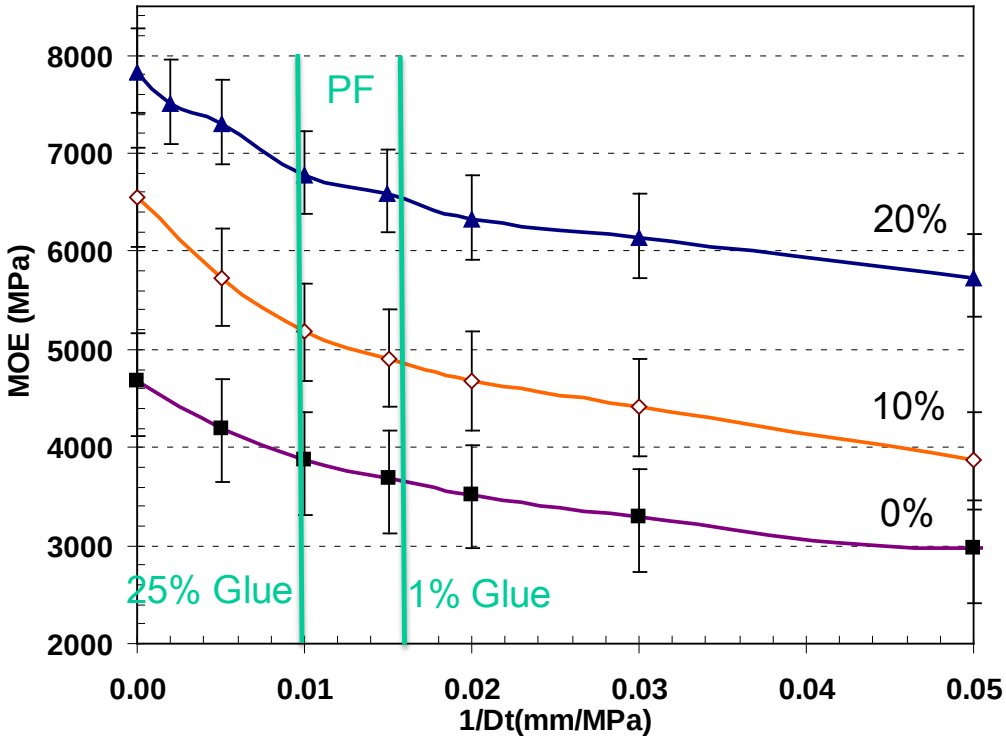

Figure 4.4. Numerical and analytical results of bending MOE versus 1/Dt for different level of compaction with gaps (strand length 150 mm, gap 30 mm).

Figure 4.4 shows bending MOE versus $1/D_t$ for different levels of compaction. The MOE in this calculation is much higher than the MOE calculation in tension in the previous study (Nairn and Le 2009, chapter 3). This is because the surface strands with the higher stiffness carried more load then when loaded in tension.

Figure 4.4 also shows an overlay of different adhesive coverages (in previous study chapter 2) at 1% and 25%; 100% close to $1/D_t = 0$. At 20% compaction, there was about 3.5% increased in MOE for the case of 1% to 25% adhesive coverage, there was about 19% increase in MOE from 1% to 100% adhesive coverage, and there was 15% increase in MOE from 25% to 100% adhesive coverage. From the previous study in tension (chapter 3) at 20% compaction, there was about 3.3% increase in MOE for the case of 1% to 25% adhesive coverage, there was about 15% increase in MOE from 1% to 100% adhesive coverage, and there was about 11% increase in MOE from 25% to 100% adhesive coverage. As these results show, there was slightly more increase of MOE in bending than MOE in tension.

Comparing the MOE in bending and MOE in tension (from chapter 3), on average, MOE in bending is roughly about 1.35 to 1.4 times higher than MOE in tension. The difference is a consequence of the structure of the OSB panels with the stiffness of the strands larger on the surfaces.

4.3.2 Plywood (*OSB with No Gaps*)

To look at strand undulation effects, an OSB simulation with no gaps was done. The analysis specimen was 100 mm in length and had an initial height of 16 mm. The specimen was held on one end and the other end was under shear loads on the top and bottom in the opposite direction to develop upward curvature. Figure 4.5 shows MOE as the function of $1/D_t$ for different levels of compaction. MOE increased as the level of compaction increased. Unlike in tension, where the no-gaps results showed no effect of glue line stiffness (chapter 3), in bending, the MOE still depends on the glue line stiffness.

Figure 4.5 also shows an overlay of different adhesive coverages (from previous study chapter 2) at 1% and 25% (100% is close to $1/D_t = 0$). At 40% compaction, there was about 4.5% increase in MOE from 1% adhesive coverage to 25% adhesive coverage, there was about 10% increase in MOE from 1% adhesive coverage to 100% adhesive coverage and there was about 5.7% increase from 25% adhesive coverage to 100% adhesive coverage. There was similar behavior in MOE at others levels of compaction.

These results show that, good glue-line interfaces are important for composites that are loaded in bending even in the absence of strand undulation.

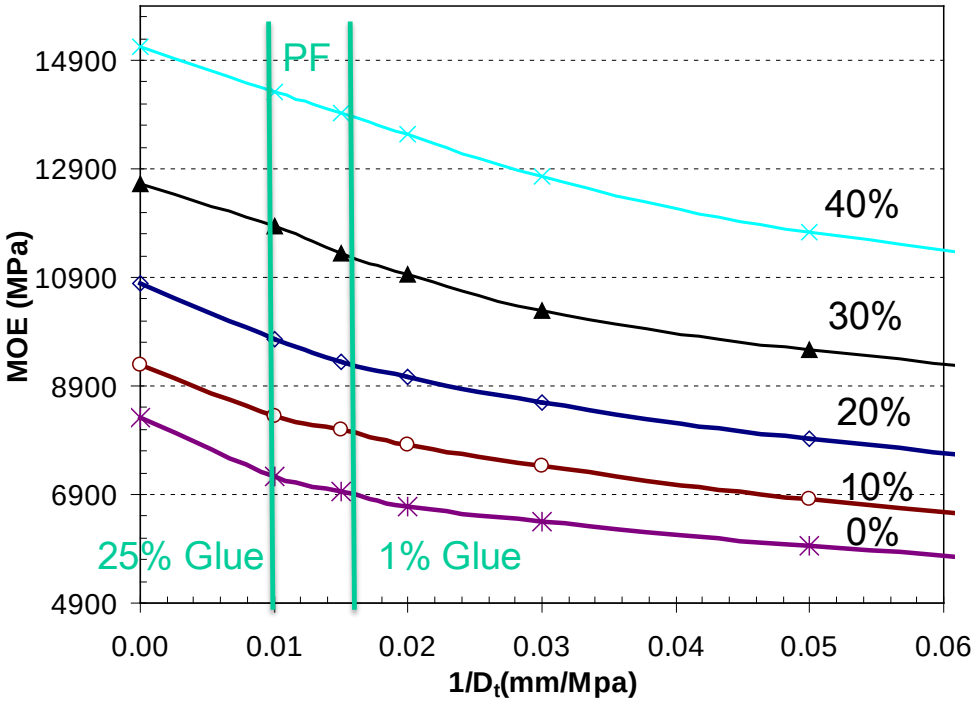

Figure 4.5. Numerical and analytical results of bending MOE versus 1/Dt for different level of compaction with no gaps.

4.3.3 Numerical Modeling of OSB with Surface Strands Loaded in Bending

To test the role of VTC strands at constant weight fraction, experiments (Rathi 2009) and simulations were run with 20% or 40%, by weight VTC strands on the surface. These results were compared to control specimens with 20% or 40%, by weight normal strands on the surface. The same structures and configurations as in the previous study (chapter section 3.6.4.2) were used. Instead of loading the structures in tension, however, this study loaded them in bending.

Figure 4.6 shows results of 20% VTC versus 20% control as a function of interfacial stiffness. There was at least 7% increase in MOE in 20% VTC compared to the control at same $1/D_t$. This trend is the same for the case of 40% VTC but was larger –

there was a 33% increase in MOE for 40% VTC compared to 40% control (see Figure 4.7). At 40% VTC, there was a continuous path of VTC strands on the surface, therefore, they had a larger increase in MOE. There was an effect of interface on the MOE and the effect was larger in the 40% VTC than in the 20% VTC (e.g. the decrease from 100% to 1% glue was larger for 40% VTC).

Table 4.1 has a summary of simulated moduli results of Figure 4.6 and Figure 4.7 along with the experimental data from Rathi (2009). The absolute values between simulations and experiments do not agree. For comparison, we looked instead at relative moduli between VTC specimens and controls. From experimental results, for OSB panels with 20% VTC, there are was a 6.9% increase in MOE; for OSB panel with 40% VTC addition, there was a 25% increase in MOE (Rathi 2009). The increase in MOE from simulations varied with different values of D_t. From the results of Table 4.1 there was 13.6% increase in MOE for 1% adhesive coverage, a 16.1% increase in MOE for 25% adhesive coverage levels, and a 26.1% increase in MOE for 100% glue. For the case of 40% VTC, there was a 30% increase in MOE for 1% adhesive coverage, a 32% increase in MOE for 25% adhesive coverage and a 37% increase in MOE for 100% adhesive coverage. The simulations show the potential for increase in MOE is higher when the glue is better. Thus optimal VTC panels should optimize the glue to get the most benefit from the VTC strands.

In average there was 18.6% increase in MOE for 20% VTC and a 32% increase for 40% VTC which are larger than experimental values of Rathi (2009) but trend in the same direction. The simulation of 40% VTC gave closer results to experiment than the 20% VTC. This may be because the 20% VTC had only one layer of VTC strands on each surface so the panel may be more influenced by the initial configuration. However, in the 40% VTC addition, there were more VTC strands on the surface, and less dependence on randomly selected structures.

In Figure 4.6 and 4.7 the error bars represent one standard deviation in the mean of at least 5 different runs. In Figure 4.6 the error bars for the 20% control and 20% VTC overlapped. This may be because of the lack of continuous layers of VTC for the 20% VTC. However, for 40% VTC, there was a continuous layer of VTC strands on the

surface layers. At shown in Figure 4.7, there is no overlap of error bars. The error bar (one standard deviation) for the simulated results are listed in Table 4.1 as well. There were larger standard deviations for the case of 20% VTC than for 40% VTC addition. The error bars for 20% and 40% control were also much smaller; suggesting variability in VTC strand has a larger influence on the deviations.

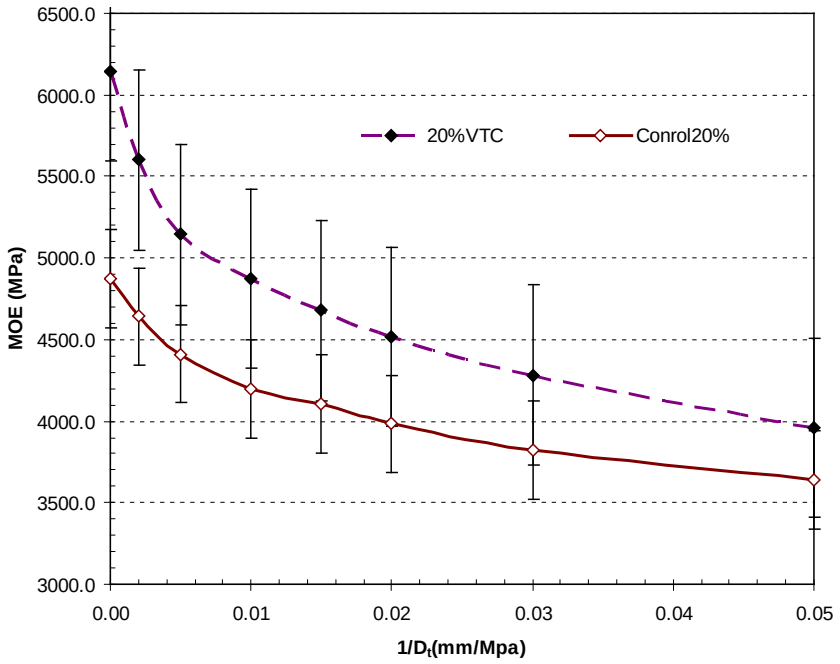

Figure 4.6. Numerical and analytical results of bending MOE versus $1/D_t$ for 20 percent VTC strand by weight and control at 10% compaction.

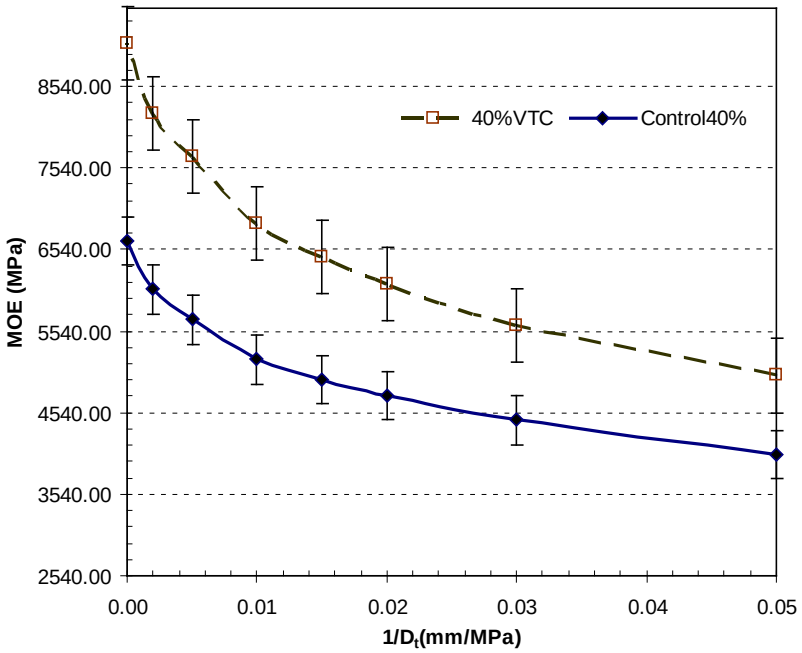

Figure 4.7. Numerical and analytical results of bending MOE versus $1/D_t$ for 40 percent VTC strand by weight and control at 10% compaction.

Table 4.1: Experiment (in bending) and MPM simulation (in bending) moduli for control and different weight VTC addition.

	MOE (GPa)				
Surface Content	**Control**	**Stdv**	**VTC**	**Stdv**	**% Increase[1]**
20% Expt	11.6	1.57	12.4	1.57	6.9%
20%, 1% PF MPM	**4.0**	**0.41**	**4.6**	**1.11**	13.6%
20%, 25% PF MPM	**4.2**	**0.40**	**4.9**	**1.12**	16.1%
20%, 100% PF MPM	**4.9**	**0.28**	**6.1**	**1.00**	26.1%
40% Expt	12.9	1.72	16.1	2.47	25%
40%, 1% PF MPM	**4.8**	**0.37**	6.3	0.94	30%
40%, 25% PF MPM	**5.2**	**0.38**	**6.9**	**0.73**	32%
40%, 100% PF MPM	**6.6**	**0.43**	**9.1**	**0.67**	37%

1) Increase of VTC compared to control.

4.4 Laminate Beam Analysis for Bending (Symmetry Three Layers Composites Model)

For a symmetric, three-layer OSB panel having two different materials with modulus E_1 and E_2 for the outer layers and inner layer (see chapter 3, Figure 3.15) in the ratio $R = E_1/E_2$, a central layer having thickness t_2, and two outer layers having the same thickness of t_1. The moment (M) and curvature (κ) relation for this structure is $M=C_\kappa\kappa$ (Nairn, 2006). Where:

$$C_\kappa = \frac{12}{hE_1t_1^3}\frac{R\lambda^3}{1+6R\lambda+12R\lambda^2+8R\lambda^3} \qquad (4.5)$$

where $\lambda = t_1/t_2$ and h is the total height of the panel. For a rectangular beam $C_\kappa = 1/(E_b^* I)_{eff}$; $I=Bh^3/12$ is the bending moment and E_b^* is the effective bending modulus. Solving for E_b^* gives:

$$\frac{1}{E_b^*} = \frac{h^3}{E_1t_1^3}\frac{R\lambda^3}{1+6R\lambda+12R\lambda^2+8R\lambda^3} \qquad (4.6)$$

For our simulated OSB panels with 50% by volume surface and core, $t_1=t_2/2$, $\lambda = t_1/t_2=1/2$.

$$\frac{1}{E_b^*} = \frac{h^3}{E_1t_1^3}\frac{R}{8(1+7R)}$$

Since $h=4t_1$

$$E_b^* = \frac{(1+7R)E_1}{8R} = E_1\left(\frac{7}{8}+\frac{1}{8R}\right) \qquad (4.7)$$

For example, consider the panels, E_1 of 9936MPa, E_2 of 423MPa (i.e. the core layers, use the property in transverse direction of wood) and R = 9936MPa/423MPa = 23.49. Substitution into equation (4.7) gives E_{eff} = 8746.9MPa. This number is close to the results of the MPM simulation (8303MPa) for no gaps, $1/D_t = 0$ and compaction of 0%.

Furthermore, E_b^* is proportional to 1/(1-C) for different level of compaction if E_1 is assumed to increase to E_1/(1-C), where C is compaction level. Therefore equation 4.7 becomes

$$E_b^* = \frac{E_1}{1-C}\left(\frac{7}{8}+\frac{1}{8R}\right) \qquad (4.8)$$

For OSB panels with gaps, E_1 and E_2 are

$$E_1 = E_L \frac{\langle L \rangle}{\langle L \rangle + \langle G_L \rangle} \quad \text{and} \quad E_2 = E_R \frac{\langle W \rangle}{\langle W \rangle + \langle G_W \rangle} \qquad (3.9)$$

where E_1 and E_2 are the longitudinal and radial modulus of the strands, <L> and <W> are the average length and width of the strands, and <G_L> and <G_W> are the average gaps between strands in the surface and core layers (see chapter 3 for more details).

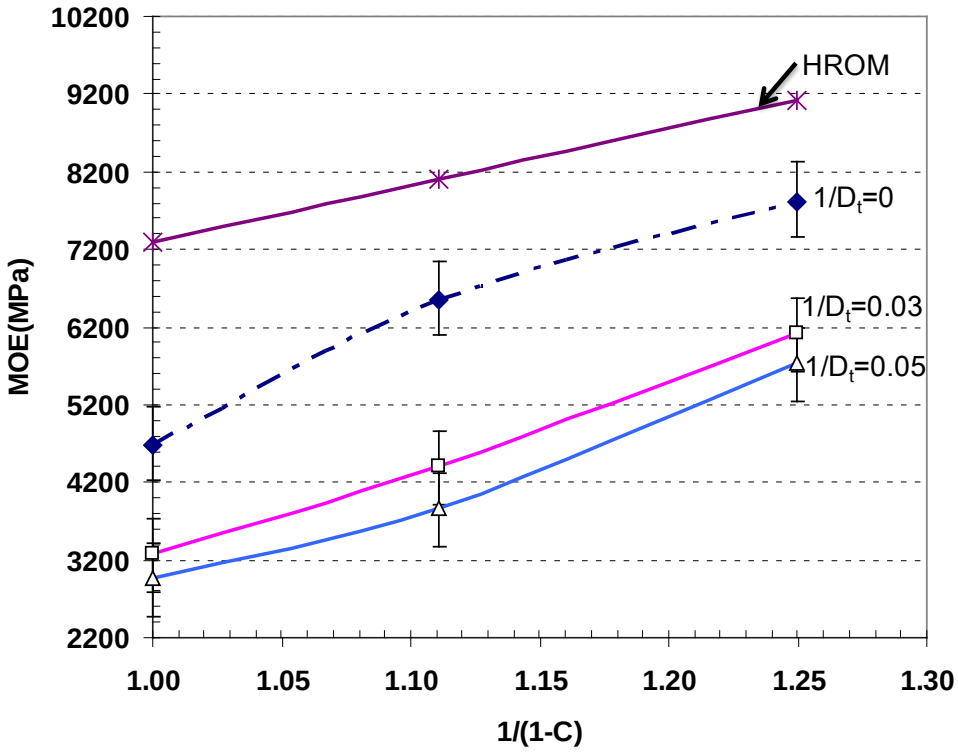

Figure 4.8. Re-plot result of Figure 4.4 for this value of $1/D_t$.

Figures 4.8 re-plots the results of Figures 4.4 as a function of 1/(1-*C*) along with the analytical model (homoginzed rule of mixture-Eq. 4.8). Simulated MOE is lower than HROM but simulated MOE are closest for the case of $1/D_t=0$. There was a further decrease of MOE as $1/D_t$ increased, which the model cannot consider. The reason MOE in bending is below HROM while it was closer or higher in tension may be that gaps

affect the real material more in bending. In other words equation 4.9 is a worse approximation in bending than in tension.

4.5 Summary and Conclusions

The main results of this study are that MPM simulations can evaluate the modulus of OSB panels in bending accounting for realistic strand undulations and for the effective stiffness of the adhesive bonds between strands. If there are no undulations, the influence of glue is still there. Thus glue is even more important for bending properties than it is for tension. The higher stiffness of strands and grain direction affects the panel's moduli greatly.

We estimated that the tensile modulus of OSB panels with inadequate gluing is approximately 15-20% lower than the one with full gluing. It could also be improved in adhesive application in the case of load in bending by slightly more (15-25%). There is more increase of MOE in bending than MOE in tension from 25% to 100% percent of adhesive coverage and from 1% to 100% glue coverage but there is about the same percent of increase for MOE from 1% to 25% glue coverage.

Mechanical properties of wood-strand composites can be improved with enhanced strands such as VTC strands. The potential increase in MOE is larger for 40% VTC than for 20% VTC. Finally, the glue influences the MOE enhancement. The better the glue, the more VTC strands will improve the MOE.

MPM simulations gave good agreement with simple laminate theory when there are no gaps. However, there was a larger deviation of MOE from laminate theory when gaps were presented. Therefore, gaps affects bending MOE more than tension MOE and require advanced modeling for accurate results rather the simple laminate theories.

References

Barnes D (2000) An integrated model for the effect of processing parameters on the strength properties of oriented strand wood products. Forest Prod J 50(11/12):33–42

Barnes D (2002a) A model of the effect of fines content on the strength properties of oriented strand wood composites. Forest Prod J 52(5):55–60

Barnes D (2002b) Orientation of OSB and particleboard strands for high-strength oriented strand lumber and panel products. Forest Prod J 52(9):31–39

Bodig J, Jayne BA (1982) Mechanics of wood and wood composites. Van Nostrand Reinhold Company, Toronto

Budman H, G Painter, and Pritzker (2006) Prediction of oriented strand board properties from mat formation and compression operating conditions. Part 2: MOE prediction and process optimization. Wood Sci Technol 40:291–307.

Goldsmith, W. (1960) Impact: The theory and physical behavior of colliding solids. London, Edward Arnold (Publishers) Ltd.

Gibson, L. J., and M. F. Ashy (1997) Cellular solids: Structure and properties. Cambridge University Press, UK.

Hunt, M. O., and Suddarth, S. K. (1974) ‘‘Prediction of elastic constants of particleboard.’’ Forest Products J., 24(5), 52–57.

Kelly MW (1977) Critical literature review of relationships between processing parameters and physical properties of particleboard. General Technical Report (FPL-10), Forest Products Laboratory, Forest Service, US Department of Agriculture

Lam, F., and Varoglu, E. (1990) ‘‘Effect of length on the tensile strength of lumber.’’ Forest Products J., 40(5), 37–42.

Lee C (2003) Modeling and optimization of the continuous oriented strand board manufacturing process. MASc. Thesis, University of Waterloo, Ontario

Lee J, Wu Q (2003) Continuum modeling of engineering constants of oriented strandboard. Wood Fiber Sci 35(1):24–40

Nairn, J.A. (2006) On the calculation of energy release rates for cracked laminates with residual stresses, International Journal of Fracture, 139, 267–293.

Rathi V (2009) Bending property enhancement of wood strand composite using viscoelastic thermal compression *MS Thesis* Oregon State University, Corvallis, OR.

Triche, M. H., and Hunt, M. O. (1993) ‘‘Modeling of parallel-aligned wood strand composites.’’ Forest Products J., 43(11/12), 33–44.

Wang, Y. T., and Lam, F. (1998) ‘‘Computational modeling of material failure for parallel-aligned strand based wood composites.’’ Computational Mat. Sci., 11(3), 157–165.

Xu W (1999) Influence of vertical density distribution on bending modulus of elasticity of wood composite panels: a theoretical consideration. Wood Fiber Sci 31(3):277–282.

Xu W, Suchsland O (1998) Modulus of elasticity of wood composite panels with a uniform density profile: A model. Wood Fiber Sci 30(3):293–300.

CHAPTER 5 – EFFECT OF STRAND LENGTH AND GAP SPACING ON MECHANICAL PROPERTIES OF WOOD STRANDS AND WOOD BASED COMPOSITES

Abstract

The length of the strands in wood-based composites affects the efficiency of stress transfer between the strands and thus affect mechanical properties. The slenderness or aspect ratio (strand length over thickness) is the key geometry variable. If the aspect ratio (AR) decreases the stress transfer efficiency decreases and there are more stress concentrations at strand ends. This result leads to decreased efficiency for carrying stress in the wood-strand composites and therefore to inferior mechanical properties.

In this study, the effect of the AR and the effect of gap spacing between strands on the mechanical properties of wood based composites were studied using numerical and analytical models. The results of the simulations were compared with an analytical shear-lag model and laminated plate theory. The numerical simulations were consistent with the shear-lag model and laminated plate theory. The results showed that increased AR or decreased gap spacing increased stiffness. Furthermore, it is noted that it is difficult to study the effect of AR by experiment but is straight forward with numerical simulations. In other words, numerical simulations can be a useful tool for design of strand board products.

5.1 Introduction

The length of the strands in wood composites affects the stress transfer between strands. Increasing strand length should increase load carrying efficiency and decrease stress concentrations at the ends. Thus longer strands should improve the overall performance of the composites. It is analogous to fiber reinforced composites where the fiber aspect ratio effects the amount of stress transfers from one member to the next (Hull and Chyne 1996 and references there in).

Orientation of wood strands with length/width of at least 3 can produce panel products with greater bending strength and stiffness in the oriented or aligned direction (Wood Handbook, chapter 10, 1996). An early study by Post (1958) concluded that

bending stiffness is fairly well correlated to the length-to-thickness ratio of the particles and constantly increased up to a ratio of at least 300. Wang and Lam's (1999) study developed quadratic regression models to relate bending MOR and MOE of oriented flake boards to aspect ratio (AR), surface orientation, and panel density. They concluded that for strand lengths of 50-100 mm and a thickness of 0.6 mm (AR from 67 to 133) that higher AR was better. Weight and Yadama (2008a) concluded that for the production of laminated strand veneer composites the optimum AR ratio is 430. Recently, Cloutier et al (2009) showed that AR affects the bending properties of strandboard but not the internal bonding. The higher AR leads to increase in bending MOR but a decrease in compression MOR.

Furthermore, beside AR, studies have shown that interfacial stiffness also affects the overall performance of wood based composites. Hashin (1991), Nairn (1996), and Nairn and Le (2009) have studied the effect of the interface on the mechanical properties of composites but did not incorporate of the effect of interface with AR on mechanical properties of wood-based composites. The interrelation between the interfacial stiffness and AR to the mechanical properties of wood strand composites has not been investigated. Therefore, the overall objective of this study was to use numerical and analytical techniques to study the effect of AR, interfacial stiffness, and strand properties on the mechanical properties of wood-strand composites.

5.2 Literature Review

The aspect ratio (L/t where L is the strand length and t is the strand thickness) has often been used to develop empirical equations to study the effect on mechanical properties of wood strand composites. In fiber-reinforced polymer composites one refers to the aspect ratio as the length of the fiber over the diameter of the fiber. Theoretically, this aspect ratio needs to be about 100 or more to have high stress transfer efficiency (Hull and Chyne 1996 and references there in). This can be accomplished with synthetic fibers but is harder with natural fibers such as wood or hemp. However, in wood-based composites we consider instead wood strands, which consist of many wood fibers, vessels, rays, tracieds and so on is a solid rectangular sheet. As a result the length of the

strand can be controlled in processing from raw materials. These strands are able to achieve much longer length than wood fibers (or other natural fibers). The length over thickness can therefore be larger. The length or width ratio may also play a role, but this study focused of AR or length over thickness.

Recently, studies have shown that the mechanical properties increased and reached a constant value as aspect ratio increased (Post 1958). Post (1958) and Suchsland (1968) both found that the modulus of rupture of flake board increases with an increasing AR. They showed that MOR properties asymptotically approach a constant value at high aspect ratios. Furthermore, recent studies of Weight and Yadama (2008a) capture images and studied the effect of strand length but these studies were not able to incorporate realistic morphology and undulations to see how mechanical properties are affected by different levels of undulation as the level of compaction increased. Thus prior work has been limited to observations.

5.3 Results and Discussion

Numerical simulations were done using NairnMPM code and doing 2D calculations. The structure of OSB was randomly generated and it was based on various values for strand length and gaps between strands. OSB panels consisted of three different layers. The top layer had 25% of the strands (top surface strands) that are perpendicular to 50% of the strands in the middle layer (core strands). The middle layer strands were perpendicular to the bottom layer that had the remaining 25% of the strands. The top and bottom surfaces have L direction in x-axis. The core layer have L direction in Z direction or normal to the analysis plane.

We simulated four different cases with various strand lengths and gaps in the face layers. Case 1, had mean strand length of 75 mm with standard deviation of 20 mm and gap of 15 mm with standard deviation of 4.95 mm. Case 2, had mean strand length of 75 mm with standard deviation of 20 mm and gap of 30 mm with standard deviation of 4.95 mm. Case 3, had strength length of 150 mm with standard deviation of 20 mm and gap of 15 mm with standard deviation of 4.95 mm. Case 4, had mean strand length of 150 mm with standard deviation of 20 mm and gap of 30 mm with standard deviation of 4.95 mm.

In all these four cases, we fixed the core strand width and gap at 25 mm with standard deviation of 3 mm and 10 mm with standard deviation of 1 mm, respectively. Figure 5.1 is sample initial geometry with zero compaction for Case 4.

Figure 5.1. Sample calculation of commercial OSB.

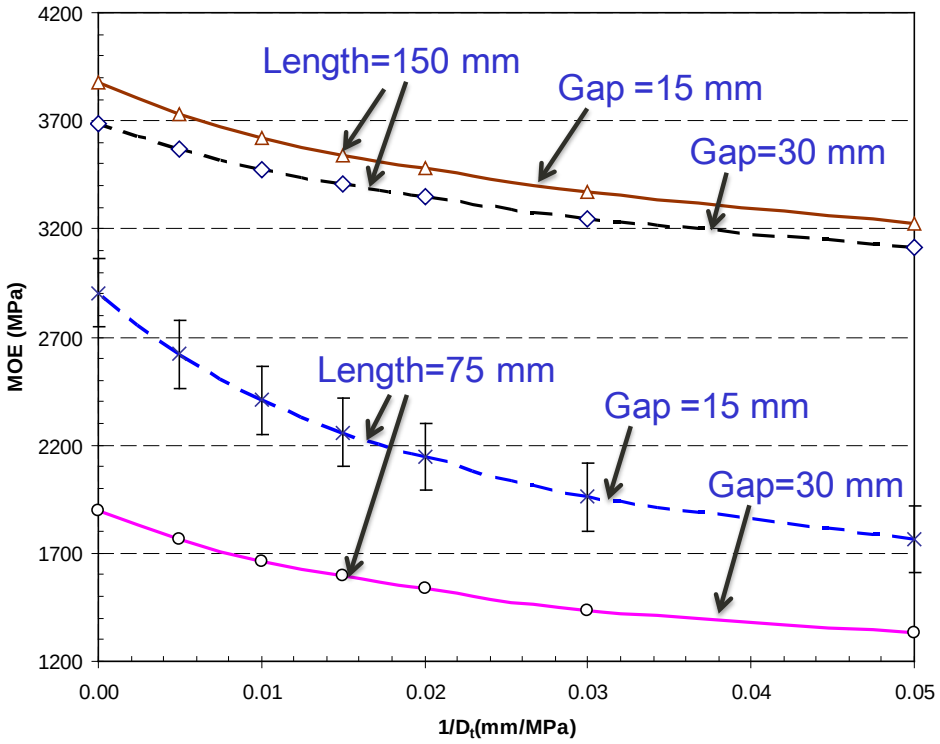

Figure 5.2. MPM calculation of MOE of OSB panel with unmodified strand as a function of $1/D_t$ for different strand length and gap size at zero compaction.

Figure 5.2 shows MPM calculation of MOE of OSB panels with unmodified strand as a function of $1/D_t$ for different strand lengths and gap spacings at zero

compaction. For constant gap spacing, as the strand length increased, MOE increased. As the strand length increased from 75 mm to 150 mm with strand gap of 15 mm or from 75 mm to 150 mm with strand gap of 30 mm, there is more load carried in each individual strand and therefore higher MOE. The fibers (strands) are more continuous when strand length is longer. Longer strand length also results in less strand undulation. This is because as strand length gets longer and longer, it approaches the case with no gaps for which there would be no undulations (see chapter 3 and 4).

Likewise, decreasing gap spacing at constant strand length increased MOE. In Figure 5.2 and Figure 5.3, as the gap spacing decreased with a fixed strand length from 30 mm to 15 mm for strand length of 75 mm or for 30 mm to 15 mm with strand length of 150 mm, MOE increased. This is because as the gap spaces decrease there is less strand undulation and there is more continuous strands to carry more load. This results in higher stress transfer between phases (or strands).

For all cases, MOE decreased as $1/D_t$ increased. The relative amount of decrease was smaller for longer strands. As shown in chapter 3, the effect of D_t goes away when there are no gaps, which is analogous to very long strand lengths. Similarly, Figure 5.4 shows MPM calculation of MOE of OSB panel with unmodified strand as a function of $1/D_t$ for different strand length and gap spacings, but at 10% compaction. The same behavior is obtained for all cases as seen at zero compaction. However, the effect of interface on MOE was different due to development of strand undulation. D_t influenced the OSB with shortest strands (75mm) and largest gaps (30mm) the most.

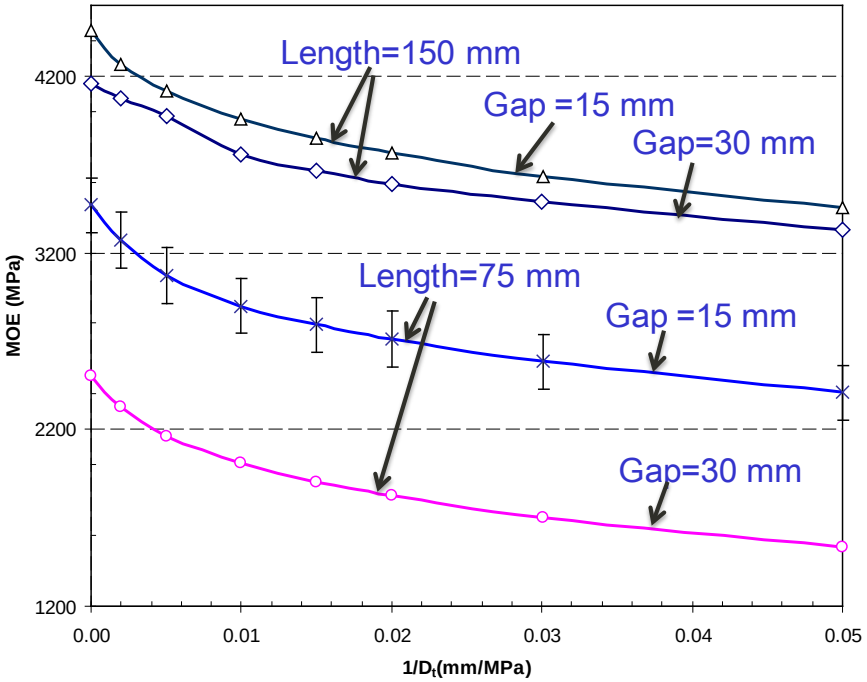

Figure 5.3. MPM calculation of MOE of OSB panel with unmodified strand as a function of $1/D_t$ for different strand length and gap size at 10 percent compaction.

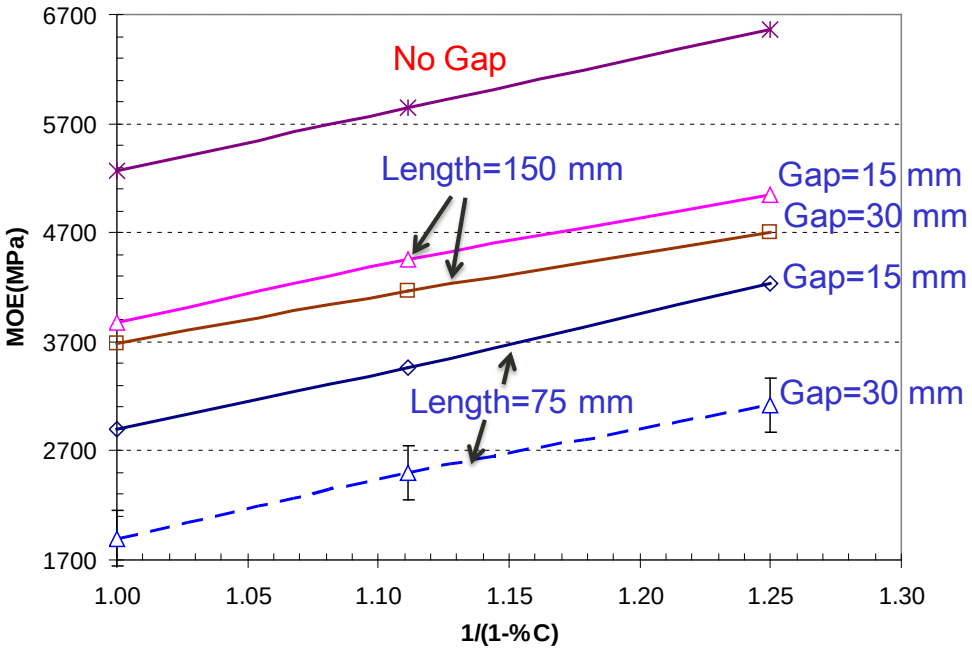

Figure 5.4. MPM calculation of MOE of OSB panel with unmodified strand as a function of $1/(1\text{-}\%C)$ and the glue line stiffness ($1/D_t$=0).

Figure 5.4 is re-plot the results for MOE with different strand lengths, and gap spacings with constant interfacial stiffness ($D_t = \infty$) along with the homogenized model for case with no gaps (in the previous study [see Chapter 3]). While fixing gap spacing, as strand length increased from 75mm to 150mm, MOE increased and approached the case for no gaps. Likewise, when gap size decreased at constant strand length, MOE is increased and approached the case for no gaps.

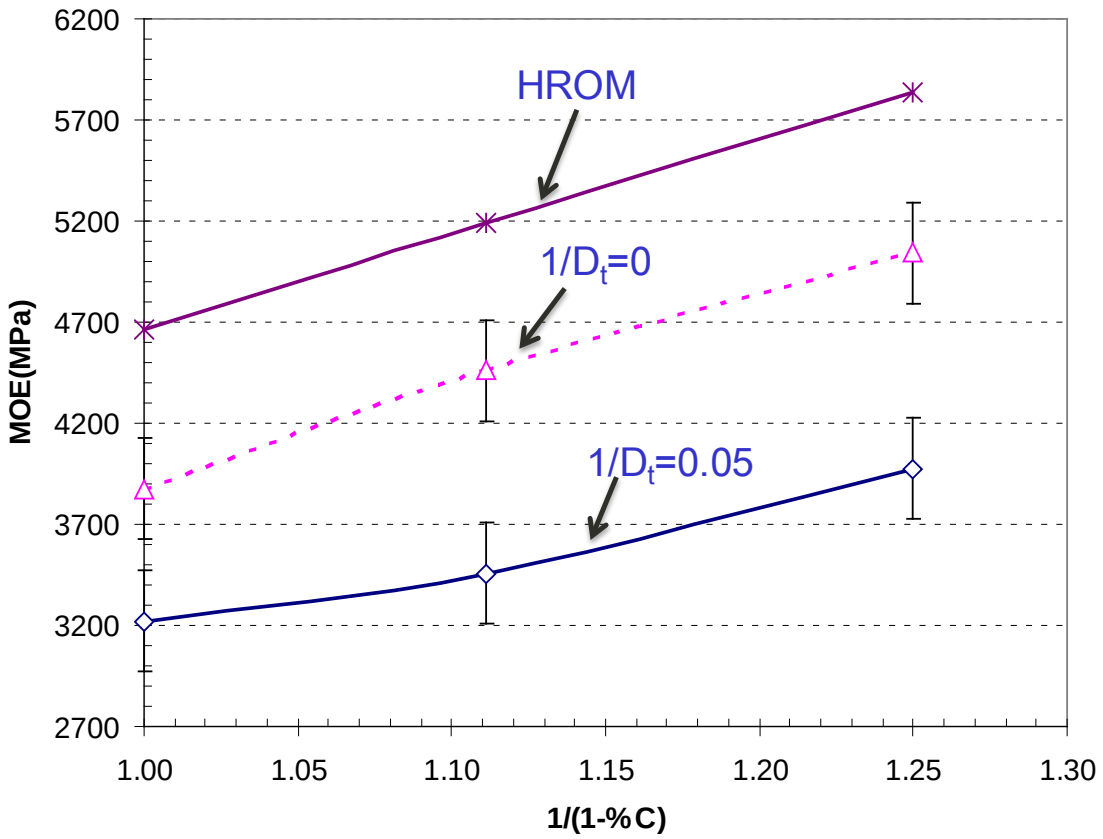

Figure 5.5. MPM calculation of MOE of OSB panel with unmodified strand as a function of 1/(1-%*C*) and different glue line stiffness for strand length of 150 mm and gap of 15 mm.

Figure 5.5, plots of simulated MOE as function of 1/(1-C) and different glue-line stiffness for strand length of 150 mm and gap of 15 mm along with HROM (see previous

study in chapter 3 for no gaps). At interface D_t increased, MOE increased. The effect of interface on MOE is more significant at higher compaction where there is more strand undulation. The HROM is higher than the simulated values. Similarly, Figure 5.6, plots of simulated MOE as function of 1/(1-C) and different glue-line stiffness for strand length of 75 mm and gap of 15 mm along with HROM. In this case simulated MOE is much lower than HROM. As the strand length is lower, the load is carried less efficiently by the strands.

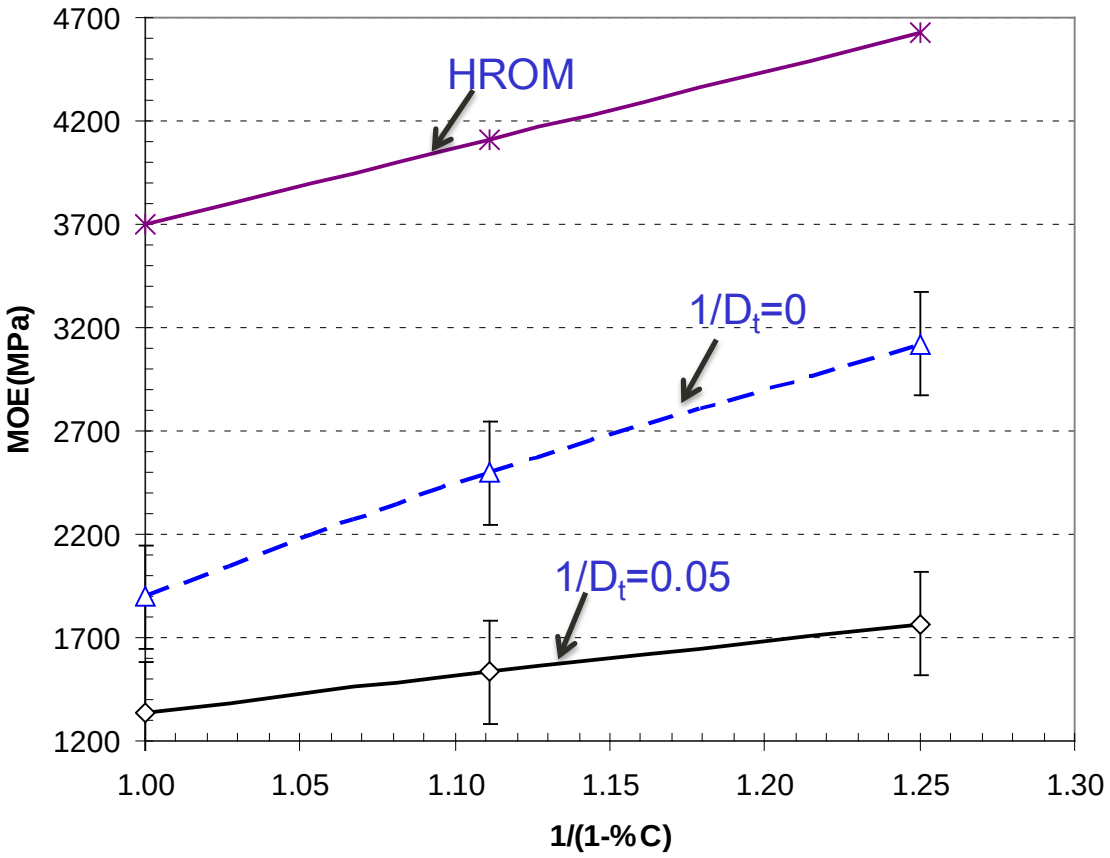

Figure 5.6. MPM calculation of MOE of OSB panel with unmodified strand as a function of 1/(1-%*C*) and different glue line stiffness for strand length of 75 mm and gap of 30 mm.

5.4 Shear Lag Model

As shown previously, HROM cannot account for the interface. But shear lag methods have been used in composites to analyze fiber aspect ratio and interface effects (Nairn 2005). Here we adapted the shear-lag approach to account for interfacial, strand length, and strand gap effects. The shear-lag equation for MOE of load in tension parallel to direction of the grain in all strands (i.e. LVL geometry) is:

$$E_x = \eta_w(D_t, AR)E_wV_w + E_mV_m \tag{5.1}$$

where D_t is interfacial stiffness parameter; V_w and V_m are volume of wood and glue; E_w and E_m are elastic moduli of wood and glue; η is an efficiency factor that describes the ability of the interface to transfer load into the reinforcing phase. The efficiency factor depends on interfacial D_t and aspect ratio. The efficiency factor can be modeled by stress transfer analysis, such as shear-lag analysis, resulting in (Hull and Clyne 1996):

$$\eta_w = \left(1 - \frac{\tanh\left(\frac{\beta t}{2}\left(\frac{l}{t}\right)\right)}{\frac{\beta t}{2}\left(\frac{l}{r}\right)}\right) = 1 - \frac{\tanh\gamma}{\gamma} \tag{5.2}$$

where $\gamma = \frac{\beta^*(AR)}{2}$, $\beta^* = \beta t$ and $AR = \frac{l}{t}$

Here, β is the shear-lag parameter; and l and t is length and thickness of the strands. The preferred shear-lag parameter has the form of (Nairn 2005):

$$\beta^{*2} = \left(\frac{\frac{E_mV_m + E_wV_w}{E_mE_wV_mV_w}}{\left(\frac{V_w}{3G_w}\right) + \left(\frac{V_m}{3G_m}\right) + \left(\frac{1}{t^*D_t}\right)}\right) \tag{5.3}$$

where G_w and G_m are the shear moduli for wood and glue and t^* is strand-to-strand spacing. Early shear-lag analysis always assumed a “perfect” interface implying continuous displacement between phases (Cox 1952). Thus the early models could not

account for interfacial stiffness effects and the modulus depended only on the mechanical and geometric properties of the phases. The new shear-lag parameter in Equation 5.3 adds interfacial stiffness effect through the term in D_t. Canceling terms and rearranging, γ becomes:

$$\gamma^2 = \left(\frac{\frac{1}{E_m V_m} + \frac{1}{E_w V_w}}{\frac{V_w}{3G_w} + \frac{V_m}{3G_m} + \frac{1}{t^* D_t}} \right) * \frac{l^2}{4} \qquad (5.4)$$

To account for the gap spacing we used:

$$V_m = \frac{\langle G \rangle}{\langle G \rangle + \langle L \rangle} \quad \text{and} \quad V_w = \frac{\langle L \rangle}{\langle G \rangle + \langle L \rangle} \qquad (5.5)$$

where G and L is the length and gap spacing. These volume fractions were derived from the geometry in Figure 5.7. With shear lag model and length and gap values, Eq 5.1 gives MOE of LVL specimens for face layers of OSB. The set MOE for OSB, the HROM can be modified by using E_x in eq 5.1 for surface layers initial modulus and use prior approach for core layer. For OSB with 50% core layer (as in all simulation), the new modulus is $E = \frac{E_x + E_C}{2(1-C)}$ (5.6)

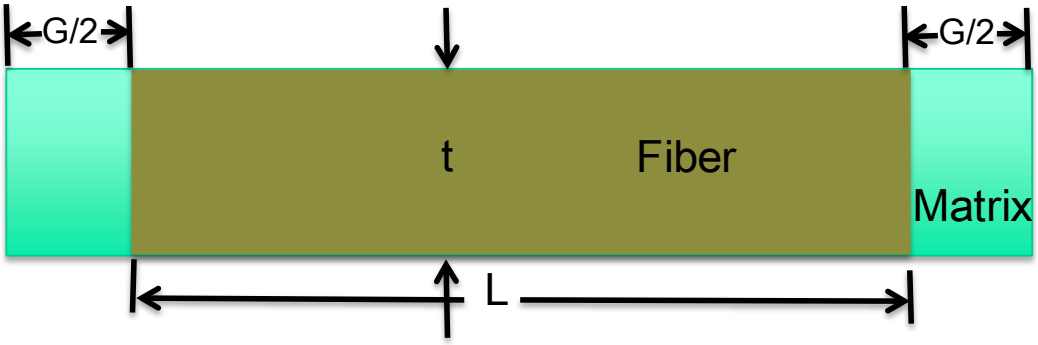

Figure 5.7. Embedded fiber (strand) into matrix (glue).

As shows in Figure 5.8, the results of MOE as the function of aspect ratio (strand length over strand thickness) in OSB for different D_t. Here the thickness of the strand is

fixed and is equal to 0.8mm and MOE of individual strands is E_w=9936 MPa, the MOE of glue is 1500 MPa, shear modulus of wood is 743MPa, shear modulus of glue is 500MPa, volume of wood is 0.83% and volume of glue is 0.17% with strand length of 150 mm and strand gap of 30 mm. Figure 5.8 are the results of equation 5.5 with different D_t. As aspect ratio increases, modulus of the composites increase and level off. For optimum of stress transfer efficiency, the AR is around 200.

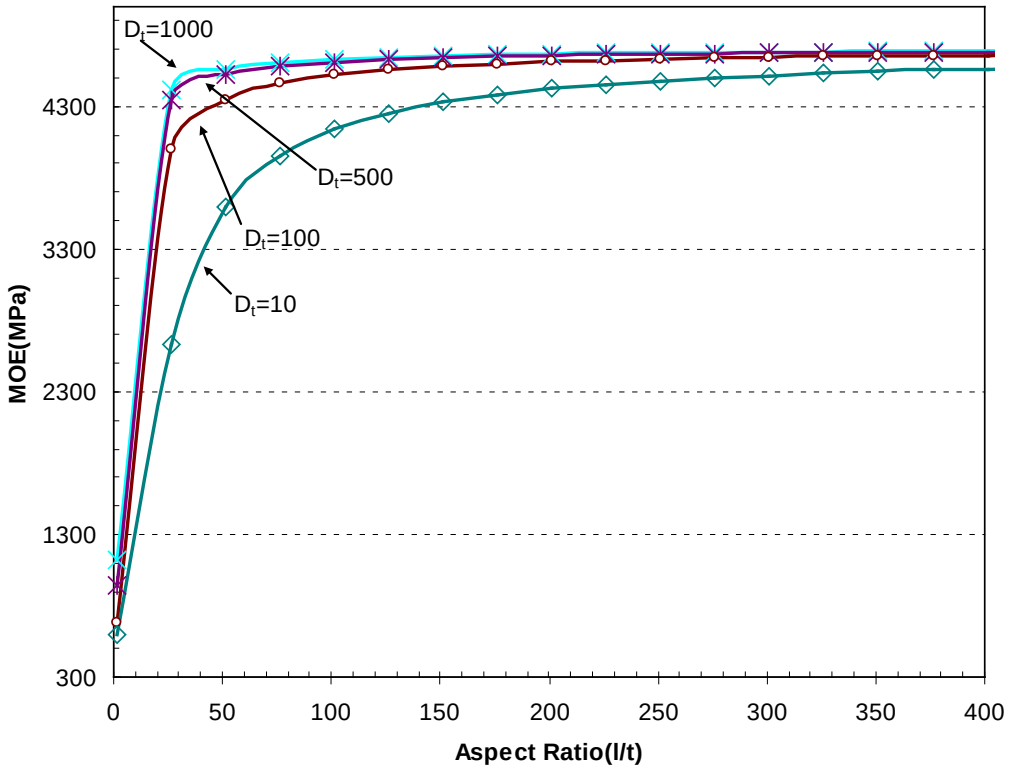

Figure 5.8. The results of MOE as the function of aspect ratio (strand length over strand thickness) in OSB for different D_t (where D_t=100 [$1/D_t$ =0.01 is 25% glue coverage; D_t = 60 [$1/D_t$=0.016] is 1% glue coverage).

Figure 5.9 is shows MOE as a function of AR at constant gap size. The results are compared to HROM modified by shear lag analysis for $1/D_t$=0.05. MOE increased as AR increased. The numerical results are lower than the analytical results of combine HROM with equation 5.5. Numerical values of MOE approached to analytical results as AR

increased. Furthermore, there is a higher percentage of increase in MOE by numerical than the combine HROM and shear-lag model (103% increased for numerical calculation and 22% increased for shear-lag calculation).

Similarly, Figure 5.10 is re-plot the results of Figure 5.2 of the effect of MOE for different values of AR along with results of equation 5.5 combined with homogenized model for $1/D_t$ =0. The numerical results are still lower than the analytical results of combined HROM with equation 5.5. However, as AR increased, MOE approached analytical results.

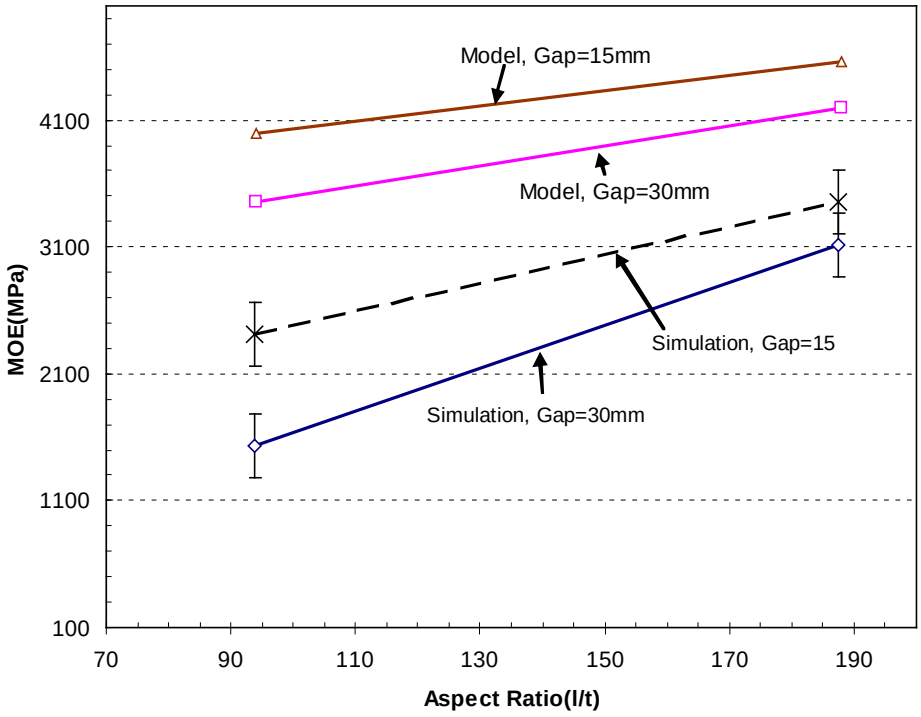

Figure 5.9. Simulated MOE and results of shear-lag Equation 5.5 for $1/D_t$=0.05.

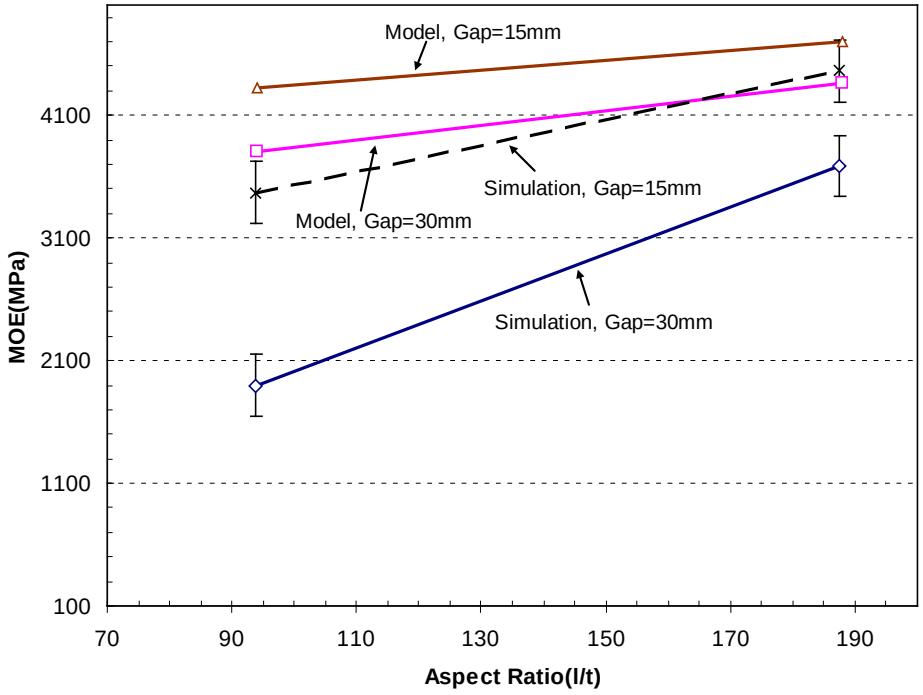

Figure 5.10. Simulated MOE and results of shear-leg Equation 5.2 for $1/D_t=0$.

5.4 Summary and Conclusions

We can conclude that, increases in strand length or decreases in gap spacings in surface layers increases MOE. Strand length has a large impact on the mechanical properties of wood-based composites when it reach optimum level at around AR = 200. One way to increase load carrying capacity in wood composites panel is to increase interfacial stiffness but this is often more difficult and costly. This is because to increase interfacial stiffness more resin can be used but this will result in higher cost for more resin consumption. Therefore, an increase in fiber aspect ratio (strand length) may be an easier route. As an added benefit, the role of resin should decrease as the strand length increases.

Shear-lag model can incorporate interfacial stiffness into the shear-lag parameter that thereby predict modulus as a function of the phase's properties, phase geometry (aspect ratio) and interfacial stiffness. From the shear-lag model, the effect of strand

properties, aspect ratio and glue-line interfacial stiffness can be obtained for wood-strand based composites.

Finally, it is easy to setup MPM models and simulate the mechanical properties of OSB as a function of strand length, gap spacings, and interfacial properties. It would be very difficult to study these effects in experiments. This is a major reason for doing numerical studies on wood-based composites.

References

Cloutier, A., K. Beck, a. Salenikovich, and R. Beauregard (2009) Effect of Strand Geometry and Wood Species on Strandboard Mechanical Properteis. Wood and Fiber Science 41(3): pp 267-278.

Nairn, J.A. (2005) Generalized shear-lag analysis including imperfect interfaces. Adv. Comp. Letts., 13, pp. 263-274.

Post, P.W. (1958) Effect of Particle Geometry and Resin Content on Bending Strength of Oak Flake Board. Forest Products Journal. October, pp. 317-322.

Suchsland, Otto. (1968) Particle-Board From Southern Pine. Southern Lumberman. December, pp. 139-144.

Halpin, J.C. (1984) Primer on Composite Materials: Analysis. Technomic publishing Co. Inc., Lancaster, Pennsylvania, pp. 130-142.

Hull, D., T.W. Chyne (1996) An introduction to composite materials, 2nd edition, Cambridge Univ. Press.

Wang K.Y., Lam F. (1999) Quadratic RSM Models of Processing Parameters for Three Layer Oriented Flakeboards. Wood and Fiber Science 31(2): pp 173-186.

Weight S.W., Yadma V. (2008) Manufacture of laminated strand veneer (LSV) composite. Part 1: Optimization and characterization of thin strand veneers. Holzforschung 62(6): 718-724.

U.S. Department of Agriculture (1987) Wood Handbook. Agriculture Handbook No. 72, Superintendent of Documents, Washington D.C. 466pp.

CHAPTER 6 – EFFECT OF DENSITY ON MECHANICAL PROPERTIES OF WOOD-STRAND COMPOSITES

Abstract

The panel density profile affects the mechanical properties of wood-based composite panels. In order to produce the highest mechanical properties of a wood-based composite panel while maintaining the lowest cost, computer tools can be used to study variables that affect the panel's density profile.

In this study, parameters that may affect the vertical density profile (VDP) such as compaction (densification) levels, compaction rate, yield stress, and stiffness were addressed. Both experimental and numerical methods are used to study the VDP of OSB panels. The results of 2D simulations gave VDPs that resemble experimental results. Reducing yield stress of the surface strands or increasing yield stress of the core strands had small effects on the surface (face) layer density. Increasing the percent of compaction increased density variations. Increasing the compaction rate increased the surface density. Reducing stiffness of the surface layer had the largest effects on VDP. The results of 3D simulation gave results different from 2D simulations although stiffness effects were similar. More work is needed to get better simulations of the vertical density profiles.

6.1 Introduction

In bending, the highest stresses are located at the surface of the panel. Thus, it is advantageous to have a higher wood density near the surface where it has a higher impact on the bending stiffness and strength than does the core. In order to achieve better properties, OSB is designed to have a U-shape vertical density profile. The higher density peak close to the top and bottom surfaces with the lower density in the core yields panels with higher bending modulus of elasticity (MOE) than would be found in a panel with uniform density profile. In processing of OSB, the heated platens soften the wood strands (i.e. reduced Young's modulus and yield stress) near the top and bottom surfaces of the panel. The strands in the core of the panel are not heated as much and therefore do

not compress as easily. The higher degree of compression near the surface and the lower degree of compression in the core causes the formation of the U-shaped density profile in the OSB panel (Wang and Winistorfer 2000).

A full simulation model would have to account for mat formation, compression, heat-time-temperature effects on the strands and strand-to-strand interactions. The changes of temperature and moisture content with time and space during compression would cause the mechanical properties to change at each position and further complicate the problem. Including all these effects is beyond the scope of the current research project. Therefore, simplifying assumptions are required and some of the complexities must be accounted for empirically.

Xu and Suchsland (1998) presented a theoretical model for the prediction of OSB MOE. The model is based on an overall elastic energy balance, with the applied bending energy being equivalent to the sum of the elastic energy stored in each strand under the assumption of negligible frictional losses. Xu (1999) extended this work by applying it to wood composites with a non-uniform VDP. He assumed an idealized VDP characterized as a Fourier transform and applied it to a panel with randomly oriented strands. The model predictions were not validated against experimental data. Lee and Wu (2003) presented a continuum model capable of predicting MOE based on laminate plate theory and the mechanical properties of the strands and resin. Unfortunately, their model predictions exhibited some discrepancies from the experimental results. This may have been caused by their assumption of a uniform VDP. Budman et al (2006) extended the original work of Xu and Suchsland (1998), where the data from a simulated panel was used as input to the MOE model rather than assuming a particular strand size distribution and an idealized VDP characterized in terms of a Fourier transform (Xu 1999).

The panel density is related to the degree of wood densification and it has significant influence on the bonding strength (Humphrey 1991, Schulte and Fruhwald 1996, Jin and Dai 2004). High bonding strength usually demands high panel density, but high density also means high cost and other undesirable properties of panels, such as low dimensional stability. An optimum strategy is needed to minimize panel density while

maintaining good bonding properties (and mechanical properties) in the manufacturing of wood composites.

Recent studies on wood strand-composites have not analyzed how the mechanical properties of wood-strand composites change as the level of compaction increases (density increases). In processing of the panel, strands are mixed with resin and wax to form a mat and then compacted between two hot plates. The manufacturers normally set the target density of the panel to some trial and error values without knowing how much the density changed due to different levels of compactions (and the mechanical properties associated with it). More compaction is needed for species with lower density, and less compaction is needed for higher density species.

In order to meet the minimum mechanical properties requirement while not wasting the raw material, we need to know how the mechanical properties change as levels of compaction increase. In chapter 3, we used computer simulation to study the effect on mechanical properties as overall panel density increased. Here, the numerical model was also used as a tool to study the VDP of wood-strand based composites. The results of the numerical simulation of density profiles of OSB panels were compared to the density profiles that were obtained by X-ray profilometer. The simple homogenized rule of mixture model was then used to interpret some results on mechanical properties as a function of panel density.

6.2 Method and Procedures

In the first part of this study, 2D MPM (material point method) simulations were done using the methods that were described before (see chapters 3 and 4). The simulated mass was obtained from the results of MPM compaction for different levels of compaction. The simulation density was then calculated by dividing the mass on each node by the unit of cell volume in the simulation. The unit cell in the simulation was set at 0.266 by 0.266 mm by 1 mm. The density profiles for different simulation specimens were then obtained across the thickness for the specimens. Due to the variation between simulations of randomly generated specimens, five different simulations were done on different randomly generated structures. The average values of the density profiles were

then obtained. To validate the simulated results, experimental results for the density profile was obtained by X-ray profilometer.

In the second part of this study, 3D MPM simulations of density profile were done. The 3D mat was constructed from a series of random strand layers images. The 3D mat was then compressed and the density profile was then calculated from the output data. The cell volume of the simulation is 0.266 mm x 9.3775 mm x 9.375 mm. The density profile was obtained by dividing the nodal mass by the cell volume. The results were visualized using ParaView (Kitware Inc. 2009).

6.3 Experimental Calculation of Density

An X-ray profilometer (Quintek Measurement Systems, Inc., Knoxville, Tennessee, U.S.A.) was used to measure the density profile for commercial OSB made by Ainsworth (Vancouver BC, Canada). The specimen was cut into 2 inch by 2 inch pieces. The initial geometry such as thickness, length and width was measured and then it was inserted into the analyzer. The weight was also measured and input into the analyzer. The X-ray profilometer was then used to measure X-ray attenuation through the specimen. The density profile at different locations was then calculated based on the initial weight and geometry. The output results of a density profile across thickness were obtained. To insure accuracy, the density profiles of 10 samples from different panels were measured and then averaged.

Figure 6.1 gives the result of the density profile from experiments on ten different specimens. There were some variations of density between specimens. The outer surface is higher in density. That is because the two hot plates contact the surfaces during compaction, which results in higher heat on both surfaces makes the surface strands softer and easier to densify than the core layer.

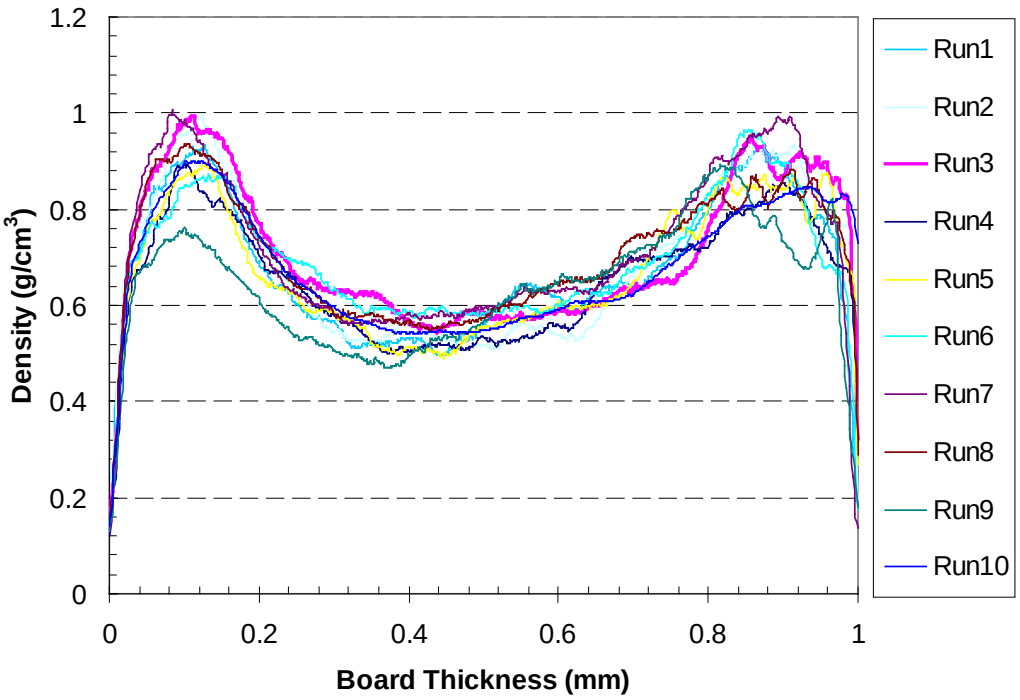

Figure 6.1. The experimental density profile of commercial OSB for 10 replications.

6.4 Simulations of Vertical Density Profile in 2D

The first simulations used 2D MPM. The input mechanical properties for the strand were obtained as explained in chapter 3. The MPM compaction simulations were run by the methods describe in chapter 3.

6.4.1 Commercial OSB

The density profiles across the thickness of the panel were studied and compared to experiments. These simulations had 50% surface strands (25% on each surface) and 50% core strands. All strands had the properties for unmodified hybrid poplar strands. Figure 6.2 shows the results of density profiles for a single simulation at different levels of compaction. It shows oscillations, particular at low levels of compaction. To get better results multiple simulations (5 simulations) on random generated panels were run and the results were averaged. Figure 6.3 has averaged results at various levels of compaction and the curves are smoother. As the levels of compaction increased, the densities

increased. In these simulations (Figure 6.2 and Figure 6.3), the higher densities are on the surface of the panel. The simulations resemble the trends obtained by experiment (see Figure 6.1). A compaction level between 50% and 60% is closest to the experiments.

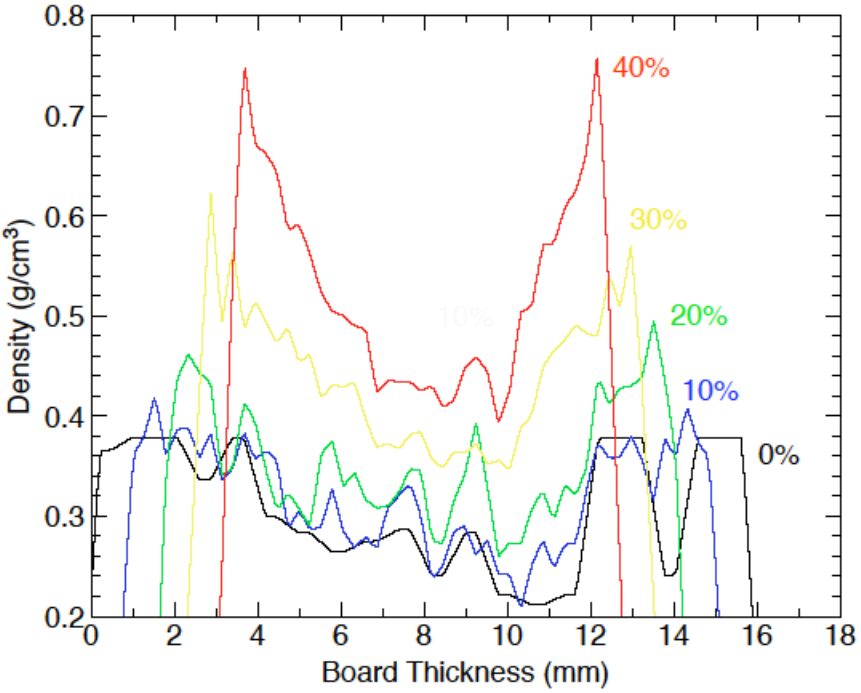

Figure 6.2. Simulated density profile of commercial OSB panel at compaction of 64 m/sec.

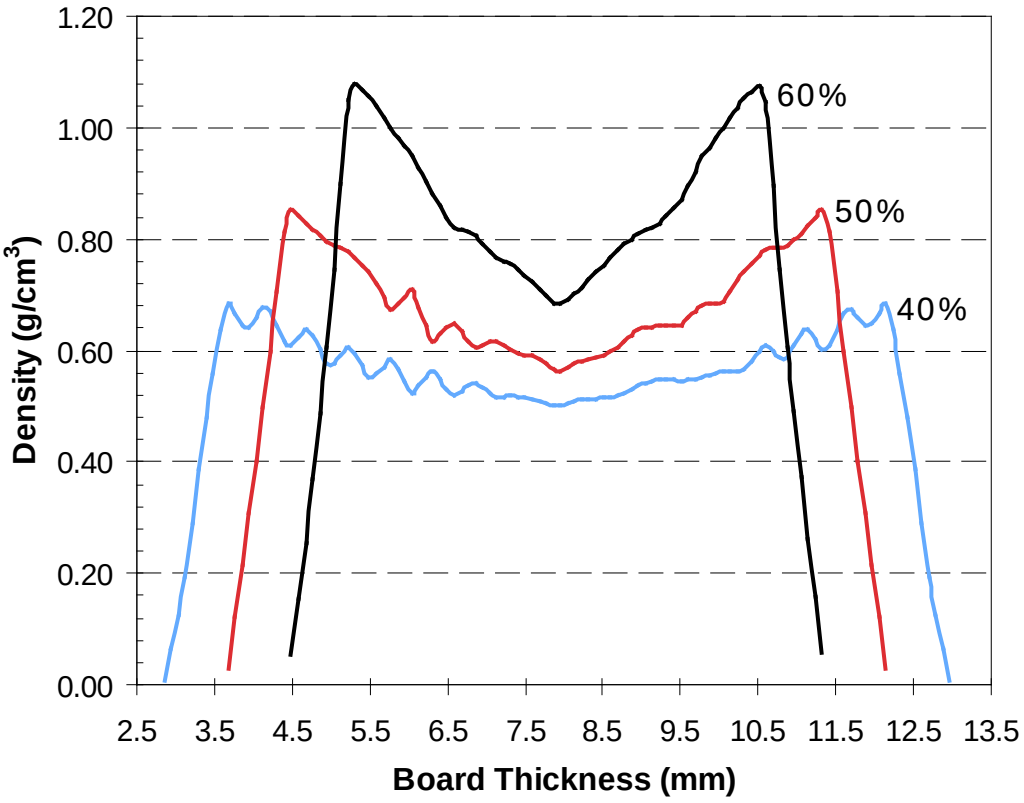

Figure 6.3. Simulated density profile of commercial OSB panel for different levels of compactions at compaction of 64 m/sec.

6.4.2 VTC and Control Panels

The density profiles for OSB with different weight percent of enhanced mechanical properties strands (viscoelastic thermal compression [VTC]) on both surfaces were also studied. The simulations considered OSB panels with 20% or 40% by weight VTC strands on the surface (10% or 20% by weight on each surface). The VTC panels were compared to control panels with 20% or 40% by weight normal surface strands. The strands in the face layers were parallel to the surface of analysis but the strands for the core layers were randomly oriented (see chapter 3 for details).

Figure 6.4 shows the experimental density profile of 20 % control strands and 20% VTC strands (Rathi 2009). The U-shape is still obtained. For the panel with 20% VTC, the whole curve of the density profile was shifted up. This is because the initial density of VTC strands is higher than the density of the normal strand.

When a panel with surface VTC strands is compacted, more compaction will happen in the core because the VTC layer is already compacted wood which cannot compact much more. Thus compared to panel with VTC, the core of VTC panels is expected to have higher density. The surface of VTC panels will start with higher density but will get closer to panels without VTC as compaction increases. Experimental results shown the surface density still remain higher in VTC panels versus control panel.

Figure 6.5 shows the experimental density profile of 40% by weight control strands or VTC strands on the surfaces (Rathi 2009). In this case, the regions of high density on the surface are larger than the case of control 20% by weight because more strands were placed on the surface. Similar to 20% VTC strand panels with 40% VTC strands had higher density throughout compared to control panels.

Figure 6.6 combines results for Figure 6.4 and Figure 6.5. The density profiles of the control 20% and 40% had the similar shapes. The panel with 40% VTC was just a little higher density compared to the 20% VTC. Therefore, panel with 40% VTC would be expected to have higher mechanical properties compared to panel with 20% VTC.

Figure 6.7 and 6.8 show simulated results for 20% control and 20% VTC or for 40% control and 40% VTC, respectively. The simulated curves were for panels compacted by 40%. Similar to experiments, the surface of VTC panels had higher density and the higher density region was larger for 40% VTC panels. The differences in surface density between VTC and controls, however was higher in simulated results than in experimental results.

The 20% panels showed no difference in core density between VTC and control panels, which differ from experimental results, where VTC panels had a denser core. In better agreement with experiments, the simulated results of 40% panels did shown higher core density in the VTC panel.

Figure 6.9 combines all simulation results. The 20% and 40% control specimens were similar. The 40% VTC panel showed overall higher density than the 20% control VTC panel.

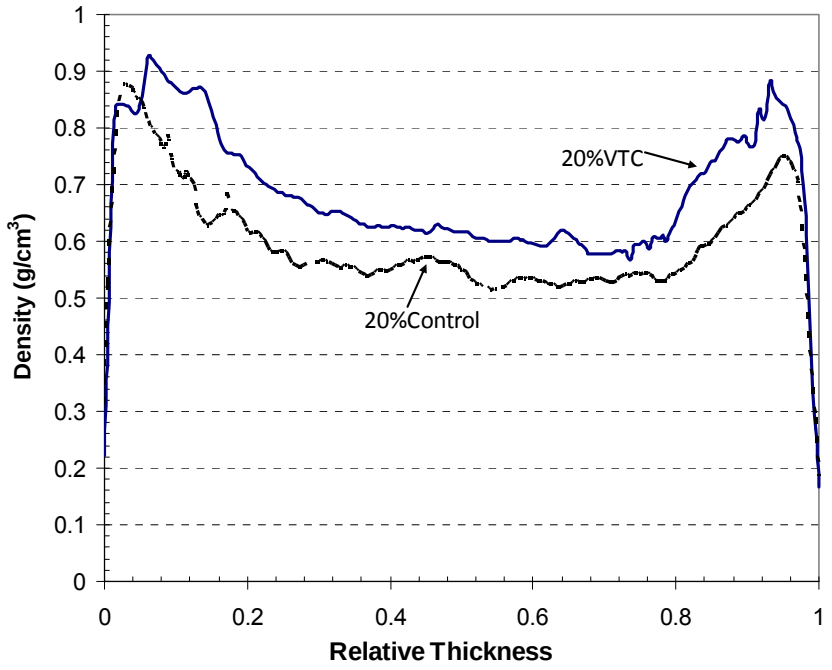

Figure 6.4. Experimental density profile of control 20% and 20% VTC by weight (Rathi 2009).

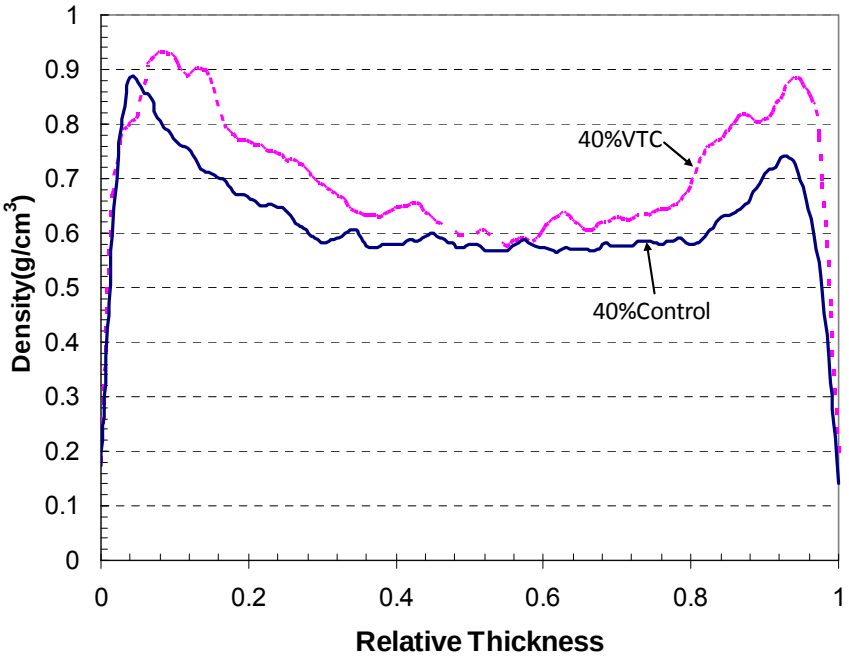

Figure 6.5. Experimental density profile of control 40% and 40% VTC by weight (Rathi 2009).

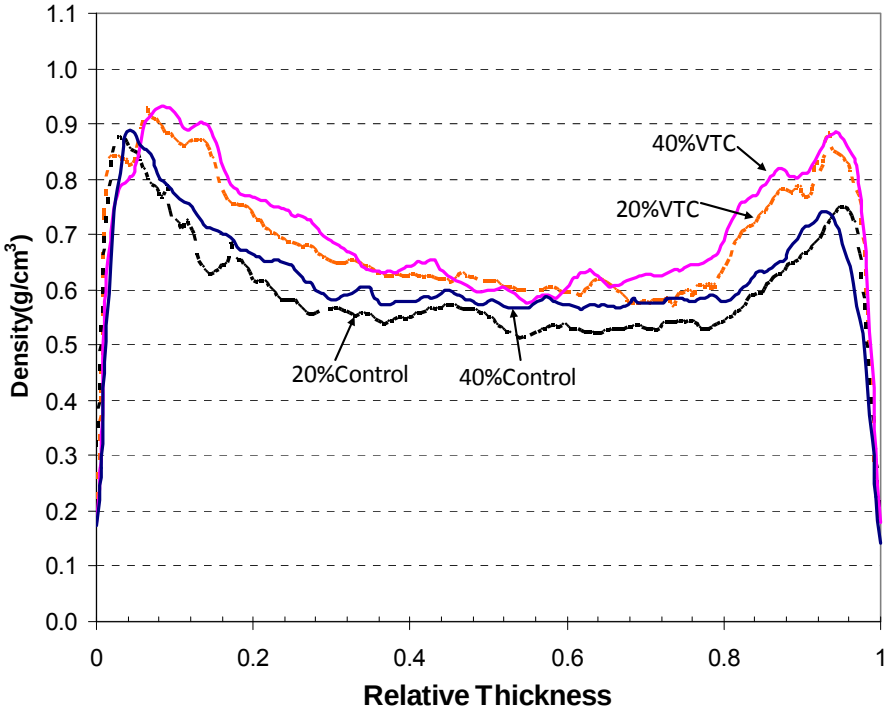

Figure 6.6 Re-plot of combine Figure 6.4 and Figure 6.5 (Rathi 2009).

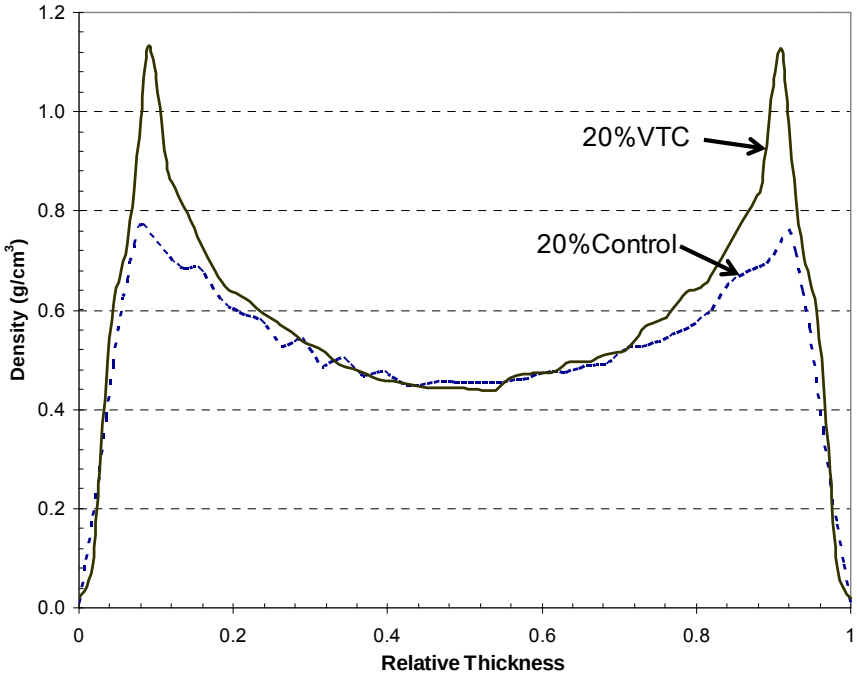

Figure 6.7. Simulated density profile of control 20% and 20% VTC by weight surface strands at 40% compaction.

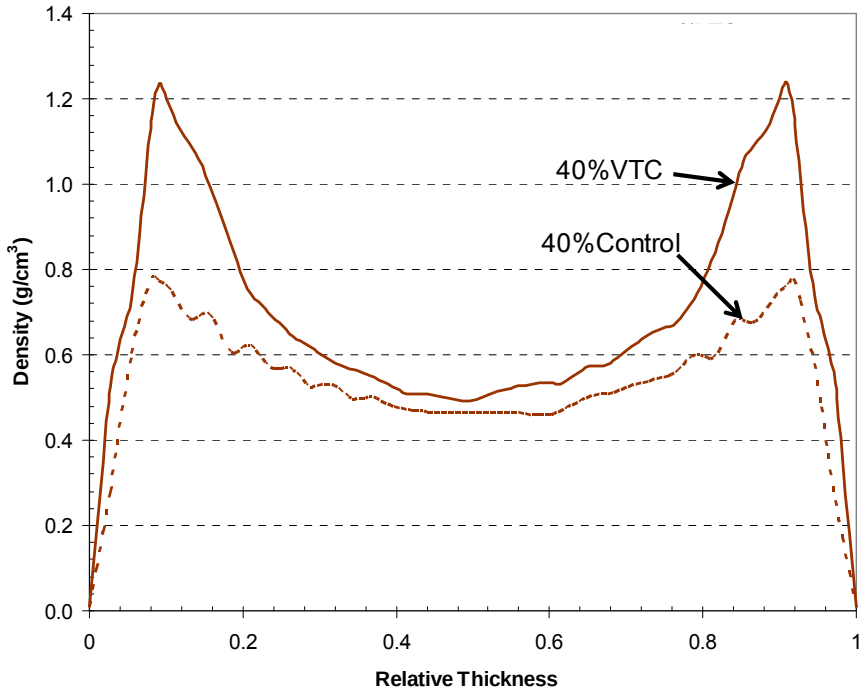

Figure 6.8. Simulated density profile of control 40% at compaction rate of 4 m/sec at 40% compaction.

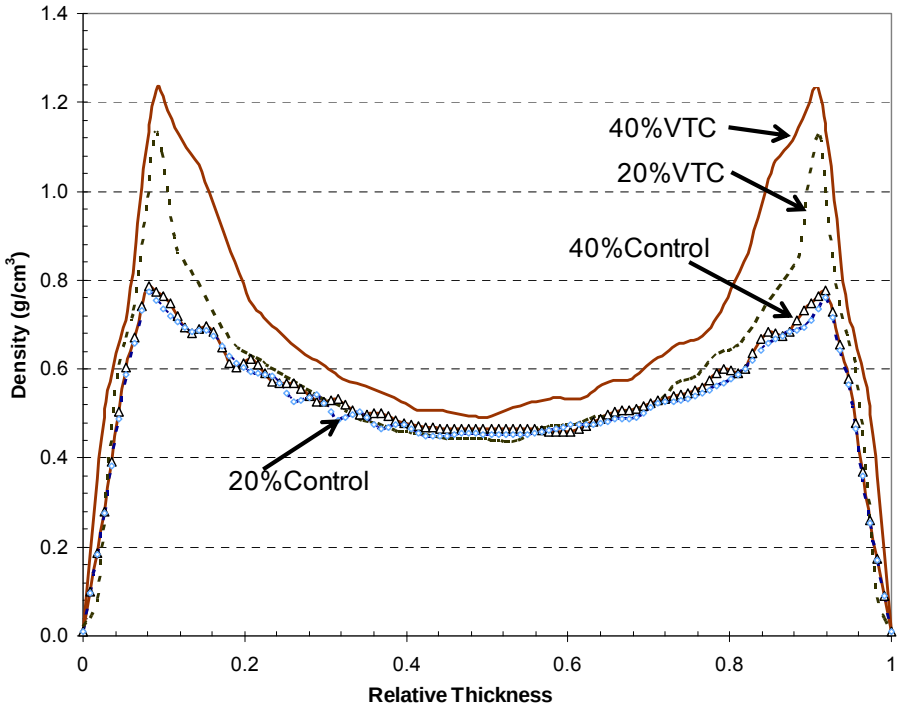

Figure 6.9. Re-plot of combine Figure 6.4 and Figure 6.5 at 40% compaction.

6.4.3 Effect of Compaction Rate

Figure 6.10 shows the results of simulated density profile of commercial OSB for different compression rates. The density near the surface of the panel increased as the compression rate increased. As the density of the surface increased, the density in the core region decreased. As the compression rate is increased, there is less time for the stress to move to the core region. This creates higher stress on the surface right beneath and above the two platens. Therefore, there is nonuniform stress distribution which leads to increase in density at the surface while reducing the density of the core.

These effects at high rate are caused by inertial forces. The results in Figure 6.10 indicate that compression rates of 64 m/sec and higher are influenced by inertial effects. The results of density profiles for compression rates 16 m/sec lower, on the other hand, are independent of compression rate. These results suggest the simulation of OSB compaction should use rates of 16m/sec or less. Since the material model used in these simulations (Hill plastic material) does not depend on rate, as long as inertial effects are small, the simulations will be independent of rate. Thus simulations at rate slower than 16m/sec should be valid even for actual platen speeds (<< 1m/sec). This conclusion would change if the Hill-plastic material was replaced by a time dependent material (such as a viscoelastic material) or if the simulations were coupled to heat and moisture transfer (which have different time scales than stress waves).

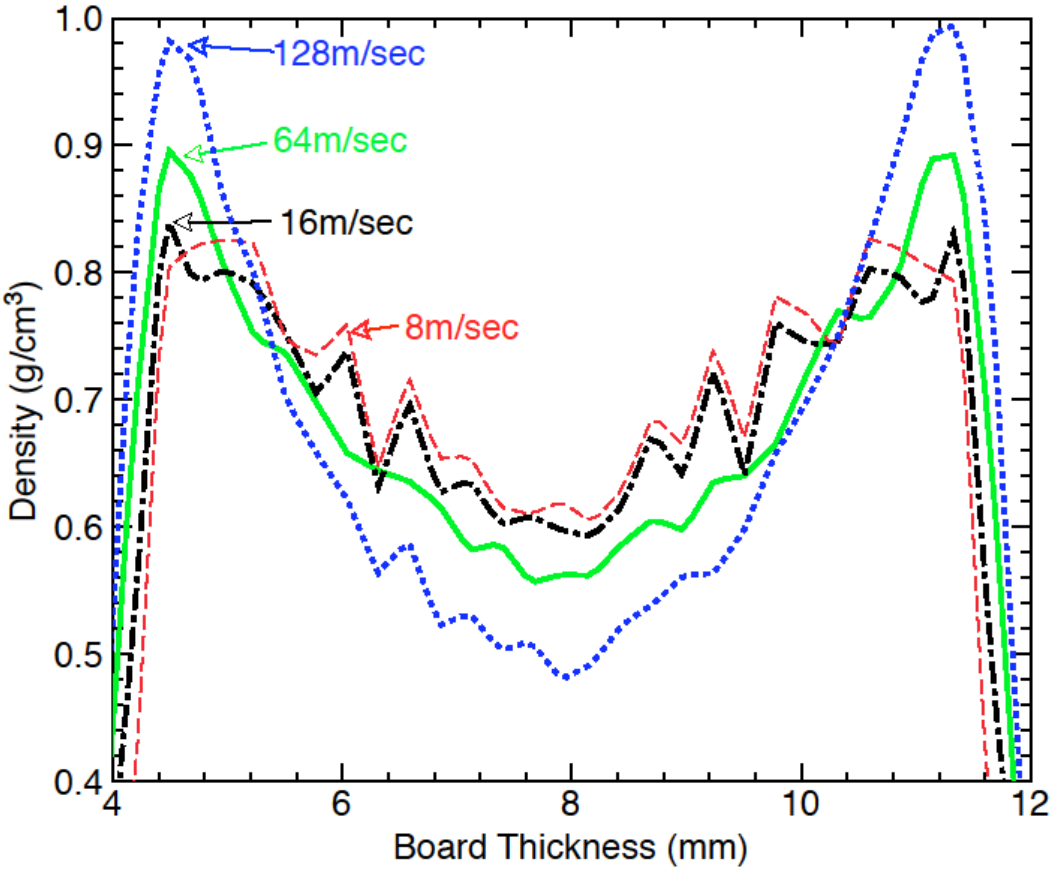

Figure 6.10. Simulated density profile for different compression rate.

6.4.4 Effect of Surface Layer Properties

The heated plates in contact with the surface layer are likely to soften that layer relative to the core layer. The ideal simulation would couple the analysis with heat and mass transfer and allow strand properties to depend on temperature and moisture content. Because that approach is beyond the scope of the current study we instead got approximate results by studying the effects of surface layer yield stress and stiffness on the VDP.

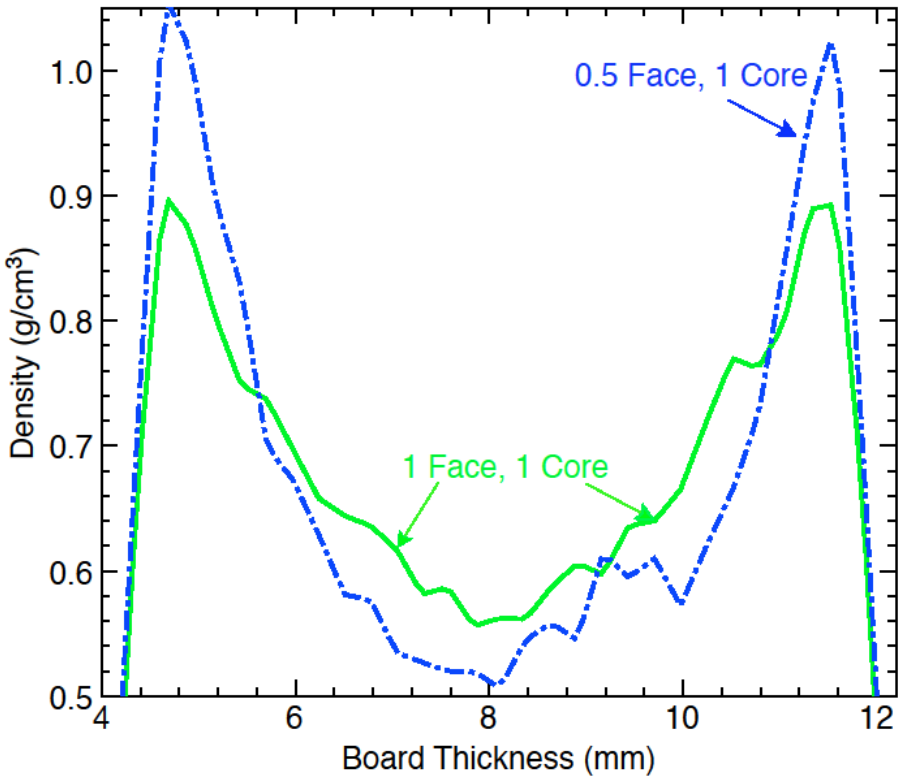

Figure 6.11. Simulated density profile for different yield stress on the core and face (surface) layers (strand length =150 mm +/- 20 mm; face gap [end-to-end spacing] = 15 mm +/- 4 mm; strand width = 25 mm +/- 3 mm; width gap [side-to-side spacing]= 5 mm+/- 1 mm).

Figure 6.11 compares the density profile (at 50% compaction) for sample with uniform yield stress(1 face, 1 core) to one where surface yield stress was reduced by half (0.5 face, 1 core). There is a higher density in the face region than the control when the yield stress in the face layer is reduced by half. This is due to the fact that lowering yield stress of the face resulted in more compaction in the face layer and led to a higher density in the face area. While the density profile for the face is increased, the density profile of the core area is decreased.

Figure 6.12 compares results of simulated density profiles when moduli (MOE and shear) are uniform (control) to sample with face moduli reduced by half (0.5 face, 1core). When the moduli of the face layers are reduced by half, the density at the surface

increased and the density in the core region decreased. When the stiffness of the surface is reduced, the surface strands get more compacted than the core layer. More compaction in the surface will result in the increase of density at the surface.

Comparing the effect on density profile of reducing the yield stress to reducing the moduli, a reduction in moduli of the face layer had a larger effect on the density profile than a reduction in yield stress. There are two possible explanations:

1. Moduli are the more important properties and modeling of VDP should focus on moisture and temperature dependence of the moduli.
2. The plasticity model is inadequate. Classical plasticity theory, as used here, is a shear process and thus does not allow plastic densification. Better material models might change predictions about the effects of yield stresses.

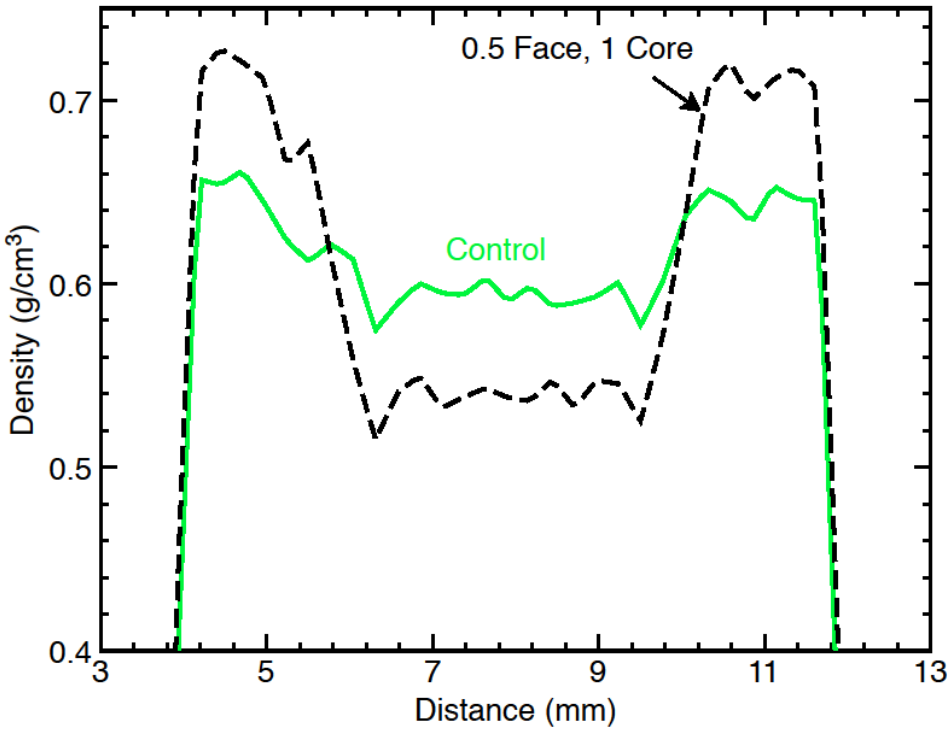

Figure 6.12. Simulated density profile for different stiffness values (strand length =150 mm +/- 20 mm; face gap [end-to-end spacing] = 30 mm +/- 5 mm; strand width = 25 mm +/- 3 mm; width gap [side-to-side spacing]= 10 mm +/- 1 mm).

6.5 Simulations of Vertical Density Profile in 3D

MPM simulations were also performed for three-dimensional OSB structures. An anisotropic elastic-plastic constitutive material model has been implemented for this study. The OSB mats consisted of three different layers. The top and bottom layer were each 25% of the strands with fiber direction partially oriented in the x direction. The 50% in the middle had strands partially oriented in the y direction. The process for modeling OSB in 3D was as follows:

1. Individual layers of a strand mat were created by randomly laying down strands of length 150 mm and with 25 mm but with random selected orientation.
2. Strand orientation was between the -90 and 90 degree along the partially oriented direction (x or y for different layers). The random orientation of each strand was selected by assuming a normal distribution $P(\pm\theta) = \frac{1}{\sqrt{2\pi\delta^2}} e^{\frac{-\theta^2}{2\delta^2}}$, where δ is standard deviation in orientation angle and the mean is zero. An experimental result for δ is 25 degrees (Nishimura, Assell and Ando, 2006). To select an angle, a random number was generated between 0 and 1 and then: $\theta = \delta * \sqrt{-2\ln(r)}$. The angle was then chosen as positive or negative (equally likely) with another random number.
3. A random layer was drawn using Illustrator software by rotating 150 mm x 25 mm rectangles by the random angles (from step 2) then adding to a 254 mm x 254 mm (10 in x 10 in) space until no more strands could be fit without overlap (see Figure 6.13).
4. The core layer strand's mean orientation was in the y-direction. These were obtained by rotating the images for face layers strands by 90 degrees.
5. The simulated OSB had 20 layers – 5 layers on each surface and 10 core layers. To reduce computational time, only half the panel was simulated with the center or the core being treated as a plane of symmetry. This means that only 10 layers

of strands were needed in the simulation, comprised of 5 layers of face strands and 5 layers of core strands.

6. The mats are then constructed by selecting 10 images for the 10 layers. The MPM model including strand location and fiber angle were created from the images. Each image provided a plane of particles at constant z in the analysis. Since the thickness of strands is 0.8 mm and cell size was 0.266 mm, there were 6 layers of particles per strand. A series of duplicate images was used to build each layer. The mechanical properties of the strands, determined from previous studies, were used as an input in this study. Figure 6.14 shows an uncompacted strand mat created by this process.
7. An MPM simulation was used to compact the strand mat. The individual strands were modeled as anisotropic elastic-plastic material (Hill yielding criterion [Hill 1948]) with work hardening. Figure 6.15 shows a strand mat that has been compacted by 40%. During the simulation, the analysis tracked the surfaces between the strands and tracked the local grain angles as the strands developed undulation.
8. Finally, the compacted mats were analyzed using 3D Visualization software (Nairn, 2006) and ParaView software (Kitware Inc. 2009) to analyze the mass distribution. The density profile map was obtained by dividing nodal mass by cell volume (MPM calculated unit cell: 7.9375 mm x 7.9375 mm 0.26666 mm).

For numerical convergence, in this study, the time step is set to 0.4 d/c, where d is the minimum dimension of the elements in the background grid and c is the maximum wave speed. The 3D mat has 32x32x60 particles (61440 total particles).

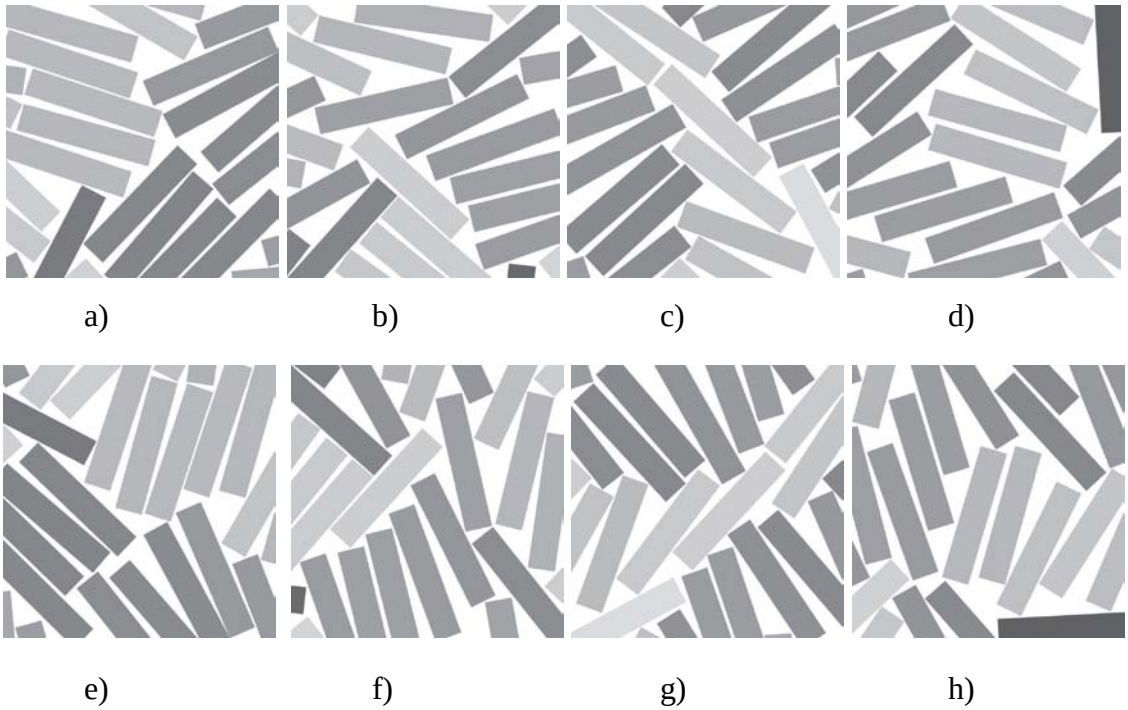

Figure 6.13. Sample images that were used to construct 3D mat; a) to d) are oriented in x-direction; e) to h) are oriented in y-direction. The gray scale indicated angle of that strand.

6.5.1 Commercial OSB

Figure 6.13 shows sample images that were used to construct the 3D mat. Figure 6.13a, 6.13b, 6.13c and 6.13d are images used for the face layers. Figure 6.13e, 6.13f, 6.13g and 6.13h are images used for the core layers. Images of the core layer are obtained by rotating images of the face layer by 90 degrees. Figure 6.14 is a sample calculation of following the orientation and mat that was prescribed with zero compaction. The gray scale represents strand orientation. Figure 6.15 shows a sample simulation of OSB at 40 percent of compaction. There is more undulating of strands in the core layer as the level of compaction increased but it is hard to see in this visualization tool.

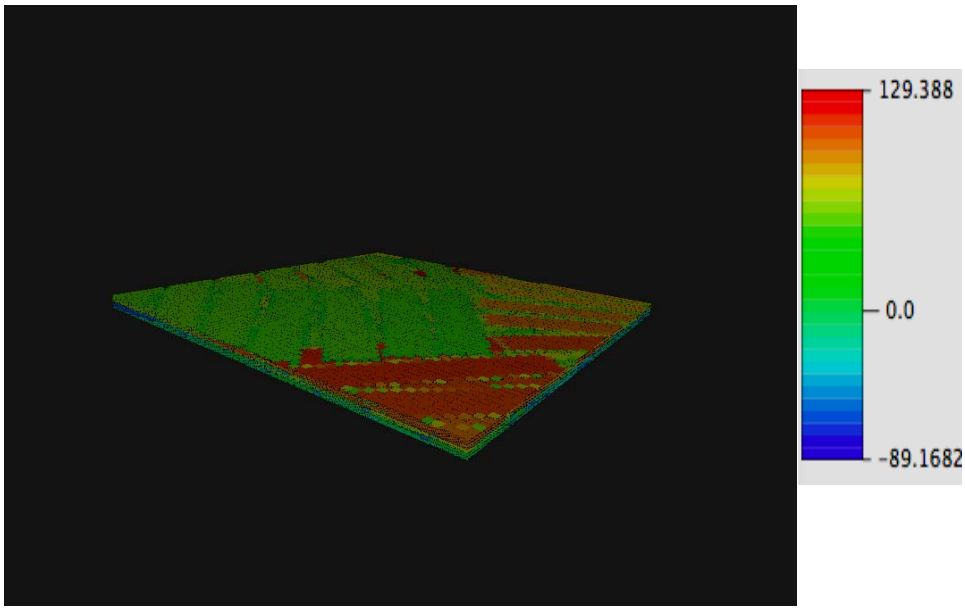

Figure 6.14. Sample calculation of commercial OSB at zero percent compaction.

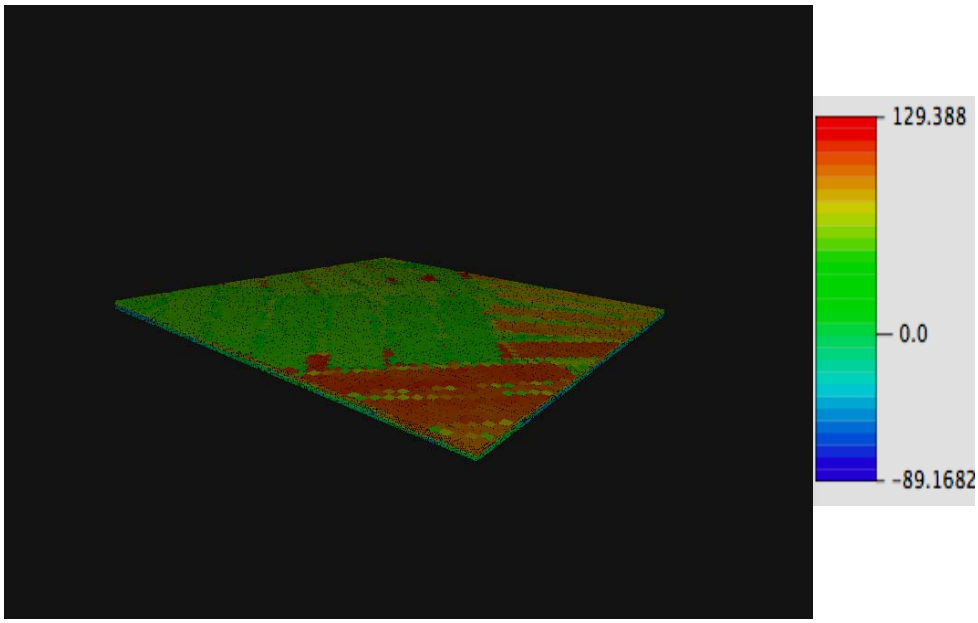

Figure 6.15. Sample calculation of commercial OSB at 40 percent compaction.

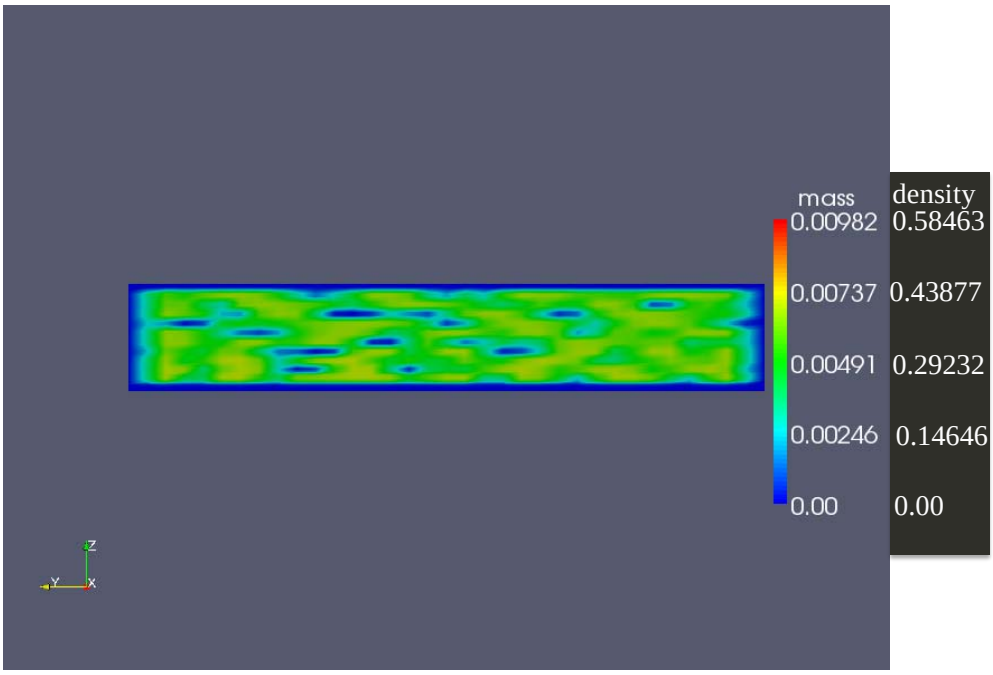

Figure 6.16. Across thickness density at 0% compaction.

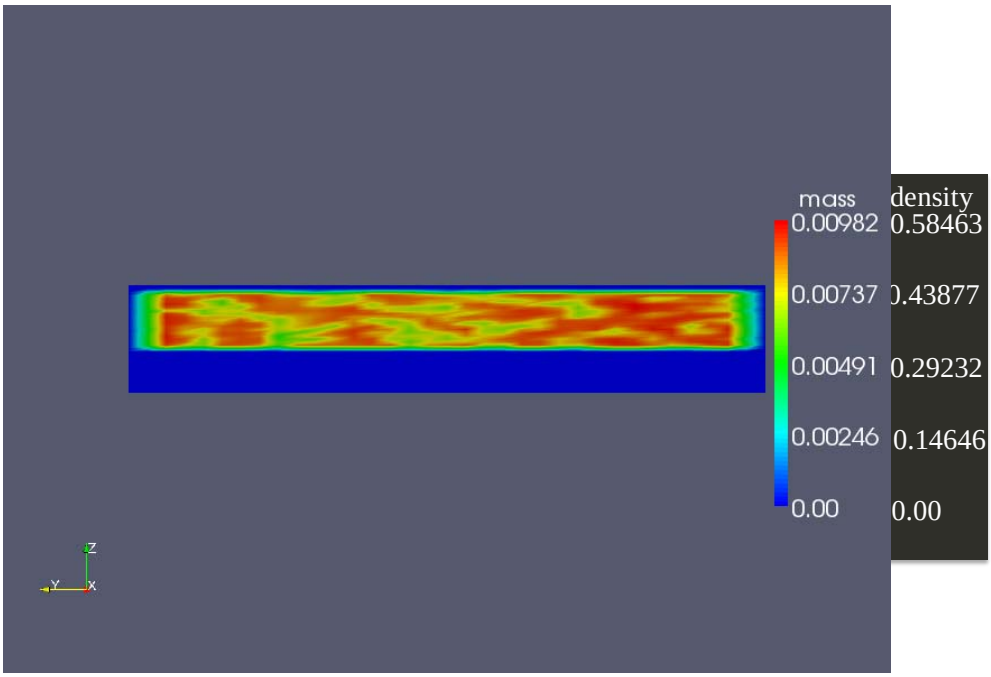

Figure 6.17. Across thickness density at 40% compaction.

Figure 6.16 shows a contour of density section of the panel at 0% compaction. The density is lower around the empty areas (no strands). Figure 6.17 shows a contour of density for a section of the panel at 40% compaction. As the level of compaction increases, the overall density increases. At lower levels of compaction, there is more void space and the structure is more opened (see Figure 6.16). At higher levels of compaction, there are less void spaces and the structures are denser (see Figure 6.17).

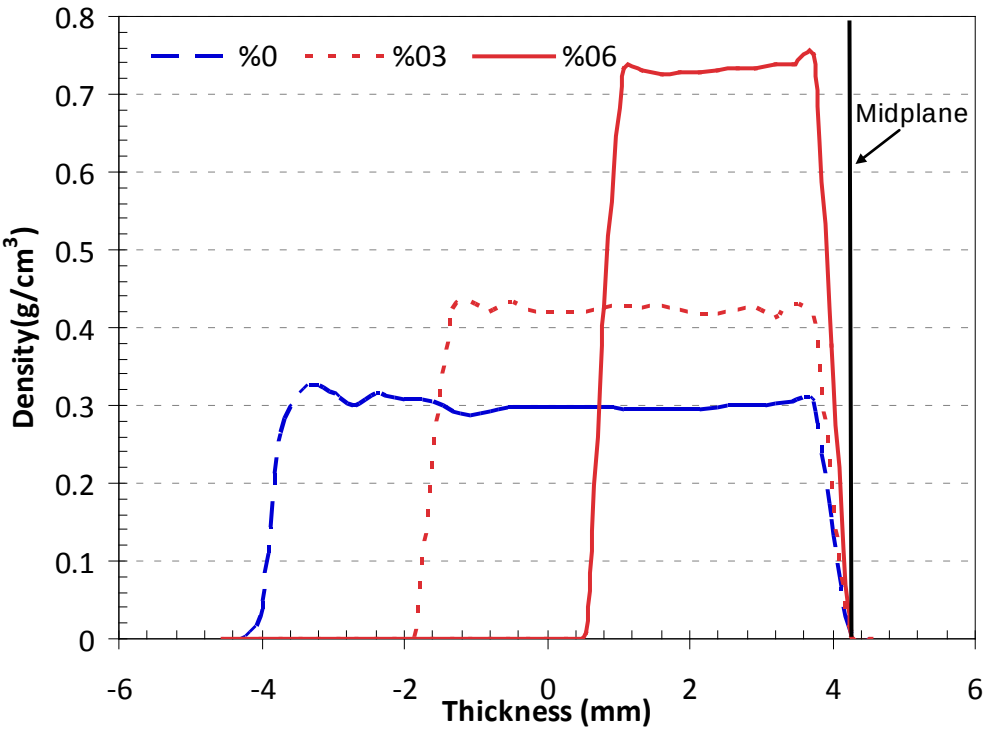

Figure 6.18. Simulated density profile (half) for different levels of compression in 3D.

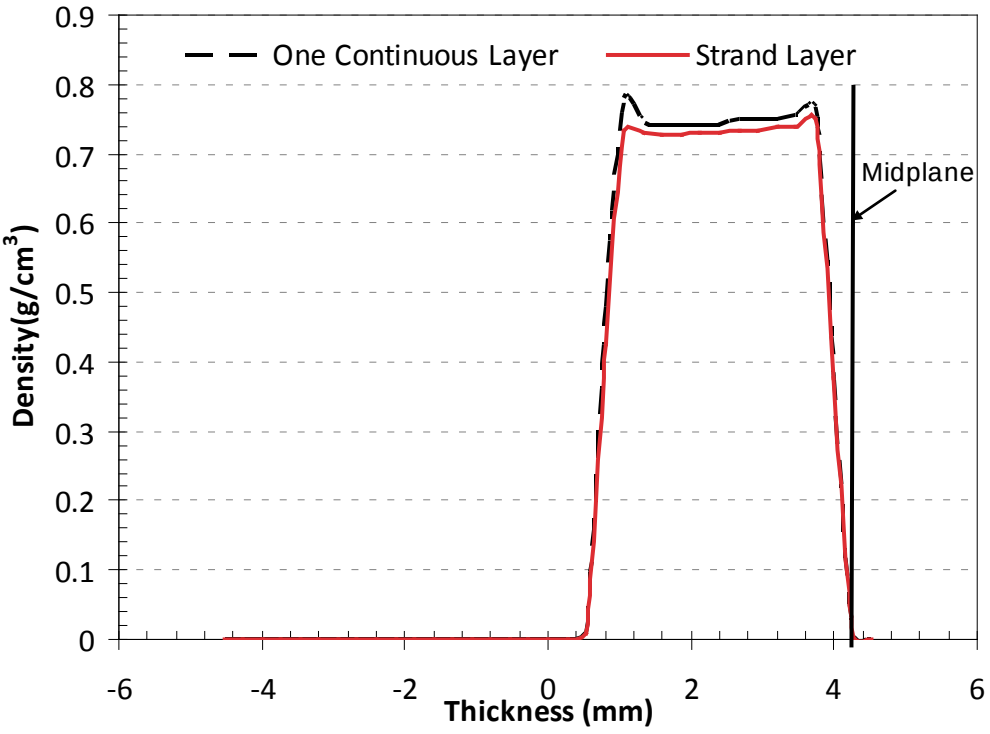

Figure 6.19. Simulated density profile (half) for continuous layer (no gap) at different levels of compression in 3D.

Figure 6.18, shows that the density profile (half the panel) for 3D calculation that went up to 30% and 60% compaction. No increase in surface density was obtained. Even as the level of compaction went up to 60%, the density profile remained flat. This may be because in 3D, there is Poisson's expansion in the width direction. The strands can therefore expand into empty spaces. This expansion into empty spaces may prevent densification of the surface strands.

To test for Poisson effects, a simulation was done where one surface layer had a continuous layer with no open space. Figure 6.19 shows small densification at the surface. Thus empty spaces in layers has an effect. Overall the 3D simulations are very different compared to 2D, suggesting the best study of VDP may require 3D simulations.

6.5.2. Effects of Surface Strand Properties

As in 2D simulation, the 3D simulations were repeated with altered surface properties. When the stiffness of the surface strands was reduced by half, the density of the surface was significantly increased (see Figure 6.20). As the stiffness of the surface strands reduce, the strand is softer and allows more compaction. The increased compaction of the surface strand resulted in increased density at the surface.

However, when yield stress of the surface strands was reduced by half, there was no increase in density of the surface (results not shown). This result may be controlled by the plasticity theory (see chapter 3). In the classical plasticity model (chapter 3 and Hill 1986), there is no change in volume once yielding occurs. All volume changes (densification) are due to elastic deformation and thus only influenced by elastic stiffness.

In processing of wood-strand composites (OSB), heat and moisture may reduce the properties of the surface strands. These reduced properties allow more compaction at the surface, thus leading to higher density at the surface. In order to fully model density profiles, we need to incorporate moisture and temperature gradient information into the mat during the pressing of the panel. A better plasticity model to account for densification may also be needed. This is because the traditional plasticity models do not allow for plastic densification after it yields. All modeling may also need to be 3D modeling, which further complicates the task.

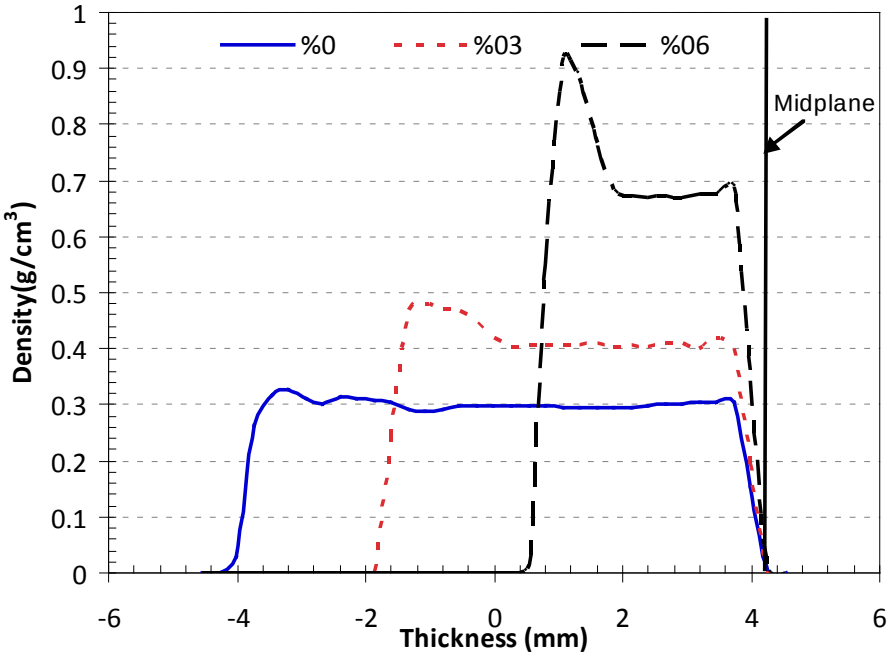

Figure 6.20. Simulated density profile (half) for different levels of compression in 3D with reduce stiffness of the face.

6.6 Homogenized Model Interpretation

6.6.1 Model Derivation

For another view of explicit numerical results, the calculated results of moduli are compared to a simplistic model based on homogenization of each layer, followed by simple and uniform compression.

The homogenized rule of mixture (HROM) is developed and this accounted for different levels of compaction, density, gap and strand length. The OSB composite representation by three layer structure, with density of each individual strand is combined and represented by a single number. For each layer, the axial density was replaced by a homogenized density by considering the volume of fraction of gaps within each layer. The density of the surface (ρ_S) and core (ρ_C) layers in terms of initial density were replaced by:

$$\rho_S = \rho_1 \frac{\langle L \rangle}{\langle L \rangle + \langle G_L \rangle} \text{ and } \rho_C = \rho_2 \frac{\langle W \rangle}{\langle W \rangle + \langle G_W \rangle} \qquad (6.1)$$

where ρ_1 and ρ_2 are the density of the surface and core strands, <L> and <W> are the average length and width of the strands, and <G_L> and <G_W> are the average gaps between strands in the surface and core layers. It was assumed the density increased uniformly due to compaction to $\rho_S/(1\text{-}C)$ and $\rho_C/(1\text{-}C)$, where C is the fraction of compaction. The simple rule of mixture was used to find effective density of OSB structures as:

$$\rho^* = \frac{\rho_S V_S + \rho_C V_C}{1 - C} \qquad (6.2)$$

where V_S, and V_C are volume fraction of surface and core layers. As the level of compaction increased the density increases. From chapter 3, the rule of mixture model gave:

$$E^* = \frac{E_S V_S + E_C E_C}{1 - C} \qquad (6.3)$$

Combining the two results, the effective modulus in terms of panel density is

$$E^* = \left(\frac{E_S \mathrm{V_S} + E_C V_C}{\rho_S + \rho_C} \right) \rho^* \qquad (6.4)$$

The results of HROM of MOE as a function of density are shown below.

6.6.2 Model Interpretation

Figure 6.21 is the simulated modulus of commercial OSB (from previous study in chapter 3, section 3.6.1) versus overall panel density for two different values of $1/D_t$. The simulated MOE deviated from simple linear theory. This deviation is mainly due to the strand undulation and surface compaction. MOE increased greatly as overall panel density increased. At further compaction, there is a crossover of simulated results. This is mainly due to the fact that at high level of compaction, the surface strands contribute more to MOE. Furthermore, in processing of OSB panel at the initial stage of pressing, density is increasing slowly as a level of compaction increased. At the later time, density

is increased much faster as the two hot plates compacted during pressing panel. At this stage, density is no longer linearly increases as increase compaction. As a result, the increased density resulting in more increase of MOE. There are more increases in modulus at high levels of compaction. And this is mainly due to non uniform compaction in OSB.

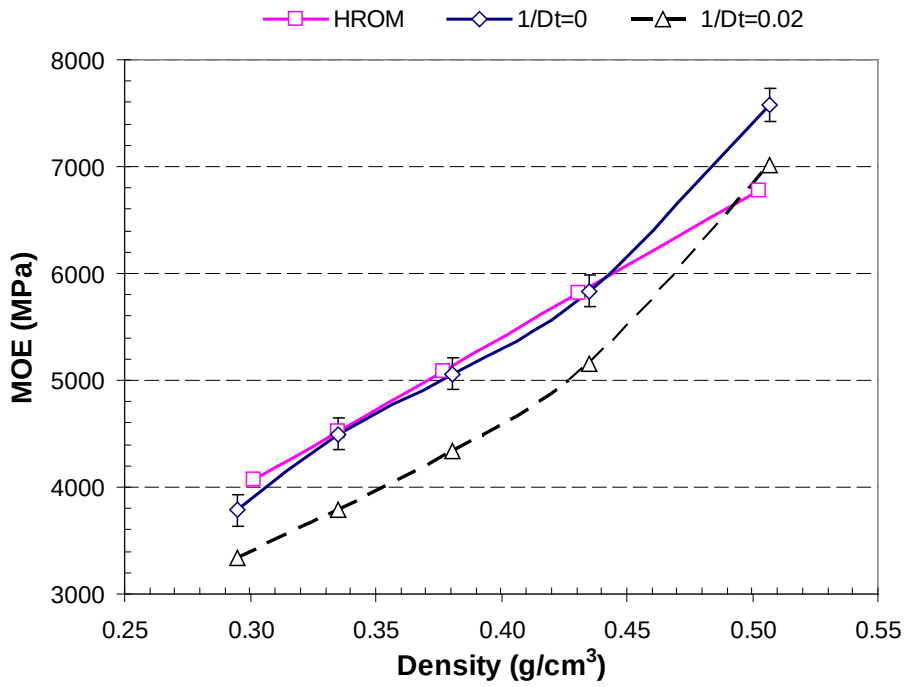

Figure 6.21. Simulated modulus versus overall panel density for different reciprocal of interfacial stiffness parameter in commercial OSB.

Figure 6.22 is the simulated modulus for panels with VTC strands in the surface (from previous study in chapter 3, section 3.6.4) versus overall density for two different values of $1/D_t$. MOE increased as density increased. In Figure 6.21, the simulated MOE is lower than the HROM even with the case of $1/D_t=0$. This is because surface VTC strands are higher in stiffness and also aligned with the grain, thus contribute to the calculation of MOE.

Unlike the results in Figure 6.21, here the density of VTC strand already higher than the core. Therefore less compaction on the face strands. This results in no crossover

like the case in Figure 6.21 at high compaction. Furthermore, there are all VTC strands on the face layers with high stiffness thus contributed the most to the modulus.

The results of Figure 6.22 also show interfacial effects have a large contribution to the overall stiffness of the panel. There is linear increase of the stiffness as a function of compaction.

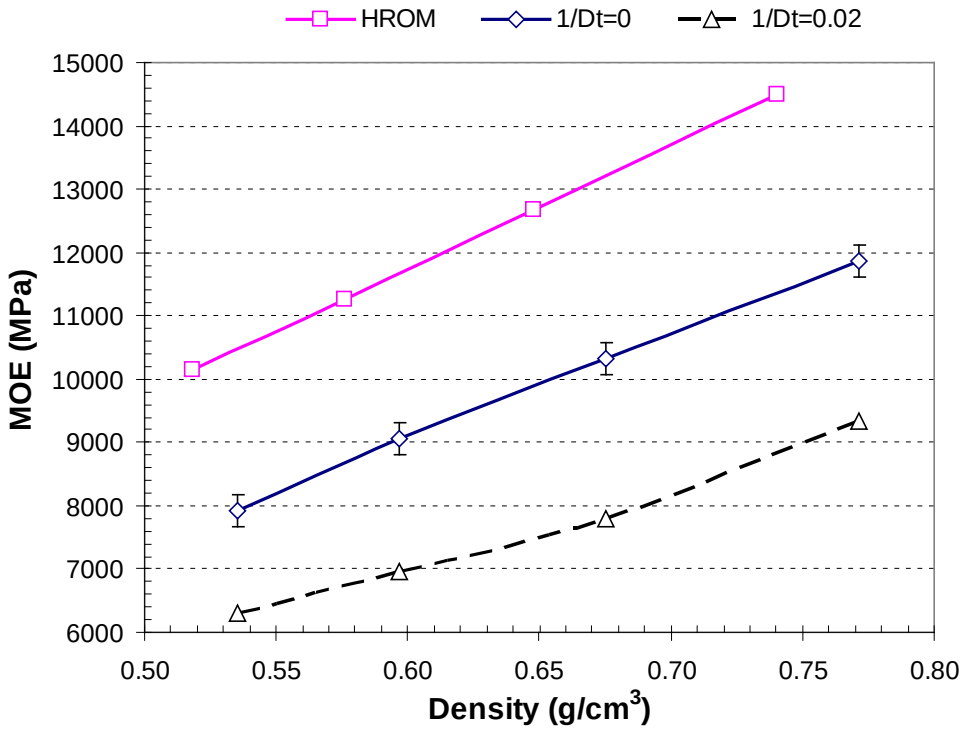

Figure 6.22. Simulated modulus versus overall panel density for different values of $1/D_t$ for commercial OSB with surface VTC strands.

6.7 Summary and Conclusions

The vertical density profile influences the overall OSB panel stiffness. In processing, the manufacturer usually demands higher density at the surface to carry the higher load in bending for structural applications. To know the specific density profile at different levels of compaction, manufacturers could benefit from optimization during processing and manufacturing of OSB. During processing, manufacturers usually obtain the stiffness and vertical density profile by trial and error. From the relationship between

vertical density profile and stiffness at different levels of compaction, the manufacturer can tailor the process to achieve high load carrying panels. Moreover, enhanced strand (VTC) on the surface layer increases density.

Additionally, reducing yield stress of the surface strands in 2D simulations gave an increase in density for the face. Reducing yield stress and moduli at the face layers in 2D increases the density at the surface area. In 2D, reducing moduli at the surface layers had more effect on the density profile than reducing the yield stress. Furthermore, increasing compaction rate increases the density at the surface of the panel.

The simulation of density profile in 3D showed different results than the 2D. In 3D, the Poisson's expansion resulted in no increase in density of the surface. There is some increase in density of the surface when there is no gap on the surface layer. Unlike the 2D, there is no increase in density profile of the surface when reduced yield stress of the surface strands. However, in 3D reducing moduli at the surface layers had an effect on the density profile of the surface strands. Furthermore, 3D model of MPM is able to look into interior structure or morphology of the panel.

Finally, to fully model the vertical density profile, moisture content gradient and a temperature profile is needed. A better plasticity model to account for densification is needed because the traditional plasticity model did not allow for plastic densification after yielding occurred. As all results all densification is due to by elastic deformation. Additionally, the simulations may need to be done on 3D. More work is needed to get the same simulation results for the vertical density profile as experimental results.

Appendix

We have density of the surface and density of the core as:

$$\rho_S = \rho_1 \frac{\langle L \rangle}{\langle L \rangle + \langle G_L \rangle} \qquad \text{and} \qquad \rho_C = \rho_2 \frac{\langle W \rangle}{\langle W \rangle + \langle G_W \rangle}$$

where ρ_1 and ρ_2 are the density of the surface and core strands, <*L*> and <*W*> are the average length and width of the strands, and <G_L> and <G_W> are the average gaps between strands in the surface and core layers. It was assumed the density increased uniformly due to compaction to ρ_S/(1-*C*) and ρ_C/(1-*C*), where *C* is the fraction of compaction. The simple rule of mixture was used to find effective density of OSB panel as:

$$\rho_{Panel} = \frac{\left(\frac{\langle L \rangle}{\langle L \rangle + \langle G_L \rangle} + \frac{\langle W \rangle}{\langle W \rangle + \langle G_W \rangle} \right)}{1 - C} \rho_W$$

But compaction ratio (CR) is equal to panel density divided by density of solid wood (strand) and CR is:

$$CR = \frac{\frac{\langle L \rangle}{\langle L \rangle + \langle G_L \rangle} + \frac{\langle W \rangle}{\langle W \rangle + \langle G_W \rangle}}{1 - C}$$

In our simulation, we define C = fraction compression where:

$$C = FractionCompression = \frac{h_0 - h_1}{h_0}$$

References

Dai C., C. Yu and J. Jim (2008) Theoretical modeling of bonding characteristics and performance of wood composites. Part IV. Internal bond strength, Wood and Fiber Science, 40 (2), pp 146-160.

Hse, C. Y. (1972) Wettability of southern pine veneer by phenol-formaldehyde wood adhesive. Forrest Prod. J. 22(1):51-56.

Humphrey, P. E. (1991) Pressing issues in panel manufacture: Internal behavior during pressing and its impact on time minimization, properties, and profit. Pages 99-108 in Proc. 2th International Particleboard/Composite Material Symposium, Washington State Univ., Pullman, WA.

Kamke, F.A., E. Kultikova, and C. A. Lenth (1996) OSB properties as affected by resin distribution. Page 147-154 in the Fourth International Panel and Engineered-Wood Technology Conference & Exposition, Atlanta, GA.

Kitware Inc. (2009) 3D and 3D Visualization tool. Retrieved from http://www.paraview.org.

Marr A. A. (1983) Applications of wood bonding. Pare 367-418 in R. F. Blomquist, A.W. Christiansen, R. H. Gillespie, and G.E. Myer, eds. Adhesive bonding of wood and other structural materials. Pennsylvania State University, University Park, PA. Educational Modules for Material Science and Engineering Projects.

Rathi V (2009) Bending property enhancement of wood strand composite using viscoelastic thermal compression *MS Thesis* Oregon State University, Corvallis, OR.

Wang S, P. M. Winistorfer (2000) Fundamentals of vertical density profile formation in wood composites. Part II. Methodology of vertical density formation under dynamic conditions. Wood Fiber Sci 32:220–238.

Xie, Y., M. Feng, and J. Deng, 2004. Quantification of UF and PF resins in MDF fiber with an X-ray fluorescence spectrometer. Wood Fiber Sci. 36(3):337-343.

Xu W. (1999) Influence of vertical density distribution on bending modulus of elasticity of wood composite panels: a theoretical consideration. Wood Fiber Sci 31(3):277–282.

Xu W., O. Suchsland (1998) Modulus of elasticity of wood composite panels with a uniform density profile: A model. Wood Fiber Sci 30(3):293–300.

CHAPTER 7 – FINAL CONCLUSIONS, RECOMMENDATIONS AND FUTURE DIRECTIONS

7.1 General Conclusions

A new technique that combined both experimental and analytical methods was developed to measure the interfacial stiffness of the adhesive bondlines between strands-used in wood-strand composites. The interfacial parameter D_t was extracted from experimental data on double lap shear specimens using shear-lag theory from given specimen mechanical properties (stiffness) and geometry. The interfacial parameters were obtained as a function of resin coverage. The results showed that in both normal and modified wood strands, resin coverage area has a positive effect on the interfacial properties, and consequently on mechanical (stiffness) properties of wood-based composites. As adhesive coverage increased from discrete droplet (1% coverage) to a continuous bondline (100% or fully glued) the stiffness of the interface increased and could even be stiffer than the wood itself. The interfacial property D_t is higher for PF resin than for PVA wood glue. The adhesive interfacial stiffness is higher when using strands with enhanced properties such as viscoelastic thermo compression (VTC) strands than when using normal strands.

A numerical model based on the material point method was developed and used to study the effect of stiffness parameters on the mechanical properties of wood-based composites. The glue-line interfacial property affects the mechanical properties of the entire composite. As the interfacial property increased (from discrete droplets to continuous bond line), the mechanical properties of strand-based composites increased.

7.2 Tensile Properties

In tension, MOE is greatly affected by the level of compaction and interfacial stiffness. MOE increased as the levels of compaction increased. The modulus of the OSB panel with inadequate gluing is approximately 10% to 25% lower than it could be with improved adhesive application. There is no effect of the glue stiffness on mechanical properties of composites with long elements, such as veneers with perfect alignments

(plywood). These simulations confirmed the importance of strand undulation in the OSB panels. The importance of interface is therefore increased whenever there is strand undulation such as in typical OSB or OSL structures.

To better interpret numerical results or glue-line properties and undulating strands, a simple homogenized rule of mixtures (HROM) was developed for OSB and oriented strand lumber (OSL) structures. The results of MPM were compared to the HROM model and laminated plate theory. The difference between simulations and the simplistic model is that the model cannot predict the influence of interfacial stiffness, strand undulation, or non-uniform compaction.

7.3 Bending Properties

Numerical simulations results show MOE in bending is higher than MOE in tension. MOE also varied for different levels of adhesive coverage (different values of $1/D_t$). The effect of interface of MOE in bending is greater than MOE in tension. HROM had worse agreement in bending than in tension due to difficulty of a simple model adequately dealing with gaps.

In contrast to tension, the glue stiffness effect remains in bending even when there are no gaps such as for plywood or LVL. These results show that interfacial properties are even more important for composites loaded in bending than in tension because the properties are affected even in the absence of strand undulation.

7.4 VTC Tension and Bending

Adding VTC strands on the outer layer of OSB panels enhanced the properties. There is higher MOE in bending than in tension. The VTC panels were slightly more affected by glue stiffness the control panels. Fortunately, VTC-VTC adhesive bond lines had glue bond stiffness similar or higher the normal strand bond lines. VTC strands enhanced panel properties even when added at constant weight fraction (20% or 40%) versus controls. The amount of improvement due to VTC depended on resin coverage with more resin (higher D_t) leading to more VTC enhancement. 40% VTC increased

more (percentage wise) than 20%. Simulated results were lower than experiments but trends in the relative increase were similar. The glue is very important for VTC composites to achieve optimal properties.

7.5 Aspect Ratio

One way to increase load carrying capacity in wood composites panel is to increase interfacial stiffness but this may be difficult or costly. This is because to increase interfacial stiffness more resin is needed, which will increase cost, and more work is need to spread resin on the strands. Another approach to improve properties is to increase the fiber aspect ratio (strand length). It may be easier and cheaper.

MPM simulations showed that strand length has a large effect on the mechanical properties of wood-based composites. Decreases in gaps (void spaces between strands) increased mechanical properties. Similarly increasing the strand length in surface layers increased MOE. As strand length increased or gap spacing decreased, MOE approached the case with no gaps.

Modern shear-lag model can incorporate interfacial stiffness into the shear-lag parameter and therefore predict modulus as a function of phase's properties, phase geometry (aspect ratio) and interfacial stiffness. From the shear-lag model, the effect of strand properties, aspect ratio and glue-line interfacial stiffness can be obtained for wood-strand based composites, plywood and laminated veneer lumber (LVL).

7.6 Vertical Density Profile (VDP)

Using current computation resources, a full simulation of VDP was not possible, but some approximate methods were done. A few selected variables were tested to study their effect of VDP. When the yield stress in the face layer is reduced, there is higher density in the face region than in the control. When the moduli of the face layers are reduced by half, the density at the surface increased and the density in the core region decreased. The density profile is also affected by high compaction rates (larger than 16 m/sec) and this is mainly due to inertial effects. From these results, moduli are more

important than yield stress and modeling of VDP should focus on moisture and temperature dependence of the moduli.

The simulated density profile in 2D resembles the experiment. However, simulations of density profile in 3D were very different then 2D. These results suggest that the best study of VDP will require 3D simulations. The importance of modulus, however was apparent in both 2D and 3D simulations.

7.7 Use of MPM

This study also has demonstrated that MPM can handle large-scale, morphology-based models of real wood-based composites including glue-line effects, strand undulation and compaction. It is very easy to generate a wood-strand composite structure based on strand length, strand gap, strand thickness and their standard deviations. Once the structure is compressed, the new structure can be tested in virtual experiments for properties.

Numerical simulation by MPM is a useful tool for studying the mechanical properties of OSB as a function of strand length, gap, and interfacial properties but it would be very difficult to study these effects by experiment. Thus a major advantage of MPM modeling on wood-based composites is that it can be used as a tool for optimizing their engineering design.

7.8 Recommendations and Future Directions

Here are some ideas for future work:

1. We were able to conclude from interfacial stiffness data that as the adhesive coverage increased from discrete droplets (1% coverage) to a continuous bondline (100% or fully glued), the stiffness of the interface could be stiffer than the wood itself and this may be due to resin penetration into the wood cells. More work needed to confirm role of penetration of resin into the wood cell on interfacial parameters and the mechanical properties of the entire wood-based composites.

For example, if penetration is crucial, why did VTC strands have stiffer glue bonds?

2. Measuring interfacial stiffness has no standard method and is difficult. Future work could develop a better interfacial stiffness test.

3. In order to precisely compare stiffness values from simulated panels to stiffness values from experiment, more work is needed to determine how much a typical OSB panel was compacted.

4. In processing of OSB panels and wood-based composites, moisture content (MC) helps soften the strands and to increase the density at the surface. However, if the moisture is too high, higher heat and longer closure press time is required. When the MC of the face strands is increased, the yield stress (and stiffness) is decreased. This reduction in yield stress (and stiffness) will increase compaction at the surface strand and consequently increase the density at these surface strands. More work is need with 3D simulation to study these effects.

5. Besides MC effects, there are also the heat effects during the formation and processing of the OSB panel. Therefore, in order to fully model the formation processing and mechanical properties of the OSB panel, a multi-scale modeling approaching is needed. The heat and formation of the mats can be obtained by using the heat and mat formation model (Zombori et al 2001 and references there in). The information of the mats formation is then obtained and based on heat and MC effect and will be used as an input into MPM model to study the effect on the mechanical properties. Since stress waves are much faster than the heat conduction and moisture diffusion, a multi-scale modeling approach is needed cover the full time scale.

6. When wood is densified, the volume still changes even after yielding occurs. However, in traditional plasticity model (Hill plastic) there is no volume change after yielding. The only volume change in these models is by elastic deformation.

Therefore, use of new plasticity models that incorporates post-yield compaction might be needed.

7. Interfacial stiffness is important for composites even in the absence of undulation such as in LVL or plywood. Therefore it would be useful to study the interface of other wood-based composite system such as plywood and/or fibrous composites such as natural fiber polymer composites (hemp Nylon 6 composites, bamboo polymer composites).

References

Zombori B., F. Kamke and L. Watson (2001) Simulation of the mat formation process. Wood and Fiber Science, 33 (4), pp 564-579.